DEVELOPING AN FDTD SIMULATION TOOL TO EVALUATE THE USE OF MAGNETIC INDUCTION ACROSS AN AIR-WATER INTERFACE

by

Mark Christopher Watson

Submitted in partial fulfillment of the requirements
for the degree of Master of Applied Science

at

Dalhousie University
Halifax, Nova Scotia
August 2020

© Copyright by Mark Christopher Watson, 2020

This thesis is dedicated to Bernard and Rosalind Watson.

Table of Contents

List of Tables

List of Figures

Abstract

Traditional underwater communication technology includes either the propagation of energy in the form of acoustic pressure waves or extremely low frequency electromagnetic radiation. Although today's acoustic technology is mature and robust, it is not able to transmit information across the air-water interface without the aid of additional electronics hardware. Extremely Low Frequency (ELF) electromagnetic radiation technology overcomes this problem; however, the low frequencies (30 - 300 Hz) require the use of very large antenna structures. The size of the ELF antenna makes this RF-based technology impractical for many applications requiring compact antenna structures including subsea oil and gas exploration, military, Underwater Internet of Things (UIoT) sensor networks, marine animal tracking, search and rescue, fishing, and environmental surveying, amongst others.

In this thesis, a simulation tool is developed to evaluate an underwater communication system which includes an air-water interface. The simulator evaluates Maxwell's equations using the Finite-Difference Time-Domain (FDTD) method. The custom FDTD simulator is designed using a 2D geometry for increased computational time, and is easily configurable such that the medium properties, coil position and orientation, and problem geometry can be user-defined. The simulator also considers the circuit properties of the transmitter and receiver using the lumped parameters of an RLC circuit model. Because the FDTD is a time domain simulation, it allows for a variety of input signals including single tones, broadband pulses, and modulated signals. Stability and convergence are successfully confirmed by running the simulation with decreasing cell size using a built-in convergence test feature. The accuracy has also been validated by comparing it against existing analytical models. The simulation tool predicts feasible transmitter depths up to 3 meters, with a receiving coil 1 meter above the air water interface, with channel capacities above several tens of kilobits per second.

List of Abbreviations and Symbols Used

Abbreviation	Description
ABC	Absorbing Boundary Condition
AWGN	Additive White Gaussian Noise
BER	Bit Error Rate
bps	Bits Per Second
BPSK	Binary Phase-Shift Keying
dB	Decibel
dBV	Decibel (Volts)
EM	Electromagnetism
ELF	Extremely Low Frequency
FDTD	Finite-Difference Time-Domain
FSK	Frequency Shift Keying
MI	Magnetic Induction
PDE	Partial Differential Equation
PEC	Perfect Electric Conductor
PML	Perfectly Matched Layer
QAM	Quadrature Amplitude Modulation
QED	Quantum Electrodynamics
RF	Radio Frequency
RLC	Resistor, inductor, and capacitor
RMS	Root Mean Squared
Rx	Receiver
SNR	Signal-to-Noise Ratio
TE	Transverse Electric
TFSF	Total-Field Scatter-Field
TM	Transverse Magnetic
Tx	Transmitter
UIoT	Underwater Internet of Things
UPML	Uniaxial Perfectly Matched Layer

Symbol	Description	Units
L	Inductance	Henry [H]
C	Capacitance	Farad [F]
R	Resistance	Ohm [Ω]
I	Current	Amp [A]
V	Voltage	Volt [V]
M	Mutual induction	Henry [H]
f	Frequency	Hertz [Hz]
f_o	Resonant frequency	Hertz [Hz]
t	Time	Often in Seconds [s]
$\vec{E}$	Electric field vector	Volt/Meter [V/m]
$\vec{H}$	Magnetic field vector	Amp/Meter [A/m]
$\tilde{E}$	Complex electric field vector	Volt/Meter [V/m]
$\tilde{H}$	Complex magnetic field vector	Amp/Meter [A/m]
$\vec{J}$	Current density vector	Amp/Area [A/m^2]
V_{emf}	Induced voltage	Volt [V]
V_o	Output voltage	Volt [V]
Q	Quality factor	-
$\tilde{C}$	Channel capacity	Bits Per Sec [bps]
B	Bandwidth	Hertz [Hz]
T_o	Ambient noise temperature	Kelvin [K]
k	Boltzmann's constant	Joules/Kelvin [J/K]
N_{Tx}	Number of turns in transmitter coil	Turns
N_{Rx}	Number of turns in receiver coil	Turns
N_{dim}	Resolution of smallest physical dimension	-
λ_o	Wavelength in air	Meter [m]
λ_{H_2O}	Wavelength in water	Meter [m]
Δ	Difference operator	-
∇	Laplacian operator	-

$\times$	Curl operator	-
$\cdot$	Dot product operator	-
∂	Partial derivative operator	-
d	Derivative of single variable	-
Ψ	Flux of a quantity	-
$\int$	Integration operator for single variable	-
$\oint$	Integration over a closed path	-
$\iint$	Integration operator over two variables	-
$\oiint$	Integration operator over a closed surface	-
Σ	Summation (except otherwise noted)	-
Ω	Ohm (except otherwise noted)	-
ψ	Often used as a dummy variable	-
$\hat{\rho}$	Unit vector in cylindrical coordinate system	-
$\hat{z}$	Unit vector in cyl/cart coordinate systems	-
$\hat{\varphi}$	Unit vector in cylindrical coordinate system	-
$\hat{y}$	Unit vector in cartesian coordinate system	-
$\hat{x}$	Unit vector in cartesian coordinate system	-
σ	Conductivity	Siemens/Meter [S/m]
μ	Magnetic permeability	Henry/Meter [H/m]
ε	Electric permittivity	Farad/Meter [F/m]
ρ_v	Electric charge volumetric density	Coulomb/Area [C/m^2]
R_r	Radiation resistance	Ohm [Ω]
$f(x)$	A function of x	-
$f'(x)$	Derivative of $f(x)$	-
δ	Skin depth	Meter [m]
$\mathcal{R}\{u\}$	Real part of parameter u	-
α	Attenuation constant	dB/Meter [dB/m]
β	Propagation constant	dB/Meter [dB/m]

Acknowledgements

My wife, Janelle, and my children Ben, Reid, Emerson, Keenan, and Adrian for giving me the motivation to work hard. My mother, Rosalind, and my late father, Bernard, for their love and support. My supervisor, Dr. Jean-Francois Bousquet, for allowing this opportunity. My research colleagues, Adam Forget and Cole Ferguson, for their valuable input. Dr. Z. (David) Chen, for introducing me to RF engineering and the FDTD method.

1 Introduction

Underwater sensor networks are used in many real-world applications including oil and gas, military, underwater internet of things (UIoT), animal tracking, search and rescue, fishing, environmental surveying, and more. The underwater sensors collect and store application-specific data which is retrieved by engineers and scientists for further processing. The transmission of this data from underwater to above the water's surface may take one of several forms. One common method is the use of electromagnetic radiation; however, in order to avoid large signal attenuation due to the water's conductivity, very low carrier frequencies must be employed sometimes on the order of tens of Hz (Gulbahar and Ozgur, 2012). To maintain a suitable radiation efficiency of the radiating antenna, this results in impractically large transmitters for use in many applications requiring small electronic hardware. Another method often used is the deployment of underwater unmanned vehicles which dive down to the submerged data acquisition system and retrieve the data often by use of acoustic or optical communication links (Kao et al, 2017). The cost of this option can be inhibitory and does not allow for applications requiring real time monitoring. This thesis investigates the use of a magnetic inductive link as an alternative means of wirelessly transmitting information across an air-water interface for use in an underwater sensor network.

This chapter will introduce the engineering challenges on which this thesis is based and the manner in which it is addressed. Next, the contributions of this research to the engineering and oceans technology communities will be highlighted. This chapter will also discuss the progress of research into magnetic induction in underwater applications over the past few decades. This literature review will be comprehensive; the papers and texts with the most significant impact on this thesis will be discussed. Finally, an outline of the organization of this thesis will be provided.

1.1 Problem Statement

An underwater senor network is being developed by researchers and students at Dalhousie University's UW-Stream Laboratory in partnership with Ultra Electronics Maritime Systems. To transmit data from under water into the air, existing systems often employ the use additional hardware to convert the acoustic pressure waves into RF energy for transmission into the air. An example of his type of system is shown in Figure 1. Underwater acoustics are prone to environmental noise, multipath effects, and high latency resulting in notoriously low data rates. Systems employing hydrophones like this can cost thousands of dollars. Further, acoustic signals run the risk of being intercepted and cause undesired acoustic noise which can be disruptive to the marine environment.

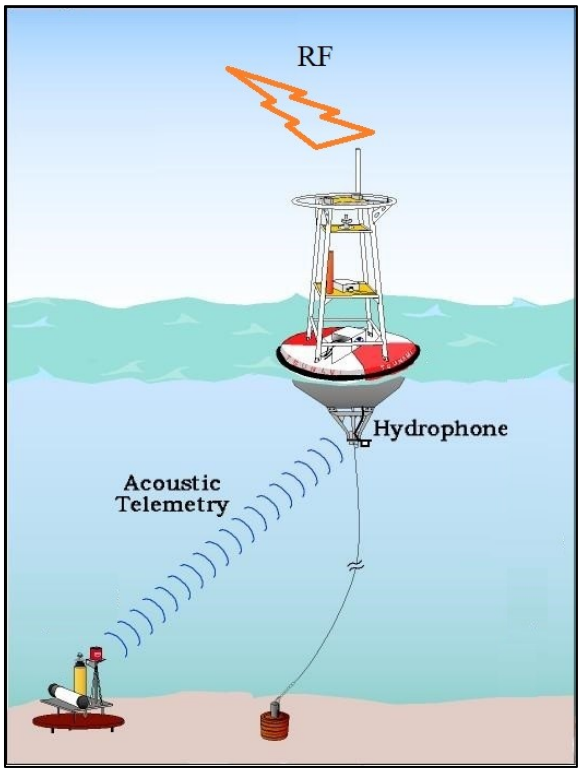

Figure 1: Traditional systems (modified from esrl.noaa.gov)

The underwater sensors may be used to collect data in various ocean applications. The amount of data to be collected would vary and could be very high. To simplify and reduce the costs associated with the collection of this information, and to keep the location of the underwater network discrete, wireless communication across the air-water interface is the preferred method for data transmission. To decrease the time required for data collection, a communication link with a suitable bandwidth must be developed with bitrates on the order of several tens of kilobits per second. Further, the sensor network may be located deep below the water's surface; therefore, targeted underwater transmitter depths are on the order of several metres. Finally, for system compactness, the size of the transmitter must be kept as small and as low power as possible. These are the engineering challenges addressed as part of this thesis.

1.2 Proposed Solution

Magnetic Induction (MI) could be a suitable technology for this application because it has the potential to address each of the engineering and design challenges discussed in the preceding section. The study of electromagnetic radiation for use in underwater applications dates to the early 1900s; however, MI has received greater attention lately due to its potential to provide a low latency and its potential for a relatively high bandwidth communication link in comparison with traditional underwater acoustics (Guo et al, 2017) (Domingo, 2012). MI-based systems utilize electrically small coils with low radiation resistance and are based on the mechanism of near-field inductive coupling (Gibson, 2003). Compared with other wireless communication standards, the bandwidth of a MI-based system is inherently narrow; however, bitrates on the order of several hundred kilobits per second may be achievable (Akyildiz et al, 2015). This thesis investigates the use of MI as a means of wireless data transmission across the air-water interface through the use of a custom simulation tool based on the finite-difference time-domain method.

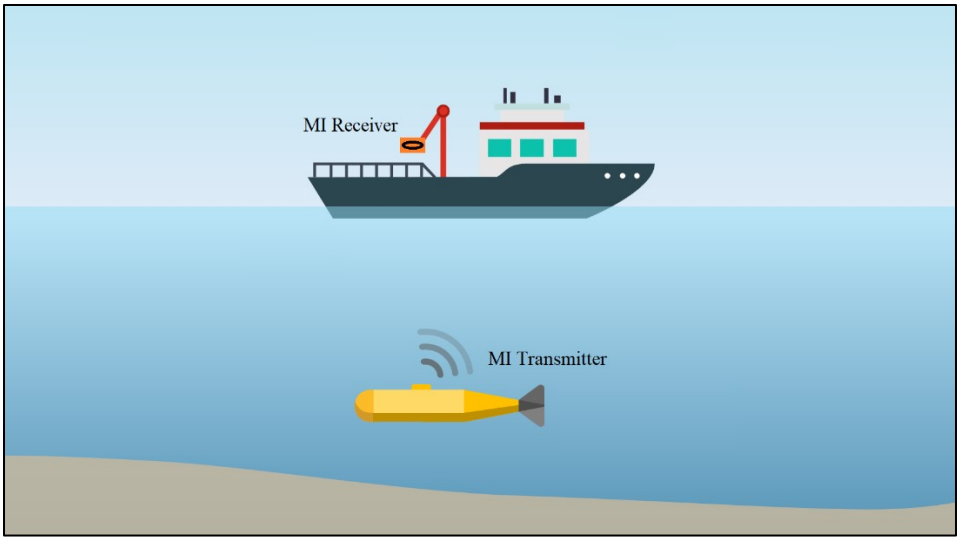

Figure 2: An example of an MI application (modified from geosoft.com)

1.3 Research Contributions

The aim of this thesis is to develop practical analytical and simulation models of magnetic coupling and/or electromagnetic radiation across an air-water interface. The primary focus is the development and evaluation of a Finite-Difference Time-Domain (FDTD) simulation tool that allows users to characterize sinusoidal tones, pluses, as well as the potential for wideband modulated signals. The simulation tool is flexible and takes takes into account the effect of the hardware front ends. The coil geometries and orientations can be modified by the user, and the underwater channel and air-water interface can be configured to any application. Using this, the optimal frequency at which a set of coils provides maximum capacity for given system level parameters can be obtained. The FDTD simulation tool is compared and validated against existing analytical models.

There were three works that occurred during the development of this thesis that would be deemed significant enough to be classified as being contributions to the relative scientific space: two accepted conference papers and the choice to make the FDTD simulation tool available for collaboration with other researchers on the *www.uwstream.com* website. It is the intention of both the author and supervisor that the field experiments will be conducted in late Summer or early Fall and the results put into at least one paper. It

should be noted that both conferences were postponed due to the global COVID-19 pandemic.

1.1.1 OCEANS 2020 Singapore

Mark Watson was the main author of the conference paper entitled “Magnetic Induction for Communication Across the Air-Water Boundary”. This paper was written and submitted early in the development of the FDTD simulator and was accepted into the regular Technical Program at OCEANS 2020 Singapore on January 25, 2020. The paper describes the development of the FDTD simulation tool along with Adam Forget’s analytical model and proceeds to describe the plan for the eventual field experiments. Forget’s model will be discussed later in this thesis.

1.1.2 UCOMMS 2020 (Non-acoustic Underwater Communication)

Mark Watson was the main author of the conference paper entitled “Evaluating the Feasibility of Magnetic Induction to Cross the Air-Water Boundary”. This paper includes the results discussed in this thesis and was accepted into the Non-acoustic Underwater Communication Session at UCOMMS 2020 on June 8, 2020. Following the peer review process, the paper was revised, and the final version submitted on July 31, 2020. The paper presents the development of a custom FDTD simulation tool, shows the validation of the FDTD simulator using the Wait’s Sommerfeld integral, and predicts the induced voltages, signal-to-noise ratios, and channel capacities for several coil orientations.

1.1.3 FDTD Tool Available Online

Although the FDTD simulation in its current form is intended for one specific use case, it is still quite configurable with the potential to be adapted to other problems or modified to include additional features. For example, the conductivity and permittivity of the water can be disabled, and the coils miniaturized and brought closer together to simulate RFID tags. The input can be modified to be a modulated digital signal and the throughput and Bit Error Rates (BER) evaluated with the appropriate demodulation scheme. Another application may be to wireless power transfer problems or almost any other problem involving coupled coils or loop antennas. As such, the FDTD simulator will be made

available, open-source, at *www.uwstream.com*. The tool may be used by students or anyone interested in learning a relatively straight-forward implementation of the FDTD method. Researchers may see applications of the FDTD tool to their research and choose to apply it to their work with appropriate reference to Mark Watson at the UW-Stream Lab, Dalhousie University.

1.4 Literature Review

The problem of mathematically modelling electromagnetic (EM) fields in a domain which includes an air-water interface is very challenging and has been studied since the early 1900s. Early pioneers on the study of EM fields in conductive media were A. Sommerfeld, H. Weyl, K. A. Norton, and C. T. Tai who were primarily interested in studying fields in an *infinite* conductive medium. Most of their work occurred at or around the time of the first world war prior to the 1950's. In the 1950's and 60's, scientist and engineers began to study the problem of a *non-infinite* conductive medium. Much of the work used to validate the FDTD simulator is based on the Sommerfeld integral.

In 1961, R. K. Moore and W. E. Blair studied electric and magnetic dipole radiation in a conductive half-space. The resulting mathematical expressions are quite complex and involve the evaluation of Sommerfeld integrals. Moore and Blair were not interested in communication from underwater to air, but rather they developed their analysis on point-to-point underwater communication. Moore appears to be the first to describe what is later called the "up-and-over" path which includes the generation of surface EM waves. Further, Moore's work also assumes that since the conductivity of seawater is relatively high, the displacement current is negligible compared to the conductive current. This assumption produces an interesting result: the damped wave equation derived from Maxwell's equations can be approximated by a diffusion equation. This is discussed in other literature and is one of the interesting phenomena observed in this thesis.

In a discussion on submerged antennas in a lossy medium, the purpose of the 1962 work of R. C. Hansen is to give engineers tools which obscure the complicated Sommerfeld integrals, Bessel functions, etc. associated with the analysis of Maxwell's equations

applied to EM fields in a conductive medium. Hansen looks at approximate field solutions for the cases of quasi-static, near field, intermediate field, and far field for the case where both antennas are submerged either underground or underwater. The analytics are mostly focused on electric dipoles; however, figures of merit are presented for the case of the loop antenna including radiation resistance. Hansen's heuristic description of the physics of submerged antenna coupling is insightful.

Moore again discusses radio communication in oceans applications in a 1967 paper published in IEEE Spectrum. As is common in much of the analytical work, the analysis is based upon plane waves in a conductive medium. He differentiates the attenuation effects of high versus low frequency signals. When the frequency is high enough such that the displacement current is large compared to the conduction current, the skin depth of a wave in a conductive medium becomes negligible for most communication systems. This results in the damped wave equation being approximated by the undamped wave equation. For low frequency signals, Moore states approximate attenuations of 8.7 dB per skin depth, or 55 dB per wavelength. However, since this derivation is based on the use of plane waves, the fields are already assumed to be radiating rather than coupled via capacitive or magnetic induction. Moore discusses the propagation of EM plane waves from air to underwater; however, he is mostly concerned with the transverse mode of propagation which allows for longer subsea communication distances. Moore's formulation is based upon matching the boundary conditions at the air-water interface. The result is that the Poynting vector reduces by a factor of 1/1000 due to the electric field component decreasing by the same amount (the magnetic field component is unchanged).

In an interesting and practical 1987 paper, L. Butler discusses underwater radio communication and provides simple frequency and conductivity dependent algebraic expressions for estimating losses due to the propagation of fields underwater and across the air-water interface. Butler also discusses, briefly, atmospheric noise and provides some rule of thumb estimates. Originally, the intention was to use Butler's equations as a means of validating the FDTD simulator; however, the origin of Butler's equations were

not found; instead, other more accurate ways to accomplish this, so Butler's methodology was not used.

In 1998, R. H. Tyler, T. B. Sanford, and M. J. Unsworth published a paper on the study of the propagation of electromagnetic fields in the costal ocean. Tyler et al derive expressions from Maxwell's equations for the damped wave equation and differentiate between the manifestation of wavelike behaviour due to large displacement currents and diffusive properties when conduction currents dominate (i.e. as in the case of electromagnetic fields in a good conductor).

The 2003 PhD dissertation by D. Gibson is one the main pieces of work used in this thesis. Although not focused on underwater communication, Gibson characterizes a subsurface channel and designs a system based on magnetic induction for subsurface communications for mining applications. Gibson uses analytical models of varying complexity to derive an optimum system frequency and antenna orientations. Gibson provides MATLAB code for his numerical evaluation of the complicated Sommerfeld integrals, and his code is modified for this application and included in this thesis. Gibson presents a model for atmospheric noise, and his noise model is also used in this thesis. Gibson describes the design of a wide-band low-frequency channel sounder used to characterize and evaluate a given channel. Apart from the specific contributions made by Gibson which have been applied to this thesis, Gibson does an excellent job at providing insight on numerous relevant topics some of which will be discussed in this thesis. These topics include near vs far fields effects, quasi-static diffusion vs radiation, and important loop antenna parameters, just to name a few.

A 2005 paper by L. O. Loseth, H. M. Pedersen, B. Ursin, L. Amundsen, and S. Ellingsrud discusses the diffusion of electromagnetic fields in a conductive medium. Mathematically, the damped wave equation includes a damping term which is a function of the conductivity of the medium. If the damping term dominates, as is the case at low frequency, the wave equation becomes a diffusion equation. As a result, electromagnetic pulses become distorted. This paper was published in the Society of Exploration

Geophysics, so the work is focused on the use of magnetic induction in underground applications; therefore, crossing of an air-water interface is not included.

C. Uribe and W. Grote wrote a paper in 2009 on the development of a radio communication model for underwater wireless sensor networks. Although not focused solely on magnetic induction, their aim is to develop models for high bandwidth systems using electromagnetics underwater. They indicate attenuation occurs primarily in the near fields of transmitting antennas with little loss occurring thereafter. They propose a model for the attenuation factor which is a function of distance and matches measurements in both the near and far fields.

In a fascinating 2011 paper published by the Swedish Defence Research Agency – Division of Defence and Security, Systems, and Technology, L. Abrahamsson develops both analytical and FDTD based models of electromagnetic fields crossing the air-water interface. Abrahamsson's attention is mostly on the analysis of the lateral wave component for the purpose of extending transmission distance. Abrahamsson touches on the diffusion of the electromagnetic fields underwater and the propagation in air. The analytical model is developed using the damped wave equation and applying appropriate boundary conditions using reflection and transmission coefficients then applying Green's function and arriving at the Sommerfeld integral. Abrahamsson concludes the FDTD method is capable of accurately reproducing air-water interface effects with good fidelity. He touches on the importance of making the computational domain large enough to avoid the interaction between the absorbing boundary condition with the interior fields, which is something observed in this thesis and cannot be understated.

In 2012, B. Gulbahar and O. B. Akan develop and analyze a model of a magneto-inductive underwater channel. They use the approach of developing an equivalent circuit model based on the mutual inductance between two coils. They do not study the effects of crossing the air-water interface.

The 2012 work by M. C. Domingo is a study of the use of magnetic induction for an underwater wireless communication network. Again, her approach is the development of an equivalent circuit model based on the mutual inductance between two coils. She derives an expression of the path loss which includes one term representing losses due to the loading of the coupled system on the transceiver and another term representing the skin depth effects. She compares this model with other models based on the use of acoustic and RF energy. Domingo also proposes a relay system based on the use of a string of passive coils for the purpose of extending the range of an MI-based system.

H. Wang, K. Zheng, K. Yang, and Y. Ma derive expressions for electromagnetic fields in air produced by a magnetic dipole immersed in the sea in a 2014 paper published in the IEEE Transactions on Antennas and Propagation. Their results are tested experimentally at a frequency near 19 kHz. This paper provided the inspiration for the approach of this thesis: to develop a model to predict the performance of a MI-based system crossing the air-water interface and then to perform experiments to validate the results of the model. The objective in the paper by Wang, Yang, and Ma is to maximize the lateral distance at a given transmitter depth, operating frequency, and receiver height where as the purpose of this thesis is to maximize transmitter depth with the receiver coil located directly overhead, at a fixed height in air, while maintaining sufficient bandwidth and data rates.

A 2015 paper by H. Guo and Z. Sun describes the development of an underwater channel model based on the use of magnetic induction. They argue that the previous work of Domingo neglects the effects of the lossy medium on the mutual inductance between the two coils. This paper treats the transmitting coil as a magnetic dipole. They show how a tri-directional coil radiates like an isotropic radiator. In this paper, Guo and Sun do not study the case where the receiving coil is in air, but the air-water interface is included such that reflected and lateral waves are included in their model. They use the analytical models of the radiated fields to find the mutual and self inductance between the two sets of coils which is then use it to develop an equivalent circuit model of the channel. This is a common approach for analytical models.

Y. Wang, A. Dobbin, and J.F. Bousquet from Dalhousie University were able to demonstrate, in a 2016 paper, magnetic induction used in the development of a low-power underwater modem capable of achieving data rate of 8 kbps at 22.5 kHz over a distance of 10 meters in seawater at just 1 Watt. Their circuit model is based on the work of Domingo which includes a term that represents mutual inductance between the two sets of coils, and losses are modelled based on skin depth. The system is completely underwater and does not consider the effects of fields crossing the air-water interface.

The 2016 textbook Antenna Theory: Analysis and Design (4^{th} edition) by C. A. Banalis develops fundamental tools for analyzing loop antennas. The fields from a current carrying circular loop are provided in this thesis and based on the derivation demonstrated by Banalis.

2018 S. Zhang, X. Tu, K. Zheng, M. Yang, and L. Xu study the radiation of electromagnetic fields across the air-water interface using the FDTD method. Their approach is quite different from the method used in this thesis. Zhang et al use what is called a Total-Field Scatter-Field source (TFSF-FDTD) which simplifies the model and reduces the number of time steps required to complete the simulation. The FDTD method used in this thesis is a direct numerical evaluation of Maxwell's equations over the entire computational space resulting in long run times. The TFSF-FDTD approach is a newer more modern technique which consists of applying TFSF boundary conditions at the water's surface - which are called the scatter-fields and are derived using analytical expressions - and then modelling the total-fields in air only. They compare their TFSF-FDTD results with that of the Sommerfeld integral which is part of the validation used in this thesis as well.

In 2018, B. Chai, X. Zhang, and J. Wang published a paper describing experiments of a magnetic induction-based communication system across an air-water interface. Their tests consisted of transmitting energy from air into the water. They transmitted data using Frequency Shift Keying (FSK) modulation from 4 to 40 Hz. At a transmitter height of 2 meters and a receiver located up to a depth of 35 meters, they were able to achieve error

free communication. The system studied and tested in this thesis is intended to operate at a much higher frequency range (~ 100 kHz) resulting in a much larger bandwidth.

Finally, an interesting 2018 paper by F. Tonolini and F. Adib describes the development of an alternative technology for transmission of information across an air-water interface. The system is called Translational Acoustic RF Communication (TARF). The technology is rather new and quite immature but is fascinating nonetheless. The system works by using acoustic energy to vibrate the water's surface. A radar system then analyzes the ripples on the surface and uses signal processing methods to extract the phase changes in the vibrations to decode them and recover the transmitted data.

1.5 Organization of Thesis

Chapter 2 will provide a review of fundamental electromagnetic theory, communication system evaluation, and important loop antenna parameters. Maxwell's equations are fundamental to this branch of physics and electrical engineering; in fact, the FDTD simulation tool developed here is based on the finite-difference form of two of Maxwell's four equations. Maxwell's equations are used to derive expressions intended to facilitate a better understanding of the physics of electromagnetic fields underwater and across the air-water interface. This thesis is based on the use of magnetic induction as a means to reduce the attenuation of electromagnetic fields underwater. To support this, the theoretical framework is developed to distinguish important characteristics of the fields as they develop and change around the transmitting loop antenna.

Chapter 3 provides a thorough description of the simulation tool developed for this thesis. The tool consists of three main functional blocks, and the operation and implementation of each part will be described in detail. The channel model is perhaps the most important functional block, and it certainly involves the most complicated algorithms based on the FDTD method; therefore, the FDTD method will be introduced and described in detail.

Chapter 4 will explain how other analytical models and field experiments are be used to compare with the results of the simulation tool developed as part of this thesis. In an

attempt to validate the base FDTD algorithm, a test is performed to measure and compare the frequency content of a pulse generated inside a cavity. Another test used to evaluate the application of FDTD in cylindrical coordinates is to simulate the fields around a single loop of wire, with no water present, to be compared with the simple analytic model. The final validation is based on the work of Wait and Forget. The analytical work of Wait and Forget will be explained and used to show how fields decay in the transmitting antenna's near-field in the presence of an air-water boundary.

Chapter 5 will explain how the FDTD simulation results compare with the other models described in Chapter 4. The performance of MI system is then hypothesized.

2 Review of Theory

The purpose of Chapter 2 is twofold: first, to provide interested readers with an introduction to the fundamental physics and mathematical formulations necessary to understand these works; and second, to present the important elements on which this thesis is based. Reading the works of other researchers was extremely satisfying, insightful, and instrumental throughout the development of this thesis, so it is very important to be able to potentially do the same for future students working in the field of magnetic induction based underwater communication systems, the development of FDTD-based computational electromagnetics simulation tools, or electromagnetic phenomenon in general. In addition, there are important distinctions to be made here which relate to the fundamental physics of electromagnetic interactions which have direct consequences on the communication system performance. This chapter will attempt to emphasize these points.

This chapter will begin by reviewing Maxwell's equations and then their application to loop antennas and electromagnetic fields in seawater. This will be followed by methods for evaluating the communication system based on noise, signal to noise ratio, and channel capacity. Next, since the communication system studied here is based on the use of loop antennas, the basic theory of RLC circuits will be briefly reviewed. Finally, an introduction to finite differences will be presented.

2.1 Maxwell's Equations

Maxwell's equations are a set of four equations which describe the behaviour of electric and magnetic fields $\vec{E}$ and $\vec{H}$, respectively. This set of equations consist of Gauss' law for electric and magnetic fields, Faraday's law, and Ampere's law. While Maxwell's equations are fundamental to understanding the physics of electromagnetic fields, this is not the only approach to this field of study. Quantum Electrodynamics (QED) is said to be the most accurate physical model in all of physics; however, the QED branch of modern physics views electromagnetism as the interaction between fundamental fields

and particles rather than as continuous fields, as is the case in the more traditional electromagnetic field theory described by Maxwell's equations. It is the traditional electromagnetic field theory described by Gauss, Faraday, Ampere, and Maxwell used throughout this thesis, so Maxwell's equations will be reviewed here.

Maxwell's equations can be expressed in integral or differential form. The differential form is presented below in Equations 2.1 through 2.4. It should also be noted that this representation of Maxwell's equations is for isotropic, homogeneous, non-dispersive, time invariant, and linear material; otherwise the constitutive relations $\vec{D} = \varepsilon\vec{E}$ and $\vec{B} = \mu\vec{H}$ and more complicated expressions for ε and μ would need to be used. While the inclusion of $\vec{D}$ and $\vec{B}$ represent a broader set of problems, the simpler expressions shown below are sufficient for the purpose of this work and are used throughout this thesis.

$$\nabla \cdot \vec{E} = \frac{\rho_v}{\varepsilon} \tag{2.1}$$

$$\nabla \cdot \vec{H} = 0 \tag{2.2}$$

$$\nabla \times \vec{E} = -\mu \frac{\partial \vec{H}}{\partial t} \tag{2.3}$$

$$\nabla \times \vec{H} = \vec{J} + \varepsilon \frac{\partial \vec{E}}{\partial t} \tag{2.4}$$

Equations 2.1 and 2.2 are known as Gauss' laws for electric and magnetic fields, respectively. Simply put, the former describes how the divergence of electric field lines depends on the existence of charged particles (ρ_v can be positive, negative, or zero), respectively, while the latter states the opposite for magnetic fields. More specifically, the amount of electric flux through an arbitrary Gaussian surface may be non-zero depending on if an electric charge is contained within the volume enclosed by the surface. The same cannot be said for magnetic fields since magnetic monopoles do not exist.

Equations 2.3 and 2.4 show the coupling between electric and magnetic fields and are the basis of the full-wave FDTD simulation tool described in this thesis. Equation 2.3 is known as Faraday's law. Faraday's law describes the relationship between electric fields and time-varying magnetic fields. Equation 2.4 is known as Ampere's law which describes how magnetic fields are related to current sources, $\vec{J}$, and/or time-varying electric fields, $\frac{\partial \vec{E}}{\partial t}$ (also called *displacement current*). An important distinction which will be expanded upon later, is the case where the medium is conductive, with conductivity σ, such that the moving charges are the result of the electric field itself, which in such a case is $\vec{J} = \sigma \vec{E}$.

2.1.1 Magnetic Induction

Magnetic induction is a physical phenomenon which illustrates the coupling of electric and magnetic fields. In 1831, Michael Faraday made an observation that would forever change the landscape of science and engineering. Faraday, a keen experimentalist, noticed that by moving a magnet near a stationary piece of wire, the changing magnetic field could generate a voltage in the wire. The mathematical formulation of this phenomenon can be expressed in a few ways; Equation 2.5 is commonly known as Faraday's law and represents one such form. Faraday's law describes how electric fields, $\vec{E}$, are generated by time-varying magnetics fields, $\vec{H}$.

$$\nabla \times \vec{E} = -\mu \frac{\partial \vec{H}}{\partial t} \tag{2.5}$$

Another common representation of Faraday's law is shown in Equation 2.6. This formulation is more intuitive as it excludes the use of the electric and magnetic field vectors which are generally not known in practice. Equation 2.6 relates the induced voltage, V_{emf}, with a time-varying magnetic flux, Ψ.

$$V_{emf} = -\frac{d\Psi}{dt} \tag{2.6}$$

Both forms of Faraday's law presented here are used at various points in this thesis, depending on the application, as will be explained in Chapter 3. Further, Equation 2.5 can be derived from 2.6 by using $\frac{d\Psi}{dt} = \mu \iint_S \frac{\partial \vec{H}}{\partial t} \cdot d\vec{S}$ and $V_{emf} = \oint_l \vec{E} \cdot d\vec{l}$ and then applying Stokes' theorem: $\oint_l \vec{\psi} \cdot d\vec{l} = \iint_S (\nabla \times \vec{\psi}) \cdot d\vec{S}$.

Magnetic induction is the working principle in the operation of electrical transformers. In the simplest sense, transformers are, of course, two coils of wire coupled by a magnetic interaction. An alternating current in one coil generates magnetic fields which cross the cross-sectional area of the secondary coil. According to Faraday's law, there will be voltages and currents induced in the second coil. This is the basis of the magnetic induction communication system discussed in this thesis. The mutual induction between two coils will be described next.

2.1.2 Mutual Inductance

When the magnetic fields generated by currents flowing in one coil result in an induced current in a secondary coil, and if the induced current results in a magnetic field which interacts with the primary coil, then it can be said that the two coils have become coupled. This coupling can be quantified by a parameter called mutual inductance, M. The mutual inductance describes the magnetic interaction between the two coils. Mutual inductance is not a fundamental property, rather it is a mathematical construct defined by

$$M_{12} = \frac{\Psi_{12}}{I_2} \tag{2.7}$$

where M_{12}, Ψ_{12}, and I_2 are shown in Figure 3. M_{12} describes the magnetic coupling of secondary coil (on the right) on the primary (left) due to the induced current I_2. Ψ_{12} represents the magnetic flux through the primary coil due to the secondary coil.

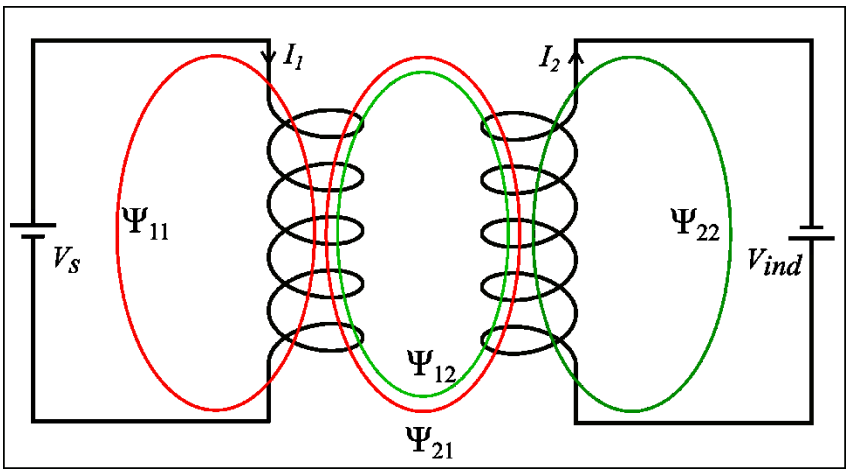

Figure 3: Mutual inductance of two coils

Similarly, the ratio of the magnetic flux linking the secondary coil due to the primary to the driving current in the primary is defined as

$$M_{21} = \frac{\Psi_{21}}{I_1} \tag{2.8}$$

Where Ψ_{21} represents the magnetic flux through the secondary coil due to the primary, and M_{21} describes the magnetic coupling of the primary coil on the secondary due to the driving current I_1. The term "mutual inductance" comes from the equivalence of the ratios.

$$\frac{\Psi_{12}}{I_2} = \frac{\Psi_{21}}{I_1} \longrightarrow M_{12} = M_{21} = M \tag{2.9}$$

The two circuits shown in Figure 3 are coupled and this can be expressed mathematically by applying Kirchoff's voltage law to the two circuits resulting in the following system of equations which are coupled through the terms which include the parameter M (Grainger and Stevenson, 1994).

$$V_s - L_1 \frac{dI_1}{dt} - M \frac{dI_2}{dt} = 0 \tag{2.10}$$

$$V_{ind} - L_2 \frac{dI_2}{dt} - M \frac{dI_1}{dt} = 0 \tag{2.11}$$

The reason mutual inductance is being presented in this way is because much of the literature uses M when developing analytical channel models and expressions of the electromagnetic fields. The FDTD model in this thesis does not use this approach, but two of the analytical models used for validating the FDTD simulation results do.

2.1.3 Boundary Conditions

As is the case with any problem involving differential equations, the problem is not considered well-posed unless boundary conditions are defined (and initial conditions where appropriate). The field quantities $\vec{E}$, $\vec{D}$, $\vec{H}$, and $\vec{B}$ will be discontinuous at a boundary of two media or if there exists surface charge ρ or surface current $\vec{J}$ (Sadiku, 2010). The integral equation form of Maxwell's equations can be obtained by applying Green and Stokes' laws to the differential counterparts. The integral forms are often used to derive the boundary conditions for electromagnetic problems. The integral form of Maxwell's equations are shown in Equations 2.12 to 2.15.

$$\oiint_S \vec{D} \cdot d\vec{S} = \iiint_V \rho_v dV \tag{2.12}$$

$$\oiint_S \vec{H} \cdot d\vec{S} = 0 \tag{2.13}$$

$$\oint_l \vec{E} \cdot d\vec{l} = -\frac{d}{dt} \iint_S \vec{B} \cdot d\vec{S} \tag{2.14}$$

$$\oint_l \vec{H} \cdot d\vec{l} = I + \frac{d}{dt} \iint_S \vec{D} \cdot d\vec{S} \tag{2.15}$$

Using Figure 4 as a reference, consider the interface of two media with media 1 containing $\vec{E}_1$ and media 2 containing $\vec{E}_2$. We can construct a rectangle that contains part of it in media 1 and part in media 2 with side lengths Δw and Δh. Each side of the rectangle is numbered 1 to 4. We can apply Faraday's law in the form $\oint_l \vec{E} \cdot d\vec{l} = 0$, where we are assuming the fields are static. Applying the line integral to the rectangle yields $\left(E_{x,2} - E_{x,1}\right)\Delta w + \left(E_{y,1} + E_{y,2} - E_{y,1} - E_{y,2}\right)\frac{\Delta h}{2} = 0$ which simplifies to Equation 2.16 which says that the components of $\vec{E}$ tangential to the boundary of media 1 and 2 are continuous.

$$E_{x,2} - E_{x,1} = 0 \qquad 2.16$$

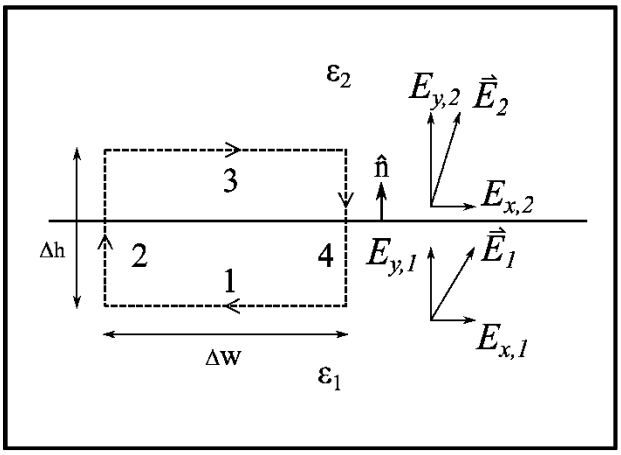

Figure 4: Electric field boundary conditions

Another way to state this is by considering a unit vector, $\hat{n}$, perpendicular to the boundary, Ω. If $E_{x,2} = E_{x,1}$, then $\vec{E}_1 - \vec{E}_2 = \left(E_{y,1} - E_{y,2}\right)\hat{y}$ which is a vector parallel to $\hat{n}$. Therefore, their cross product vanishes resulting in Equation 2.17. A similar procedure can be used to find an expression for the magnetic field which is shown in Equation 2.18. This equation says that $\vec{B}_1 - \vec{B}_2$ results in a vector perpendicular to the boundary, Ω, which indicates $B_{y,2} = B_{y,1}$.

$$\hat{n} \times \left(\vec{E}_1 - \vec{E}_2\right)\Big|_\Omega = \vec{0} \qquad 2.17$$

$$\hat{n} \cdot \left(\vec{B}_1 - \vec{B}_2\right)\Big|_{\Omega} = 0 \qquad 2.18$$

This is an incomplete picture of boundary conditions, but the interested reader can find the complete derivation in any undergraduate textbook on electromagnetism (see *Elements of Electromagnetics* by Matthew N.O. Sadiku). The boundary conditions presented here are sufficient for - and was used in - the development of the FDTD simulator and will be discussed again in Chapter 3.

2.1.4 Magnetic Fields Around a Wire

As will be discussed in Chapter 3, the FDTD tool must convert the current in the transmitting coil into a magnetic field to be injected into the FDTD-based channel model. To this end, let us briefly discuss how the magnetic field is obtained. The magnetic fields produced around a current carrying wire can be found using Ampere's law, repeated here in Equation 2.19, where $I = \iint_S \vec{J} \cdot d\vec{a}$ and $\vec{J}$ is the current density. Figure 5 shows the cross-section of a wire of radius r carrying a current I into the page. Note: cylindrical coordinates (ρ, ϕ, z) are used here and in the FDTD simulator.

$$\oint_l \vec{H} \cdot d\vec{l} = \iint_S \vec{J} \cdot d\vec{a} \qquad 2.19$$

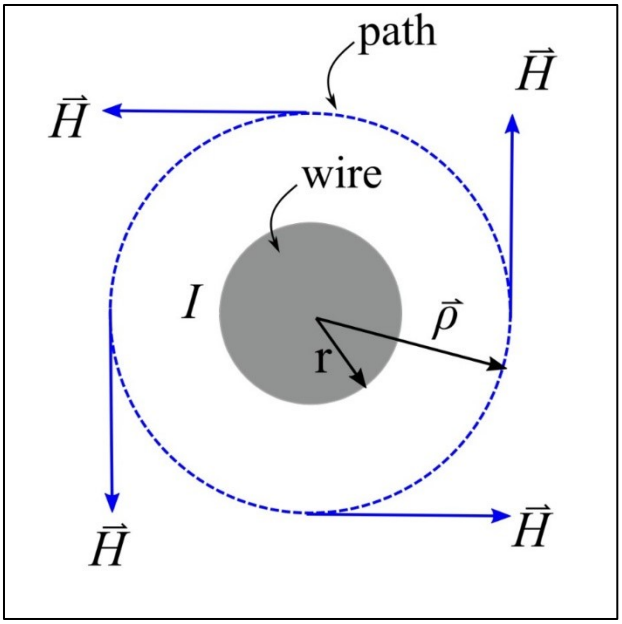

Figure 5: Magnetic fields around a current carrying wire

In order to find an analytic expression for $\vec{H}$, this problem must be broken down into two parts based on if the position vector $\vec{\rho}$ is inside or outside of the wire. When the position vector $\vec{\rho}$ is less than r, the left-hand side of Ampere's law becomes

$$\oint_l \vec{H} \cdot d\vec{l} = H_\phi \iint_l dl = H_\phi 2\pi\rho \tag{2.20}$$

because the magnetic field is constant on the curve l due to the cylindrical symmetry. The right-hand side becomes

$$\iint_S \vec{J} \cdot d\vec{a} = \frac{I}{\pi r^2} \int_0^\rho \int_0^{2\pi} \rho d\phi d\rho = \frac{I\rho^2}{r^2} \tag{2.21}$$

resulting in the following expression for H_ϕ when $0 < \vec{\rho} < r$.

$$H_\phi = \frac{I\rho}{2\pi r^2} \tag{2.22}$$

This shows how the magnetic field strength increases linearly inside the wire, from the center to the outside surface. Outside of the wire, when $\vec{\rho} > r$, the right-hand side of Ampere's law is simply I, and the left-hand side is the same as before. Therefore, when $\vec{\rho} > r$, Ampere's law becomes

$$H_\phi = \frac{I}{2\pi\rho} \tag{2.23}$$

It is Equation 2.23 which is used in this thesis to inject the magnetic field into the FDTD-based channel model.

2.1.5 The Fresnel Equations

The Fresnel equations describe the degree of reflection and transmission of a plane wave as it moves from a medium with intrinsic impedance η_1 into a second medium with an impedance η_2. If the two impedances are matched, then there will be no reflection. The reflection coefficient is used later in this thesis to develop the Absorbing Boundary Conditions (ABC) in the form of a Perfectly Matched Layer (PML). The conditions used to define a state where the reflection is zero are used in the construction of a tensor matching the impedance of the interior computational space with that of the PML. This will be discussed further in Chapter 3. Since this thesis focuses on minimizing the reflections from the PML, a derivation of the reflection coefficient will be presented here. The setup is shown in Figure 6 where the incident (denoted with a subscript i) and reflected (r) components are in medium 1 and the transmitted components (t) are in medium 2. The interface is at $y = 0$ in the xy-plane. Note that this is the Transverse Electric (TE) mode as the electric field in perpendicular to the xy-plane which is the plane of incidence in this case.

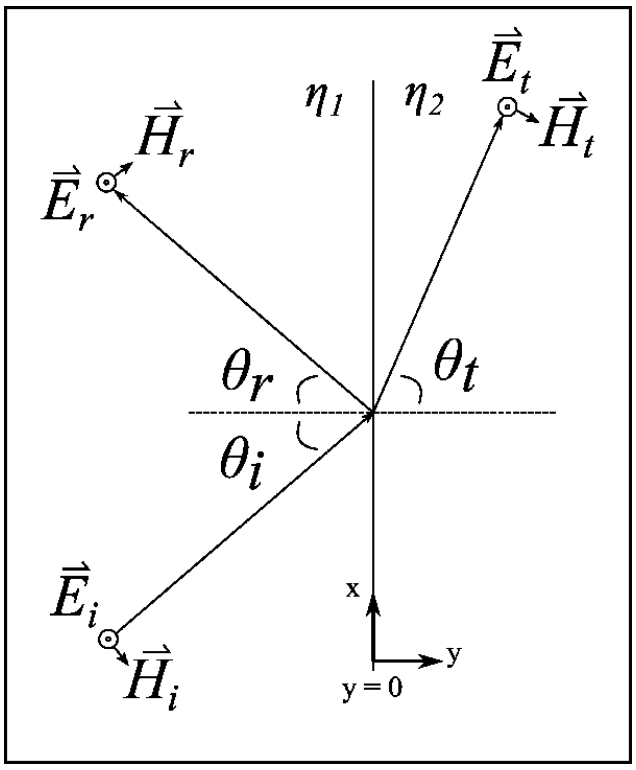

Figure 6: Plane wave behaviour at a boundary

The setup involved carefully constructing expressions for each of the plane waves shown in Figure 6. Take the incident fields for example. There will be a wave vector, $\vec{k}$, which describes the direction of the plane wave and is defined as $\vec{k} = \vec{E}_i \times \vec{H}_i$. Further, for this case, $\vec{k} = k_x\hat{x} + k_y\hat{y}$. Therefore, the incident planes waves can be defined as

$$\vec{E}_i = E_{i,0}\cos(k_x x + k_y y - \omega t)\hat{z} \tag{2.24}$$

$$\vec{H}_i = \frac{E_{i,0}}{\eta_1}\cos(k_x x + k_y y - \omega t)(-\cos\theta_i\,\hat{x} + \sin\theta_i\,\hat{y}) \tag{2.25}$$

Similarly, plane waves describing the reflected and transmitted fields can be found as

$$\vec{E}_r = E_{r,0}\cos(k_x x - k_y y - \omega t)\hat{z} \tag{2.26}$$

$$\vec{H}_r = \frac{E_{r,0}}{\eta_1}\cos\big(k_x x - k_y y - \omega t\big)(\cos\theta_r\,\hat{x} + \sin\theta_r\,\hat{y}) \tag{2.27}$$

$$\vec{E}_t = E_{i,0}\cos\big(k_x x + k_y y - \omega t\big)\hat{z} \tag{2.28}$$

$$\vec{H}_t = \frac{E_{t,0}}{\eta_2}\cos\big(k_x x + k_y y - \omega t\big)(-\cos\theta_t\,\hat{x} + \sin\theta_t\,\hat{y}) \tag{2.29}$$

At the interface where $y = 0$, the conditions of continuity are expressed as $\vec{E}_i + \vec{E}_r = \vec{E}_t$ and $\vec{H}_i + \vec{H}_r = \vec{H}_t$. The former results in

$$E_{i,0} + E_{r,0} = E_{t,0} \tag{2.30}$$

and the latter

$$\begin{gathered}\frac{1}{\eta_1}\big[\big(E_{r,0}\cos\theta_r - E_{i,0}\cos\theta_i\big)\hat{x} + \big(E_{r,0}\sin\theta_r - E_{i,0}\sin\theta_i\big)\hat{y}\big] = \cdots \\ \ldots = \frac{E_{t,0}}{\eta_1}(-\cos\theta_t\,\hat{x} + \sin\theta_t\,\hat{y})\end{gathered} \tag{2.31}$$

We can equate, for example, the x-components of Equation 2.31 and make the substitution $\theta_r = \theta_i$ (from basic optics) resulting in

$$\frac{1}{\eta_1}\big(E_{i,0} - E_{r,0}\big)\cos\theta_i = \frac{E_{t,0}}{\eta_1}\cos\theta_t \tag{2.32}$$

After making the substitution $E_{t,0} = E_{i,0} + E_{r,0}$ and rearranging, the resulting expression for the TE reflection coefficient can be readily obtained and is shown in Equation 2.33.

$$\Gamma_{TE} = \frac{E_{r,0}}{E_{i,0}} = \frac{\eta_2\cos\theta_1 - \eta_1\cos\theta_2}{\eta_2\cos\theta_1 + \eta_1\cos\theta_2} \tag{2.33}$$

Similarly, for the TM case, the associated reflection coefficient, Γ_{TM}, is

$$\Gamma_{TM} = \frac{\eta_2 \cos\theta_2 - \eta_1 \cos\theta_1}{\eta_2 \cos\theta_2 + \eta_1 \cos\theta_1} \tag{2.34}$$

A similar procedure can be followed for deriving the other part of the Fresnel equations (i.e. the transmission coefficient); but this is not relevant here. Again, as derivations are explained, one does not want to lose focus of the greater picture. The purpose of showing the reflection coefficient will become apparent when the development of the PML is shown in Chapter 3.

2.1.6 Dispersion

A very important aspect in the setup of the FDTD method involves selecting the appropriate time step. There is a limit on how large the time step can be, and this limit is called the Courant stability criterion. The limit is derived from something called the numerical dispersion relation, which is inherent in the FDTD algorithm. Therefore, it is necessary to provide a review of dispersion as it relates to physical EM plane waves. The Courant stability criterion will be discussed in Chapter 3.

Dispersion describes the relationship between the speed, frequency, and wave number of an EM plane wave (Sadiku, 2010). If the electric and magnetic fields are assumed to be in free space and consist of plane waves of the form $\vec{E} = \mathcal{R}\left\{\tilde{E}e^{j(\vec{k}\cdot\vec{r}-\omega t)}\right\}$ and $\vec{H} = \mathcal{R}\left\{\tilde{H}e^{j(\vec{k}\cdot\vec{r}-\omega t)}\right\}$, where $\vec{k} = k_x\hat{x} + k_y\hat{y}$ and $k = \sqrt{{k_x}^2 + {k_y}^2}$, then Maxwell's equations can be written in the frequency domain as

$$\vec{k}\cdot\tilde{E} = 0 \tag{2.35}$$

$$\vec{k}\cdot\tilde{H} = 0 \tag{2.36}$$

$$\vec{k} \times \tilde{E} = -\omega\mu_0\tilde{H} \tag{2.37}$$

$$\vec{k} \times \tilde{H} = \omega\varepsilon_0\tilde{E} \tag{2.38}$$

The last two equations can be combined to produce a complex valued wave equation by taking the cross-product of Equation 2.37 with $\vec{k}$ and then substituting the expression for $\vec{k} \times \tilde{H}$ from 2.38.

$$\vec{k} \times \left(\vec{k} \times \tilde{E}\right) = -\omega\mu_0\left(\vec{k} \times \tilde{H}\right) \tag{2.39}$$

$$\vec{k} \times \left(\vec{k} \times \tilde{E}\right) = -\omega^2\mu_0\varepsilon_0\tilde{E} \tag{2.40}$$

Next, we can apply the definition of the Laplacian of a vector field to the left-hand side of Equation 2.40 (i.e. $\mathrm{k}^2\vec{\psi} = \vec{k}\left(\vec{k} \cdot \vec{\psi}\right) - \vec{k} \times \vec{k} \times \vec{\psi}$ for arbitrary $\vec{\psi}$) such that

$$\vec{k}\left(\vec{k} \cdot \tilde{E}\right) - \mathrm{k}^2\tilde{E} = -\omega^2\mu_0\varepsilon_0\tilde{E} \tag{2.41}$$

And since $\vec{k} \cdot \tilde{E} = 0$, we have the equation $(\mathrm{k}^2 - \omega^2\mu_0\varepsilon_0)\tilde{E} = 0$ which implies

$$\mathrm{k}^2 = \omega^2\mu_0\varepsilon_0 \tag{2.42}$$

This is the dispersion relation for plane waves in free space. It relates the wave number, k, to frequency and speed, where the speed of light in a vacuum is given by

$$c_0 = \frac{1}{\sqrt{\mu_0\varepsilon_0}} \tag{2.43}$$

Note that since $\lambda_0 = c_0/f$, the wave number can also be expressed as $k = 2\pi/\lambda_0$. The dispersion relation given by Equation 2.42 does not take into account a lossy medium,

which is the case for the electromagnetic fields underwater. If the fourth Maxwell equation is re-written to include the conductivity of the material, σ, we have

$$\vec{k} \times \tilde{H} = (\sigma + \omega\varepsilon_0)\tilde{E} \tag{2.44}$$

And by following the same procedure as before, Equation 2.41 becomes

$$\vec{k}\left(\vec{k} \cdot \tilde{E}\right) - \mathrm{k}^2\tilde{E} = -\omega\mu_0(\sigma + \omega\varepsilon_0)\tilde{E} \tag{2.45}$$

And since $\vec{k} \cdot \tilde{E} = 0$, we have the equation $\left(\mathrm{k}^2 - \omega\mu_0(\sigma + \omega\varepsilon_0)\right)\tilde{E} = 0$ which implies another dispersion relation describing plane waves in a lossy material.

$$\mathrm{k}^2 = \omega\mu_0(\sigma + \omega\varepsilon_0) \tag{2.46}$$

The dispersion relation for lossy material shown in Equation 2.46 reverts to the expression found for dispersion relation in free-space when $\sigma = 0$ S/m. The dispersion relation is a physical phenomenon which reflects the physics of electromagnetic waves. The concept of *numerical dispersion* is somewhat abstract and only applies to the numerical computation of Maxwell's equations: not the physics (Taflove and Hagness, 2005). This introduces a source of error. In Chapter 3, the numerical dispersion will be shown to be similar to the dispersion shown here, except that the relationship between the wave number, speed, and frequency will have other dependencies on the temporal and spatial discretization which are necessary for the numerical approximation of Maxwell's equations. This will lead to an important result which effects the stability of the simulation.

2.2 Loop Antennas

In the independent works of researchers like M. C. Domingo, H. Guo, B. Gulbahar, and others, the topic of magnetic induction-based communication systems often refers to the principles of electric transformer action as the main principle of operation (although, less so in Guo). Although this formulation may yield somewhat satisfactory first-order

models, depending on the application, this thesis does not take this approach. In this thesis, the transmitting and receiving coils are viewed as loop antennas, and a full wave analysis is performed on the electric and magnetic fields through a conductive medium. A review of basic loop antenna theory is presented here. The following section will show a derivation of the fields radiated by a loop antenna. As a convenient intermediary step, the concept of a magnetic vector potential will be introduced in this section, and the vector potential will be derived using Maxwell's equations. The vector potential will then be used to find the radiated fields next. These analytical expressions are then used in Chapter 4 as part of the validation of the FDTD model.

2.2.1 Magnetic Vector Potential

Since the divergence of the curl of a vector field is zero (i.e. $\nabla \cdot \left(\nabla \times \vec{\psi}\right) = 0$ for arbitrary $\vec{\psi}$), with regards to Equation 2.2, let

$$\mu\vec{H} = \nabla \times \vec{A} \tag{2.47}$$

where $\vec{A}$ is defined as the magnetic vector potential. Substitute Equation 2.47 into Maxwell's equations 2.3 and 2.4 to yield

$$\nabla \times \vec{E} = -\frac{\partial \vec{}}{\partial t}(\nabla \times \vec{A}) \tag{2.48}$$

$$\nabla \times (\frac{1}{\mu}\nabla \times \vec{A}) = \vec{J} + \varepsilon\frac{\partial \vec{E}}{\partial t} \tag{2.49}$$

Using reasoning similar to that above, since the curl of the gradient of a scalar field is zero (i.e. $\nabla \times (\nabla\psi) = 0$ for arbitrary ψ), let

$$\vec{E} = -\frac{\partial \vec{A}}{\partial t} - \nabla V \tag{2.50}$$

such that Equation 2.48 still holds, and V is some scalar potential function. Before substituting Equation 2.50 into 2.49 and 2.1, apply the Laplace transformation (resulting in $\frac{\partial}{\partial t} \rightarrow j\omega$) to obtain

$$\nabla \times (\nabla \times \vec{A}) = \mu\vec{J} + \omega^2\mu\varepsilon\vec{A} - j\omega\mu\varepsilon\nabla V \tag{2.51}$$

$$j\omega\nabla \cdot \vec{A} + \nabla^2 V = \frac{\rho_v}{\varepsilon} \tag{2.52}$$

Applying the definition of the Laplacian of a vector field to Equation 2.51 (i.e. $\nabla^2\vec{\psi} = \nabla(\nabla \cdot \vec{\psi}) - \nabla \times \nabla \times \vec{\psi}$) yields

$$\nabla^2\vec{A} + \omega^2\mu\varepsilon\vec{A} = \mu\vec{J} + \nabla(\nabla \cdot \vec{A} + j\omega\mu\varepsilon V) \tag{2.53}$$

Now by equating the bracketed term on the right-hand side of Equation 2.53 to zero (commonly referred to as the Lorentz gauge, i.e. $\nabla \cdot \vec{A} + j\omega\mu\varepsilon V = 0$), then we arrive at what are called the *Helmholtz wave equations*:

$$\nabla^2\vec{A} + \omega^2\mu\varepsilon\vec{A} = \mu\vec{J} \tag{2.54}$$

$$\nabla^2 V + \omega^2\mu\varepsilon V = \frac{\rho_v}{\varepsilon} \tag{2.55}$$

Of particular interest here is Equation 2.54, specifically, because it describes the wave nature of the magnetic vector potential, $\vec{A}$. This equation can be solved to find $\vec{A}$, which gives $\vec{H}$ using $\mu\vec{H} = \nabla \times \vec{A}$. In the next section, the radiated $\vec{E}$ and $\vec{H}$ fields of the loop antenna will be derived from $\vec{A}$, but first, the magnetic vector potential will be found from Equation 2.54.

To this end, assume $\vec{A} = [A_x, A_y, A_z]$, we are away from the source such that $\vec{J} = 0$, and consider only the z-component of $\vec{A}$ in Equation 2.54. Then, Equation 2.54 becomes

$$\nabla^2 A_z + \omega^2 \mu \varepsilon A_z = 0 \tag{2.56}$$

At a distance far away, assume A_z is a function of r only, then in spherical coordinates, Equation 2.56 is reduced to

$$\frac{d^2 A_z}{dr^2} + \frac{2}{r}\frac{dA_z}{dr} + \omega^2 \mu \varepsilon A_z = 0 \tag{2.57}$$

For the static case, when $\omega = 0$, $A_z = \frac{C}{r}$ solves Equation 2.57. For the non-static case above, $A_z = \frac{Ce^{-j\omega^2 \mu \varepsilon r}}{r}$ is a solution. Comparing these two solutions, one can see they differ by the multiplication of a $e^{-j\omega^2 \mu \varepsilon r}$ term. Keeping this in mind, consider first the static case of Equation 2.54 when $\vec{J} \neq 0$, then

$$\nabla^2 A_z = \mu J_z \tag{2.58}$$

Which can be shown to have the solution $A_z = \frac{\mu}{4\pi}\iiint_v \frac{J_z}{r} dv$. Using the logic described above, multiplying this solution by the $e^{-j\omega^2 \mu \varepsilon r}$ term should yield the desired non-static case. Assuming this procedure holds true for the other x- and y-components, we arrive at the expression for the magnetic vector potential shown in Equation 2.59.

$$\vec{A} = \frac{\mu}{4\pi}\iiint_v \vec{J}\frac{e^{-j\omega^2 \mu \varepsilon r}}{r} dv \tag{2.59}$$

Sometimes the loop current, $\vec{I}$, is preferable to work with rather than the volumetric current density, $\vec{J}$. As such, the expression for $\vec{A}$ can be rewritten in terms of a line

integral as shown in Equation 2.60 which will be used in the next section to derive the radiated $\vec{E}$ and $\vec{H}$ fields.

$$\vec{A} = \frac{\mu}{4\pi}\int_{l} \vec{I}\frac{e^{-j\omega^2\mu\varepsilon r}}{r}dl \qquad 2.60$$

2.2.2 Radiated Fields

The radiated electric and magnetic fields of a loop antenna will be derived here using the magnetic vector potential discussed in the preceding section. The fields obtained here will be used distinguish the near and far field zones in the following section. The geometry used for this derivation is shown in Figure 7 (Balanis, 2016).

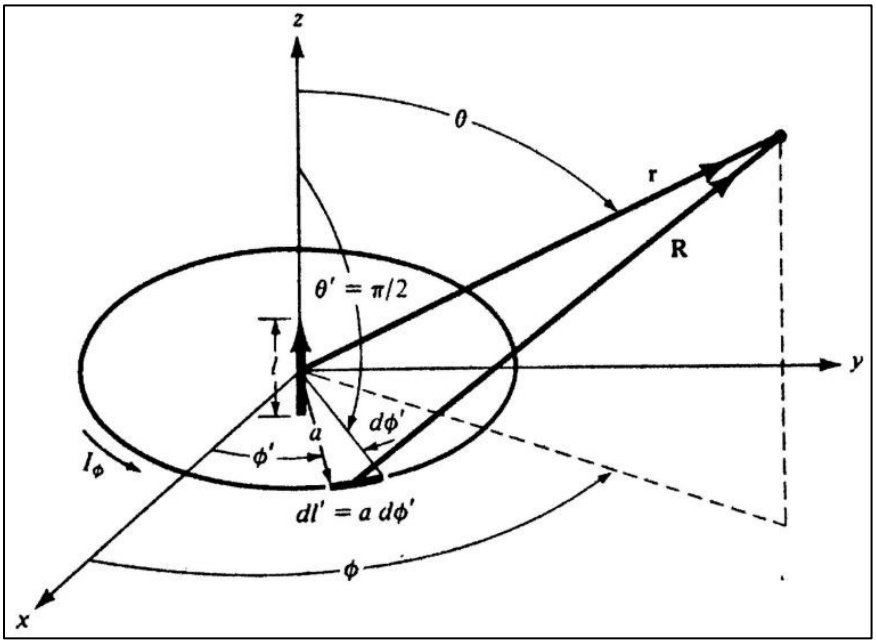

Figure 7: The geometry of a circular loop (source: Balanis)

Balanis uses coordinate transformations to write $\vec{I}$ in a mixed-coordinate form which includes both cylindrical and spherical coordinate terms because the loop is best represented in cylindrical coordinates, and the radiating fields are best expressed in terms of spherical coordinates. These transformations will be omitted here. The resulting expression is then simplified by noting $\vec{I} = I_\phi\hat{\phi}$ which results in an expression for the

loop current, $\vec{I} = I_\phi\left[\sin\theta\sin(\theta-\theta')\,\hat{r} + \cos\theta\sin(\phi-\phi')\,\hat{\theta} + \cos(\phi-\phi')\,\hat{\phi}\right]$. Further, using the geometry in Figure 7, the line integral in Equation 2.60 can be rewritten as shown in Equation 2.61.

$$A_\phi = \frac{a\mu I}{4\pi}\int_0^{2\pi}\cos\phi'\,\frac{e^{-j\omega^2\mu\varepsilon\sqrt{r^2+a^2-2ar\sin\theta\cos\phi'}}}{\sqrt{r^2+a^2-2ar\sin\theta\cos\phi'}}\,d\phi' \qquad 2.61$$

Next, the term $g(a) = \frac{e^{-j\omega^2\mu\varepsilon\sqrt{r^2+a^2-2ar\sin\theta\cos\phi'}}}{\sqrt{r^2+a^2-2ar\sin\theta\cos\phi'}}$ in Equation 2.61 can be simplified by using the first two terms of a Maclaurin series $g(a) \approx g(0) + \frac{\partial g(0)}{\partial a}a$, which is a common simplification in the analysis of nonlinear terms. To this end, this term in the integrand can be simplified to that shown in Equation 2.62.

$$g(a) \approx \left[\frac{1}{r} + a\left(\frac{j\omega^2\mu\varepsilon}{r} + \frac{1}{r^2}\right)\sin\theta\cos\phi'\right]e^{-j\omega^2\mu\varepsilon r} \qquad 2.62$$

After using this expression for g, and completing the integral in Equation 2.61, an expression for $\vec{A}$ is found and shown in Equation 2.63.

$$\vec{A} = \hat{\phi}j\,\frac{\omega^2\mu^2a^2\varepsilon I\sin\theta}{4r}\left[1 + \frac{1}{j\omega^2\mu\varepsilon r}\right]e^{-j\omega^2\mu\varepsilon r} \qquad 2.63$$

where $\omega = 2\pi f$ is in radians/sec. Equation 2.63 can then be used together with Equation 2.47 ($\mu\vec{H} = \nabla\times\vec{A}$) to obtain the magnetic field components shown in Equations 2.64 to 2.66.

$$H_r = j\,\frac{\omega^2\mu\varepsilon a^2 I\cos\theta}{2r^2}\left[1 + \frac{1}{j\omega^2\mu\varepsilon r}\right]e^{-j\omega^2\mu\varepsilon r} \qquad 2.64$$

$$H_\theta = -\frac{\omega^4(\mu\varepsilon a)^2 I \sin\theta}{4r}\left[1 + \frac{1}{j\omega^2\mu\varepsilon r} - \frac{1}{(\omega^2\mu\varepsilon r)^2}\right] e^{-j\omega^2\mu\varepsilon r} \qquad 2.65$$

$$H_\phi = 0 \qquad 2.66$$

These are the well-known magnetic field components for a radiating loop antenna (of a single turn) in spherical coordinates. The electric field can then be found using the Maxwell-Ampere equation ($\nabla \times \vec{H} = \vec{J} + \varepsilon\frac{\partial \vec{E}}{\partial t}$) but will be omitted for now since the focus of this thesis is on the magnetic coupling (although, the electric field is important when considering the attenuation due to the conductivity of the water, which will be discussed later).

Finally, in order to directly compare these analytical expressions with the results of the FDTD simulation, H_r and H_θ are transformed to cylindrical coordinates using the transformations $\rho = r\sin\theta$, $\phi = \phi$, and $z = r\cos\theta$ resulting in plots of H_ρ and H_θ for the case where $\theta = 0^\circ$ and it is assumed that as $\hat{\rho} \longrightarrow 0, \hat{r} \longrightarrow \hat{z}$; that is, we are assessing $\vec{H}$ along the axis of the coil (i.e. the z-axis). Figure 8 shows H_ρ and H_θ evaluated along the z-axis, with $f = 50$ MHz, $a = 10$ cm, and $I = 1$ A.

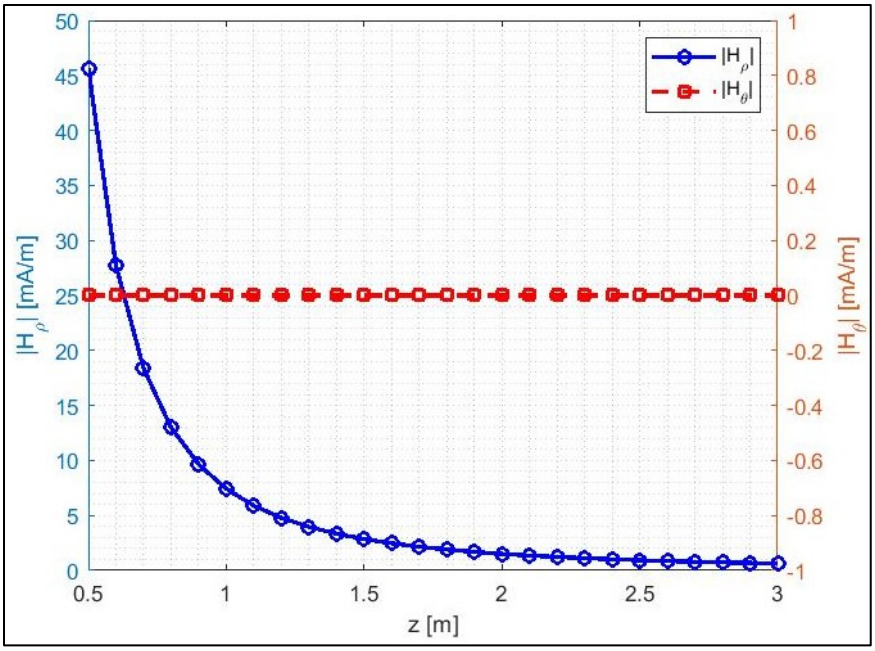

Figure 8: Plots of H_ρ and H_θ along the z-axis

2.3 Electromagnetic Fields Underwater

Compared to air, electric and magnetic fields behave quite different in seawater because of the electrical conductivity of the medium. Probably the most important effect - which likely has the most practical ramifications - is the attenuation of the electromagnetic fields as they travel through the medium. From an engineering perspective, this obviously affects the overall system performance in terms of the received power, signal to noise ratio, and data throughput. The fields also travel quite a bit slower is seawater which results in a dramatically decreased wavelength. This also has a great impact on the overall system performance, as it effects the antenna size. It also impacts the transition from the near to far field zones which determines how power is transferred and by which means (i.e. through inductive coupling or electromagnetic radiation). The air-water interface, which is a major point of emphasis in this work, causes reflection back into the incident medium, which also contributes to overall power loss.

It is a common approach to treat propagating electromagnetic fields as plane waves because the mathematical analysis becomes much simpler. The argument is such that at distances far enough away from the source, an outward traveling spherical wave can be

approximated by a flat wave front similar to how the ground you are standing on appears flat despite being on the surface of a sphere.

The general form of the common scalar wave equation is $\nabla^2\psi = k^2\frac{\partial\psi}{\partial t}$, where ψ is some scalar function of space and time, and k is called the propagation constant. Maxwell's equations can be used to derive a similar expression for the electric and magnetic fields. In a conductive media, the propagation constant is a complex quantity. The derivation is based on the textbook *Electromagnetic Waves*, by Umaran and Aziz Inan, and begins with the time-harmonic form of Maxwell's equation shown in Equations 2.67 and 2.68.

$$\nabla \times \vec{E} = -j\omega\mu\vec{H} \tag{2.67}$$

$$\nabla \times \vec{H} = \sigma\vec{E} + j\omega\varepsilon\vec{E} \tag{2.68}$$

Taking the curl of Equation 2.67 and applying the definition of the Laplacian of a vector field (i.e. $\nabla^2\vec{\psi} = \nabla(\nabla\cdot\vec{\psi}) - \nabla\times\nabla\times\vec{\psi}$ for arbitrary $\vec{\psi}$) yields $\nabla\times\nabla\times\vec{E} = \nabla(\nabla\cdot\vec{E}) - \nabla^2\vec{E} = -j\omega\mu\nabla\times\vec{H}$. Using this and $\nabla\cdot\vec{E} = 0$ from Gauss' law, Equation 2.67 can be rewritten as

$$\nabla^2\vec{E} = j\omega\mu\nabla\times\vec{H} \tag{2.69}$$

Substituting Equation 2.68 into 2.69 results in Equation 2.70 which is the desired vector wave equation for the electric field. A similar equation can be derived using the magnetic field.

$$\nabla^2\vec{E} = j\omega\mu(\sigma + j\omega\varepsilon)\vec{E} \tag{2.70}$$

Defining the complex propagation constant as γ, and comparing with the general form of the scalar wave equation discussed above, results in an expression for γ shown in Equation 2.71.

$$\gamma = \sqrt{j\omega\mu(\sigma + j\omega\varepsilon)} \tag{2.71}$$

If we let $\gamma = \alpha + j\beta$, then $\gamma^2 = (\alpha + j\beta)^2 = \alpha^2 - \beta^2 + j2\alpha\beta$. From Equation 2.71, we also have $\gamma^2 = -\omega^2\varepsilon\mu + j\omega\mu\sigma$. Equating the real and imaginary parts of these two expressions for γ^2 results in the equalities $\alpha^2 - \beta^2 = -\omega^2\varepsilon\mu$ and $2\alpha\beta = \omega\mu\sigma$. Solving for α and β can be achieved by squaring and adding the two equations for the real and imaginary parts resulting in $\alpha^4 + 2\alpha^2\beta^2 + \beta^4 = \omega^4\mu^2\varepsilon^2 + \omega^2\mu^2\sigma^2$; which, after completing the square on the left hand side, can be written as $\alpha^2 + \beta^2 = \omega^2\varepsilon\mu\sqrt{1 + \left(\frac{\sigma}{\omega\varepsilon}\right)^2}$. Finally, by adding the expressions for $\alpha^2 + \beta^2$ and $\alpha^2 - \beta^2$, Equations 2.72 and 2.73 are achieved.

$$\alpha = \omega\sqrt{\frac{\mu\varepsilon}{2}}\left[\sqrt{1 + \left(\frac{\sigma}{\omega\varepsilon}\right)^2} - 1\right]^{1/2} \tag{2.72}$$

$$\beta = \omega\sqrt{\frac{\mu\varepsilon}{2}}\left[\sqrt{1 + \left(\frac{\sigma}{\omega\varepsilon}\right)^2} + 1\right]^{1/2} \tag{2.73}$$

Here, α is defined as the attenuation constant, and β the phase or propagation constant. Underwater, due to the conductivity of the medium, small Eddy currents are generated which result it magnetic dipole moments which oppose the transmitted fields resulting in energy loss (Akyildiz et al, 2015) (Domingo, 2012). The fields decay as $e^{-\alpha x}$, where it is assumed that $x > 0$ is the distance underwater. Further, when $x = \delta$, which is called the skin depth, the fields fall off to e^{-1} when

$$\delta = \frac{1}{\alpha} \tag{2.74}$$

The phase constant has an important effect on the wavelength where the relationship is shown in Equation 2.75.

$$\lambda = \frac{2\pi}{\beta} \qquad 2.75$$

Figure 9 shows the dramatic effect of sea water on wavelength. For example, at 100 kHz, a water conductivity of 4 S/m and a relative permittivity of 81, the wavelength in air is approximately 3 km while in seawater is closer to 5 m.

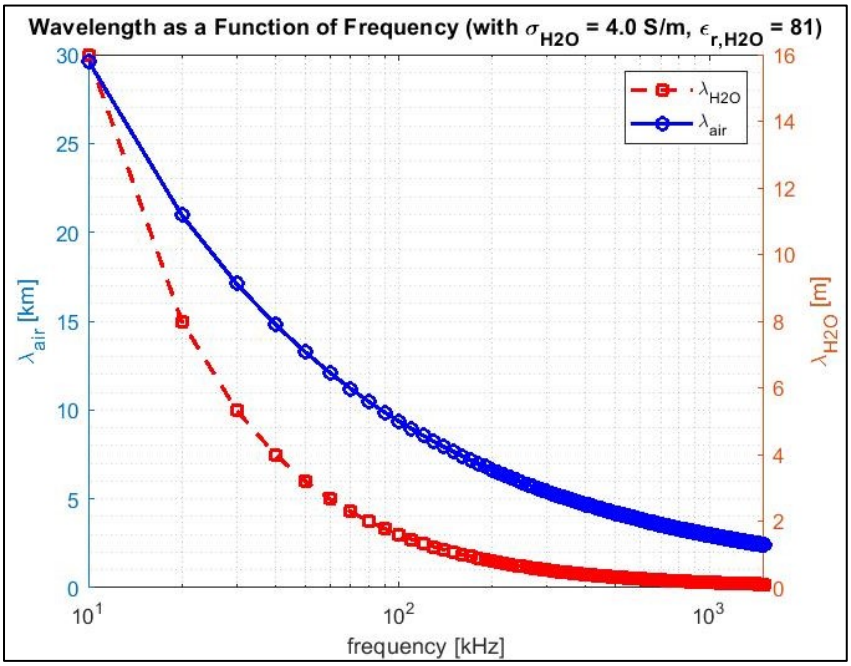

Figure 9: Comparing wavelengths in seawater to air

2.4 Communication System Evaluation

In this section, an expression for the channel capacity is presented based on predicted thermal and atmospheric noise conditions, and the voltage signal induced in the receiver. The communication system being evaluated in this thesis will be characterized based primarily on the channel capacity. The channel is assumed to be influenced by simple models of atmospheric and thermal noise. Further, the channel is assumed to experience no signal distortion. Of course, a more in-depth analysis can be performed in terms of channel characterization; however, that is outside of the scope of this thesis. This section will discuss the noise models used as part of this evaluation. Next, the signal to noise ratio will be determined. Finally, the well-known Shannon's formula will be presented in its final form.

2.4.1 Atmospheric and Thermal Noise

It is recognized that atmospheric noise produces significant interference at low frequency. According to Gibson, the atmospheric noise temperature ratio, $F_{at} = T_{at}/T_o$, reaches several hundred dBs below 10 kHz, which is well below our frequency of interest. Further, the random motion of the atoms due to heat inside the electrical components of the communication system contributes to noise in the form of thermal noise (Blake, 2002). In this work, the contribution of the thermal noise voltage, V_{th}, in the load resistance, R, at the receiver is added to the atmospheric noise, V_{at}, in the radiation resistance, R_r, for the transmitter to assess the MI link capacity. The expression for thermal noise is shown in Equation 2.76 and the equation for the atmospheric noise is shown in Equation 2.77.

$$V_{th} = \sqrt{4kT_oBR} \tag{2.76}$$

$$V_{at} = \sqrt{4kT_oBF_{at}R_r} \tag{2.77}$$

Note that k is the Boltzmann's constant ($\sim 1.3807x10^{-23}$ J/K), B is the system bandwidth, and T_o is the ambient noise temperature. The total noise voltage at the receiver is assumed to be due to the contributions of both the thermal and atmospheric

noises. The total noise voltage, V_{tot}, is determined by taking the square root of the sum of the squares of V_{th} and V_{at} since these quantities are given in RMS terms.

$$V_{tot} = \sqrt{{V_{th}}^2 + {V_{at}}^2} \tag{2.78}$$

$$V_{tot} = \sqrt{4kT_oB(R + F_{at}R_r)} \tag{2.79}$$

Where the final expression for the total noise voltage is shown in Equation 2.80.

$$V_{tot} = \sqrt{4kT_oBR\left(1 + \frac{F_{at}R_r}{R}\right)} \tag{2.80}$$

The bandwidth, B, is inversely proportional to the quality factor of the coils, Q, as shown in Equation 2.81, where f_o is the resonant frequency of the coils. The quality factor was assumed to be in the range of 5 to 10.

$$B = \frac{f_o}{Q} \tag{2.81}$$

2.4.2 Signal to Noise Ratio

To assess the channel capacity, the results of the analytical and FDTD models are used to determine the induced voltage, V_{emf}, and the bandwidth, B. To obtain the Signal-to-Noise Ratio (SNR) at the receiver, the induced voltage is used together with the thermal and atmospheric noise voltages and is expressed by Equation 2.82. This approach is based on the work of Gibson.

$$SNR = \frac{V_{emf}}{\sqrt{4kT_oBR\left(1 + \frac{T_{at}R_r}{T_oR}\right)}} \tag{2.82}$$

In this work, since the coil is small compared to the wavelength, it is assumed radiation is not the main mechanism of energy transport; therefore, the radiation resistance, R_r, is assumed to be much smaller than the load resistance, R. For example, the receiver coil has a total load resistance of $R = Nl/\sigma\alpha + 50\ \Omega\ \approx 50\ \Omega$, where the first term represents the resistance due to the coil wire, and the second term is the load resistor assumed to be $50\ \Omega$ (and l is the length of the coil, N is the number of turns, σ is the wire conductivity, and α is the cross-sectional area of the wire). By comparison, $R_r = N^2\eta\frac{8}{3}\pi^3\left(\frac{A}{\lambda^2}\right)^2$, which is small because the efficiency, η, is assumed small due to radiation not being the main mechanism of signal transmission, and the term $\left(\frac{A}{\lambda^2}\right)^2$ is also small. Using the parameters of interest in this paper, $R_r \approx 0.3\ m\Omega \ll R$. With this approximation, the main mechanism of noise is thermal noise. Finally, a minimum SNR of 10 dB is used in this work as it is often used to define the limits of barely intelligible speech (Blake, 2002).

2.4.3 Channel Capacity

The expression used to estimate the channel capacity is the well-known Shannon's formula expressed by $\tilde{C} = B \cdot log_2(1 + SNR)$. Using the equations and methodology described above, the formula used to estimate the channel capacity is Equation 2.83.

$$\tilde{C} \approx B \cdot log_2\left(1 + \frac{V_{emf}}{\sqrt{4kT_oBR}}\right) \qquad 2.83$$

Shannon's formula assumes an Additive White Gaussian Noise (AWGN) channel with no distortion (Blake, 2002), so this is considered a first-order approximation. As mentioned, a more in-depth analysis can be performed in terms of channel characterization; however, that type of detailed channel analysis is outside of the scope of this thesis.

2.5 Frequency Modes in a Cavity

The frequency content of E_z can be predicted from basic electromagnetic theory for fields in a waveguide. A brief derivation of the theoretical frequencies will be included here

with some details omitted (see Sadiku, 1994). In phasor form (time-dependence removed), Maxwell's equations can be converted to wave equations for E and H. That is, for E_z:

$$\frac{\partial^2 E_z}{\partial x^2} + \frac{\partial^2 E_z}{\partial y^2} + \frac{\partial^2 E_z}{\partial z^2} + k^2 E_z = 0 \tag{2.84}$$

where $k = 2\pi f\sqrt{\varepsilon\mu}$. The method known as separation of variables can be used to solve this Partial Differential Equation (PDE), analytically, and the results will be used later when validating the FDTD simulation algorithm. To this end, let $E_z(x, y, x) = X(x)Y(y)Z(z)$, then the PDE becomes

$$\frac{X''}{X} + \frac{Y''}{Y} + \frac{Z''}{Z} = -k^2 \tag{2.85}$$

Since each of the derivatives are with respect to their independent variables (i.e. $X'' = \frac{d^2X}{dx^2}$, etc.), and since the sum equals a constant, each of the ψ'' terms must too equal a constant (this is a key step in the separation of variables method).

Using this, let $\frac{X''}{X} = -k_x^2, \frac{Y''}{Y} = -k_y^2$, and $\frac{Z''}{Z} = \gamma^2$; thus, the PDE is now converted to three ordinary differential equations which can be readily solved. This is the advantage of using separation of variables. Substituting these solutions for $X, Y,$ and Z into $E_z(x, y, x) = X(x)Y(y)Z(z)$ yields

$$E_z(x, y, x) = (c_1 \cos(k_x x) + c_2 \sin(k_x x))\big(c_3 \cos\big(k_y y\big) + c_4 \sin\big(k_y y\big)\big)e^{-\gamma z} \tag{2.86}$$

Imposing the Dirichlet boundary conditions results in

$$E_z(x, y, x) = E_0 \sin\left(\frac{m\pi x}{a}\right) \sin\left(\frac{n\pi y}{b}\right) e^{-\gamma z} \tag{2.87}$$

The theoretical frequency modes follow and are shown in Equation 2.88.

$$f_{mn} = \frac{c}{2\sqrt{\mu_r \varepsilon_r}} \sqrt{\left(\frac{m}{a}\right)^2 + \left(\frac{n}{b}\right)^2} \qquad 2.88$$

where $a > b$ are the physical dimensions of the cavity. This equation for the frequency modes will be used in the subsequent validation of the FDTD algorithm.

2.6 RLC Circuits

The transmitter and receiver coils used in this project are configured as series resistor-inductor-capacitor (RLC) circuits, where the inductor represents the loop antenna, the capacitor is selected to allow resonance at a specific frequency of interest, and the resistor limits the coil current to avoid the potential for damage in the transmitter, and acts as a load resistor in the receiver. Since the transmitter and receiver coils are represented in this way, the basic mathematical model of the RLC circuit topology will be reviewed here. Figure 10 shows a series RLC circuit with the inclusion of a voltage source, V_{in}.

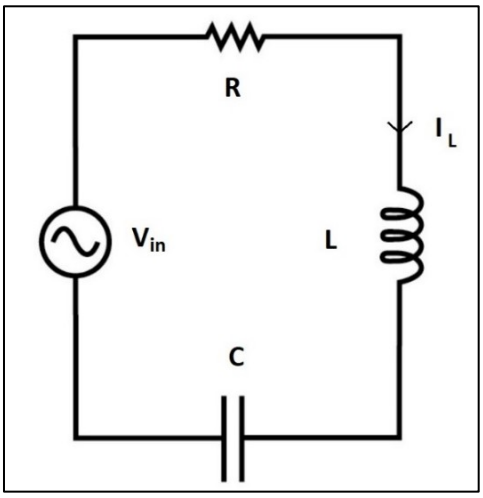

Figure 10: A series RLC circuit

The series RLC circuit shown above can be modelled using Kirchhoff's voltage law, $\sum_i V_i = 0$, defining the voltages across the resistor, inductor, and capacitor as $V_R = RI_L$,

$V_L = L\frac{dI_L}{dt}$, and $V_C = \frac{1}{C}\int_0^t I_L dt$, respectively, and differentiating once. Equation 2.89 shows the resulting second order, linear, constant coefficient, differential equation which describes the dynamics of the RLC circuit in terms of V_{in} and I_L.

$$\frac{d^2 I_L}{dt^2} + \frac{R}{L}\frac{dI_L}{dt} + \frac{1}{LC} I_L = \frac{1}{L}\frac{dV_{in}}{dt} \tag{2.89}$$

The impulse response of the RLC circuit exhibits damped oscillations due to the transfer of energy between the inductor and capacitor and the dissipation of energy due to the circuit resistance. The frequency response of the system can be either low-pass, high-pass, or band-pass. The specific frequency response is a result of the system transfer function. The transfer function depends which signals are defined as the input and output signals. For the purpose of this thesis, the input signal is V_{in}, and the output signal is I_L, the inductor current. The frequency response of this RLC circuit is band limited. In fact, the system shown above acts as a passband filter and has a resonant frequency, f_o, shown in Equation 2.90.

$$f_o = \frac{1}{2\pi\sqrt{LC}} \tag{2.90}$$

2.7 Finite Differences

Our aim to find mathematical formulations for first and second order derivatives suitable for numerical computation on a computer. This section will present the approaches used to find the finite difference representations for first and second order derivatives.

2.7.1 First Order Derivatives

We begin by looking for a way to evaluate continuous first order derivatives on a computer. To this end, we begin with the Taylor series approximation of the function $f(x + \Delta x)$ as shown in Equation 2.91.

$$f(x+\Delta x) \approx f(x) + f'(x)\Delta x + \frac{1}{2}f''(x)(\Delta x)^2 + O((\Delta x)^3) \tag{2.91}$$

One way to approximate $f'(x)$, is by neglecting the terms of order $O((\Delta x)^2)$ and simply solving for $f'(x)$ resulting in Equation 2.92.

$$f'(x) \approx \frac{f(x+\Delta x) - f(x)}{\Delta x} + O((\Delta x)^2) \tag{2.92}$$

This is considered a perfectly valid approximation to a first order derivative. This approximation is of order $O((\Delta x)^2)$ meaning that if the higher order terms are neglected, the error will decrease proportional to $(\Delta x)^2$ as Δx decreases. Although this approach is valid, we can improve upon the accuracy. First, we derive another Taylor series approximation, this time for the function $f(x-\Delta x)$.

$$f(x-\Delta x) \approx f(x) - f'(x)\Delta x + \frac{1}{2}f''(x)(\Delta x)^2 - O((\Delta x)^3) \tag{2.93}$$

Subtracting Equation 2.93 from Equation 2.91 results in Equation 2.94.

$$f(x+\Delta x) - f(x-\Delta x) \approx 2f'(x)\Delta x + O((\Delta x)^3) \tag{2.94}$$

Solving for $f'(x)$ results in the central difference form of the first derivative as shown in Equation 2.95.

$$f'(x) \approx \frac{f(x+\Delta x) - f(x-\Delta x)}{2\Delta x} + O((\Delta x)^3) \tag{2.95}$$

If the higher order terms are neglected, this approximation is of order $O((\Delta x)^3)$ meaning the error will decrease proportional to $(\Delta x)^3$. This is a big improvement over the initial approach of $(\Delta x)^2$ for small Δx. The central difference form for first order derivatives is the method used through out this work.

2.7.2 Second Order Derivatives

The approach for finding the finite difference form of second order derivatives is similar to the method presented in the previous section. We begin with the Taylor series forms of $f(x + \Delta x)$ and $f(x - \Delta x)$ as shown in Equations 2.93 and 2.91, respectively. Adding these two equations results in Equation 2.96.

$$f(x + \Delta x) + f(x - \Delta x) \approx 2f(x) + f''(x)(\Delta x)^2 + O((\Delta x)^3) \qquad 2.96$$

Solving for $f''(x)$ results in the central difference form of the second derivative as shown in Equation 2.97.

$$f''(x) \approx \frac{f(x + \Delta x) - 2f(x) + f(x - \Delta x)}{(\Delta x)^2} + O((\Delta x)^3) \qquad 2.97$$

If the higher order terms are neglected, this approximation is also of order $O((\Delta x)^3)$, and we have the approximation for second order derivatives used in this thesis.

2.7.3 Discretization

Finally, rather than working with continuous functions $f(x)$ and continuous independent variables x, where x can take on any value over the domain of interest, let us restrict x such that $x = \{x_o, x_1, \dots, x_{N-1}\}$. With this formulation, x has been discretized to a set of N discrete numbers, and $f(x_i)$ can take on any number limited only by the resolution of the computer.

As an example, refer to Figure 11. To find the central difference approximation of $f(x)$ at $x = x_1$ (i.e. the blue dotted line), Equation 2.95 can be thought of as the average of the slopes of the red and green lines. The red line has a slope from the points $(x_0, f(x_0))$ and $(x_1, f(x_1))$. It has the same form as the equation describing the forward difference approximation of the derivative at $f(x_0)$. The green line has a slope connecting the points $(x_1, f(x_1))$ and $(x_2, f(x_2))$. It has the same form as the equation describing the backward

difference approximation of the derivative at $f(x_2)$. Taking the average of these two expressions yields the expression describing the slope of the blue line.

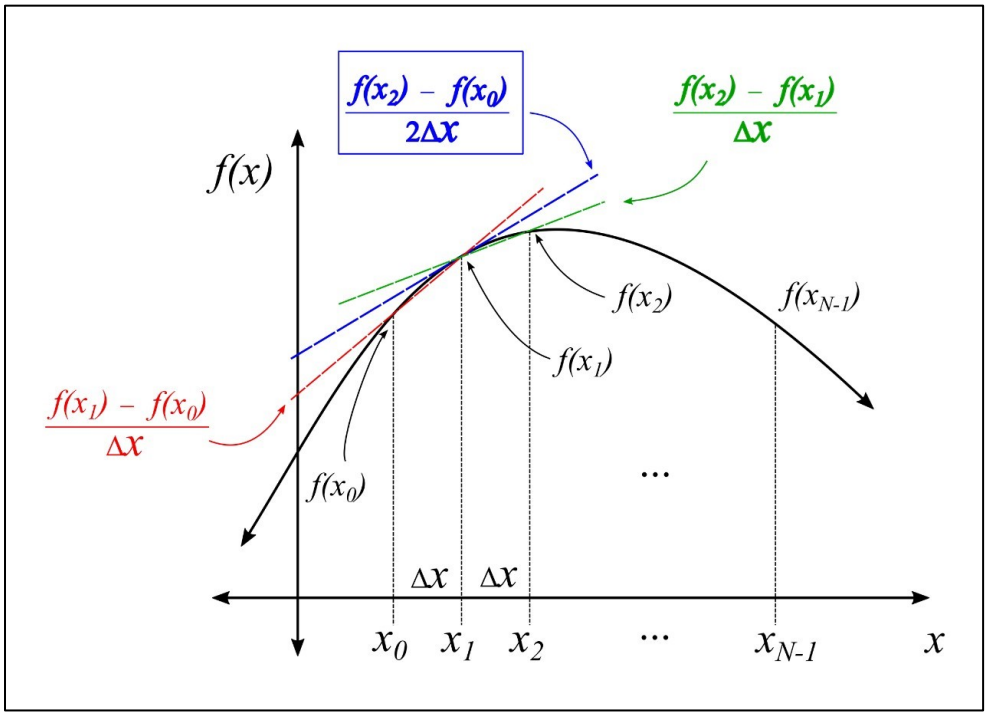

Figure 11: Central differences in approximating derivatives

3 Development of the FDTD-based Simulation Tool

The simulation tool developed in this thesis is based on the Finite-Difference Time-Domain (FDTD) method. The entire simulation tool was developed using Mathwork's MATLAB. Although some parts of the simulator do not involve FDTD, the FDTD method is a significant portion, and the channel model is based entirely upon it. The simulation tool is intended to be highly configurable for different problems involving loop antennas - using either inductive coupling or radiation mechanisms - with or without the presence of water and/or an air-water interface. Of course, the focus of this thesis is the evaluation of a magneto-inductive communication channel across an air-water interface for use in an underwater sensor network, so the focus of the development was based primarily upon this application.

This chapter will begin by providing a comprehensive overview of the general functionality of the FDTD-based simulation tool and then will expand upon the development of each of the main system components.

3.1 Overview

The FDTD simulator developed in this thesis consists of three main functional blocks: the transmitting coil, the channel, and the receiving coil. This is depicted in Figure 12. Each functional block will be introduced here and then elaborated upon in the sections that follow.

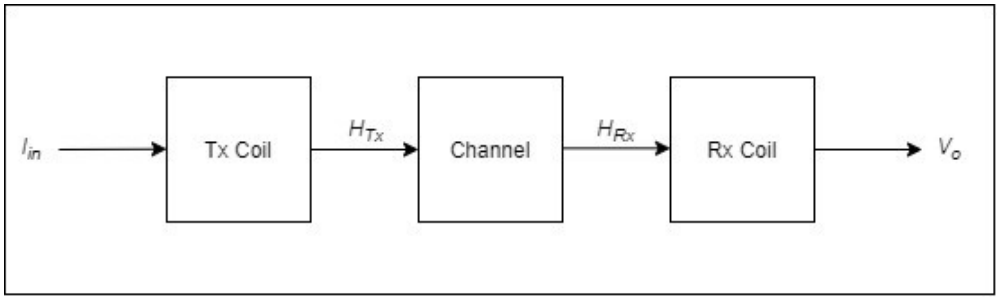

Figure 12: Block diagram of model

The transmitting coil is modelled using a series RLC circuit using finite-differences. It has the ability to simulate an arbitrary input signal including monochromatic tones and modulated signals; however, the current version of the software (Version 0.10.1) only allows for single tones using either voltage or current sources. In the case of an input voltage signal, the difference equation is solved, numerically, for the coil current. The interface between the transmitting coil and the channel model is the injection of a magnetic field into the channel. The coil current is used to calculate the magnetic field around the coil wire, as was discussed in Chapter 2.

The channel is modelled using a full-wave analysis of Maxwell's equations using the FDTD method. The material properties of the water and air are accounted for, and the resulting electric and magnetic fields are solved, numerically, throughout the entire computational space. To avoid undesirable reflections off the boundaries of the computational space, a Perfectly Matched Layer (PML) has been added to absorb the electromagnetic energy as the fields reach the edge of the domain.

Again, to interface the channel with the receiving coil, the magnetic field component perpendicular to the plane of the receiving coil is sampled, and the flux of the magnetic field through the receiving coil is calculated via numerical integration resulting in the generation of an induced voltage. This induced voltage is then used to find the current generated in the receiving coil's series RLC circuit using finite differences similar to the transmitting coil. The output voltage is the voltage generated across a load resistor.

When being used to evaluate a given problem, the simulation tool is meant to be used by interfacing with one MATLAB script called *setup.m*. In the setup file, the user can define the frequency, input voltage/current, coil orientation (horizontal/vertical), coil coordinates (x, y), water depth, domain size, water conductivity and permittivity, RLC circuit parameters, grid resolution, and more. When the user runs *main.m* a series of windows pop up which are used for debugging, viewing various simulation results, and convergence testing information. Figure 13 shows one such debug window. Figure 13 shows the setup of a problem involving two horizonal coaxial loops both with 10 cm

radii. The transmitter is located 0.5 m below the water's surface, and the receiver is 0.5 m above. The grid resolution is set to 50 mm using $N_{dim} = 2$, for illustrative purposes only. Other debug windows show how the material properties are defined, the size of the perfectly matched layer, and other information including the calculated wavelength underwater and skin depth.

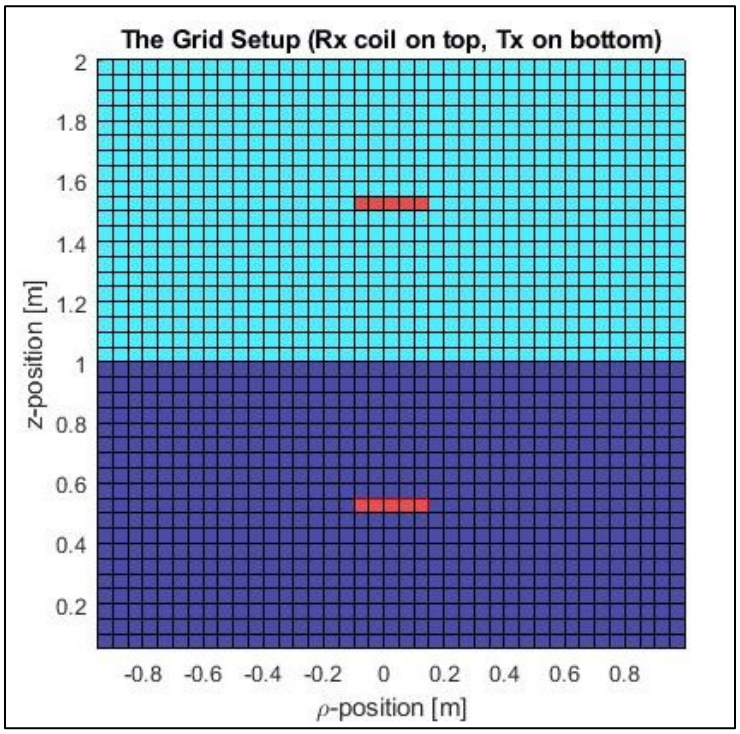

Figure 13: Setup of FDTD simulation with horizontal coaxial loops

Another configuration with can be turned on or off in the *setup.m* file is an animation of the simulation. When enabled, an .mp4 video file is generated and a screenshot of one such video is shown in Figure 14 below. The screenshot shows the problem geometry on the left - with the transmitting coil at position $(\rho, z) = (0,2)$ (in meters), the air-water boundary at $z = 3$ meters, and a receiving point located at $(0,4)$ above the water - and a view of the air-water interface with the magnitude of the magnetic field component H_z increased by a factor of 1000 (which can be configured in *setup.m*) to allow better visibility of the attenuated field as it enters the air. Note that the simulation runs much faster when the animation is switched off.

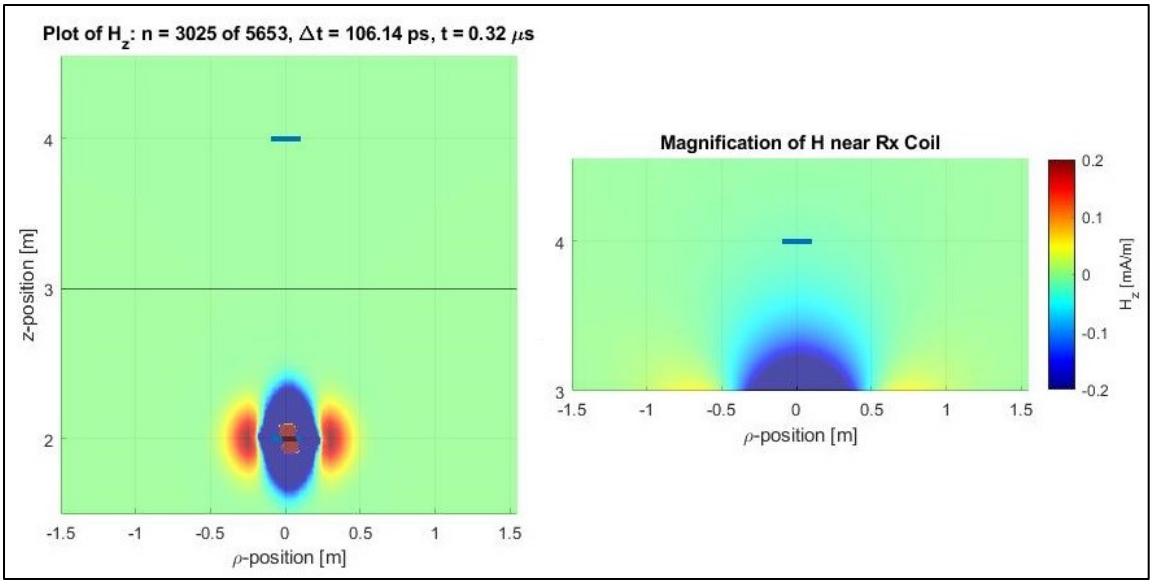

Figure 14: Screenshot of FDTD animation

Figure 15 shows another output of the simulator which appears during runtime. The top graph is the current in the transmitting coil, but if configured to have a voltage input, the input voltage would be plotted as well. The bottom plot is blank during runtime, but following the conclusion of the program, the induced voltages and current in the receiving coil is displayed.

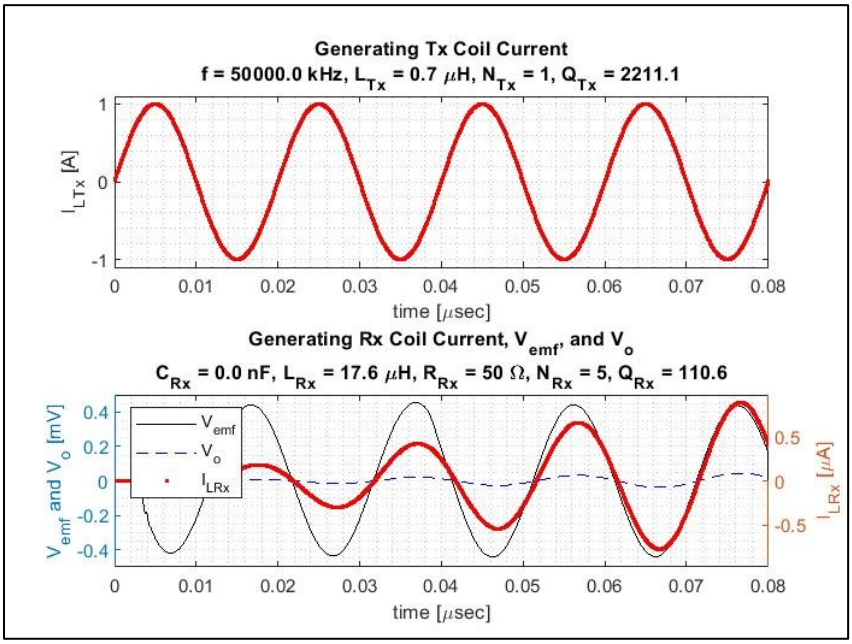

Figure 15: Input and output signals generated in the Tx and Rx coils

Figure 16 shows one of the most important outputs which appears at the end of the simulation. This data is used to validate the results of the FDTD simulation, as will be discussed in Chapter 4, for given test conditions (depth of transmitting coil, placement of coils, etc.). The graph shows the FDTD results (red circle) plotted against the results of numerically integrating Wait's Sommerfeld integral, which is one of the analytical models used to validate the FDTD-based simulation tool.

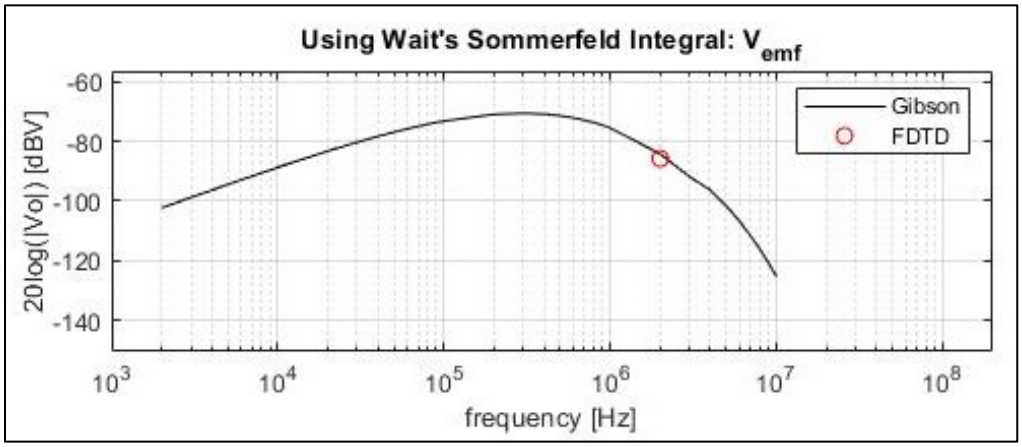

Figure 16: Output of FDTD validation using Wait/Gibson

Finally, when enabled, Figure 17 shows an example of running a convergence test. Convergence is tested by running the simulation many times at ever decreasing gird resolutions. The user defines the pass criteria and a threshold level in terms of the change is the calculated induced voltage (shown as Δ in the figure below) from one simulation result to the next. The convergence test can take a very long time if it must run through many simulations; therefore, it is up to the user to determine the acceptable level of uncertainty or error for a particular application.

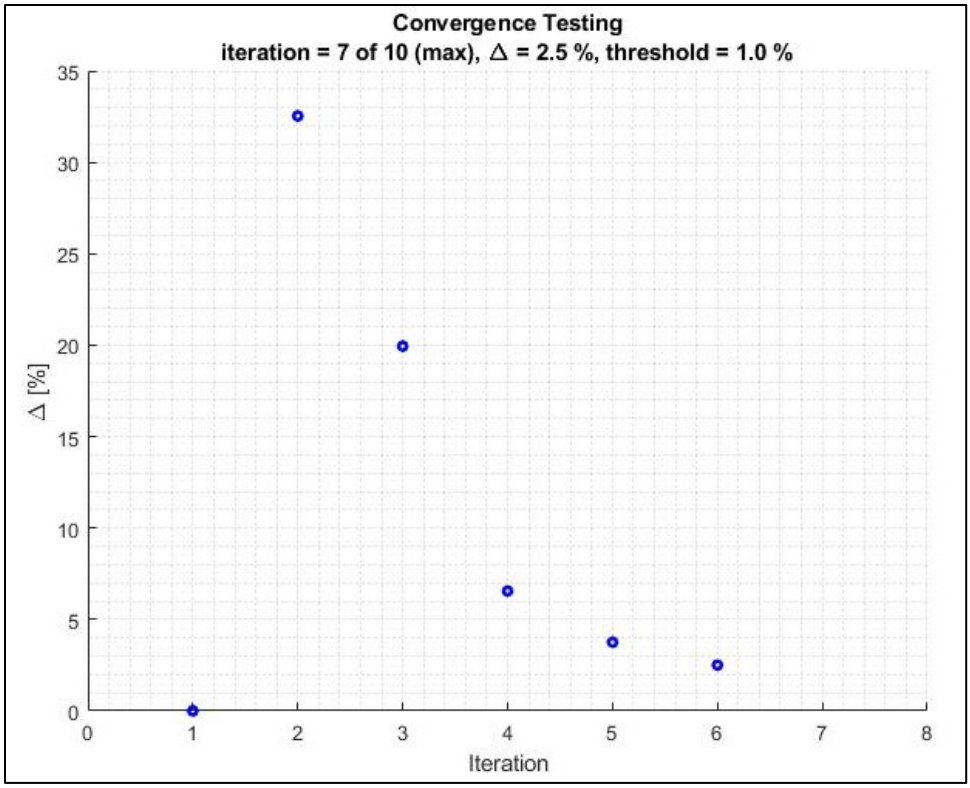

Figure 17: Example of convergence testing

3.2 Introduction to the FDTD Method

The channel model used in this thesis takes into account the material properties of the medium and the geometry of the problem, and it is based upon the numerical evaluation of Maxwell's equations over the entire two dimensional (2D) computational domain and utilizes cylindrical symmetry to simplify the implementation and to decrease the simulation time. The FDTD algorithm was developed in cylindrical coordinates, but the Cartesian coordinate system will be discussed in this introduction.

3.2.1 Update Equations in Cartesian Coordinates

Maxwell's equations are a set of four equations that describe electromagnetic phenomenon and were discussed in a previous section. The two equations that describe the interaction between time-varying electric and magnetic fields ($\vec{E}$ and $\vec{H}$, respectively) are shown in Equations 3.1 and 3.2. Note that Equation 3.2 includes a $\sigma\vec{E}$ term, where σ represents the conductivity of the medium. In water, this term is set to the commonly used value of 4 S/m (i.e. the conductivity of seawater), and in air is set to zero.

$$\nabla \times \vec{E} = -\mu \frac{\partial \vec{H}}{\partial t} \tag{3.1}$$

$$\nabla \times \vec{H} = \sigma \vec{E} + \varepsilon \frac{\partial \vec{E}}{\partial t} \tag{3.2}$$

With the cross-products expanded, the resulting six equations can be simplified by setting $\frac{\partial \psi}{\partial z} = 0$ meaning ψ does not change in the z-direction. This substitution converts the 3D problem to the desired 2D case. The resulting system of partial differential equations are shown in Equations 3.3 through 3.8.

$$\frac{\partial H_x}{\partial t} = -\frac{1}{\mu}\frac{\partial E_z}{\partial y} \tag{3.3}$$

$$\frac{\partial H_y}{\partial t} = \frac{1}{\mu}\frac{\partial E_z}{\partial x} \tag{3.4}$$

$$\frac{\partial E_z}{\partial t} = \frac{1}{\varepsilon}\left(\frac{\partial H_y}{\partial x} - \frac{\partial H_x}{\partial y} - \sigma E_z\right) \tag{3.5}$$

$$\frac{\partial E_x}{\partial t} = \frac{1}{\varepsilon}\left(\frac{\partial H_z}{\partial y} - \sigma E_x\right) \tag{3.6}$$

$$\frac{\partial E_y}{\partial t} = -\frac{1}{\varepsilon}\left(\frac{\partial H_z}{\partial x} + \sigma E_y\right) \tag{3.7}$$

$$\frac{\partial H_z}{\partial t} = \frac{1}{\mu}\left(\frac{\partial E_x}{\partial y} - \frac{\partial E_y}{\partial x}\right) \tag{3.8}$$

Equations 3.3, 3.4, and 3.5 are decoupled from 3.6, 3.7, and 3.8; thus, each set of three coupled equations can be considered independently. For this thesis, Equations 3.3, 3.4,

and 3.5 are considered. This set is referred to as the TE modes (Transverse Electric) because the electric field component E_z is completely transverse to the plane of incidence, which is assumed here to be the xy-plane.

The derivatives in time and space are approximated using finite differences. For example, the time derivative of H_x is shown in Equation 3.9, and the derivative of E_z with respect to y is shown in Equation 3.10.

$$\frac{\partial H_x}{\partial t} \approx \frac{H_x\big|_{t+\frac{\Delta t}{2}}^{i,j} - H_x\big|_{t-\frac{\Delta t}{2}}^{i,j}}{\Delta t} \tag{3.9}$$

$$\frac{\partial E_z}{\partial y} \approx \frac{E_z\big|_{t}^{i,j+1} - E_z\big|_{t}^{i,j}}{\Delta y} \tag{3.10}$$

The resulting update equations are shown in Equations 3.11 through 3.13. This is the two-dimensional FDTD form of the TE mode of Maxwell's equations. These are the update equations implemented in the FDTD algorithm used in this thesis.

$$H_x\big|_{t+\frac{\Delta t}{2}}^{i,j} = H_x\big|_{t-\frac{\Delta t}{2}}^{i,j} - \frac{\Delta t}{\Delta y \mu\big|^{i,j}}\left(E_z\big|_{t}^{i,j+1} - E_z\big|_{t}^{i,j}\right) \tag{3.11}$$

$$H_y\big|_{t+\frac{\Delta t}{2}}^{i,j} = H_y\big|_{t-\frac{\Delta t}{2}}^{i,j} + \frac{\Delta t}{\Delta x \mu\big|^{i,j}}\left(E_z\big|_{t}^{i+1,j} - E_z\big|_{t}^{i,j}\right) \tag{3.12}$$

$$E_z\big|_{t+\Delta t}^{i,j} = E_z\big|_{t}^{i,j} - \frac{\Delta t}{\varepsilon\big|^{i,j}}\left(\sigma\big|^{i,j}\left[\frac{E_z\big|_{t+\Delta t}^{i,j} + E_z\big|_{t}^{i,j}}{2}\right] + \frac{H_y\big|_{t+\frac{\Delta t}{2}}^{i,j} - H_y\big|_{t+\frac{\Delta t}{2}}^{i-1,j}}{\Delta x} - \frac{H_x\big|_{t+\frac{\Delta t}{2}}^{i,j} - H_x\big|_{t+\frac{\Delta t}{2}}^{i,j-1}}{\Delta y}\right) \tag{3.13}$$

Although not initially apparent, the spatial derivatives in the above equations are approximated using finite-differences of the order $O(h^3)$. For example, Equation 3.12 shows an approximation of the derivate of E_z with respect to the spatial variable x, where

$x = (j-1)\Delta x$. Equation 3.12 looks similar to an order $O(h^2)$ forward difference formulation of, f', where $f'(x) \approx \frac{f(x+\Delta x)-f(x)}{\Delta x}$; however due to how the grid is arranged, the approximation of $\frac{\partial E_z}{\partial x}$ is indeed order $O(h^3)$ in the FDTD method.

$$\frac{\partial E_z}{\partial x} \approx \frac{E_z|_t^{i+1,j} - E_z|_t^{i,j}}{\Delta x} \qquad 3.14$$

As an illustration of the order $O(h^3)$ of the spatial derivatives, consider the equation $H_y\big|_{n+\frac{1}{2}}^{i} = H_y\big|_{n-\frac{1}{2}}^{i} + \alpha\left(\frac{E_z|_t^{i+1,j}-E_z|_t^{i,j}}{\Delta x}\right)$, similar to Equation 3.12 but modified to be one dimensional along the x-axis, and the computational cells are shown in Figure 18.

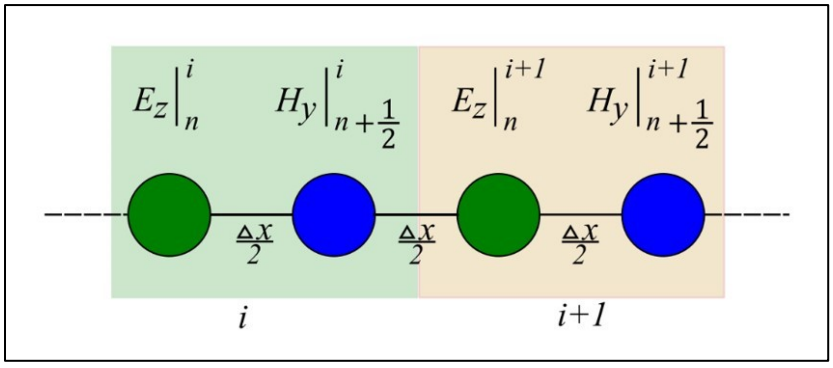

Figure 18: Central differencing on a 1D Yee cell

The H and E terms are staggered in space such that H is located a distance of $\frac{\Delta x}{2}$ from E, and the next cell $(i+1)$ is a distance Δx from the previous cell (i). The term $H_y\big|_{n+\frac{1}{2}}^{i}$ is being evaluated in the i-th cell, and if an order $O(h^3)$ central difference formula like $f'(x) \approx \frac{f(x+\Delta x)-f(x-\Delta x)}{2\Delta x}$ is used to approximate $\frac{\partial E_z}{\partial x}$, then indeed $\frac{\partial E_z}{\partial x} \approx \frac{E_z|_t^{i+1,j}-E_z|_t^{i,j}}{\Delta x}$.

3.2.2 The Yee Cell

With the discretization of Maxwell's equations over the problem space, the electric and magnetic fields are evaluated at discrete points throughout the domain. Kane Yee developed an algorithm in 1966 which is still popular today. Yee's algorithm places each

component of $\vec{E}$ inside a cell surrounded by 4 circulating $\vec{H}$ components, and vice vera. For the 2D case, in Cartesian coordinates, the cell is known as a "Yee cell" and has dimensions Δx by Δy. The $E_z, H_x,$ and H_y components are shown Figure 19 for the $(i,j)'$th Yee cell.

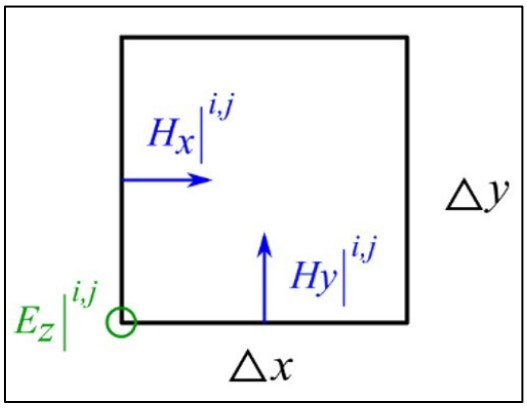

Figure 19: The 2D Yee cell defined for this problem

The computational domain is discretized into $N_x \times N_y$ cells. Figure 20 shows the case where $N_x = N_y = 2$. The electric field at node $(i+1, j+1)$ has 4 magnetic field components circulating around it, the circulation depicted in Figure 20 as a red circle. This arrangement lends itself well to Maxwell's equations which involve the curl operator, for example in Ampere's equation: $\nabla \times \vec{H} = \varepsilon \frac{\partial \vec{E}}{\partial t}$. It is easy to image the curl of $\vec{H}$ resulting in a changing electric field, $\frac{\partial \vec{E}}{\partial t}$.

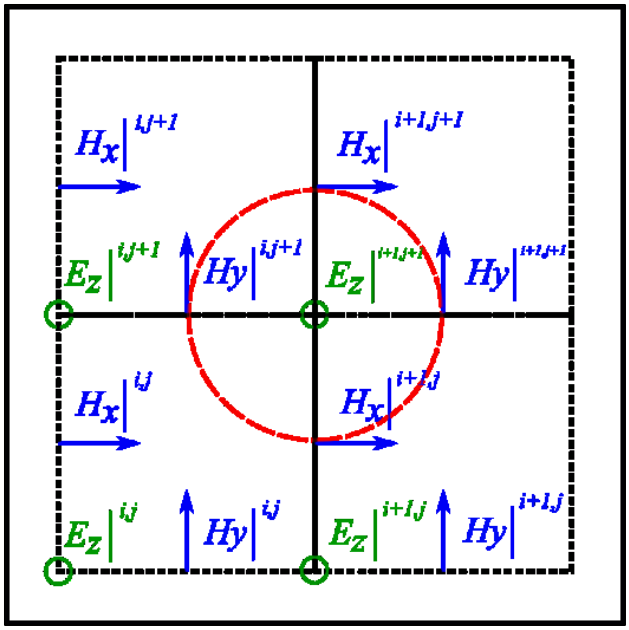

Figure 20: Yee cells and $\nabla x\vec{H}$

3.2.3 Spatial Discretization

In the course *EE5303-EM Analysis using FDTD,* Professor Dr. Raymond C. Rumpf of the University of El Paso recommends discretizing the smallest physical dimension by a factor of at least one to four Yee cells. The smallest physical dimension was resolved by a factor of $N_{dim} = 3$ for the simulations performed in this thesis. The smallest physical dimension is 10 cm, the radius of the coil, so each Yee cell is $d\rho \times dz = 33.\overline{3} \times 33.\overline{3}$ mm. The resulting spatial discretization can be seen in Figure 21.

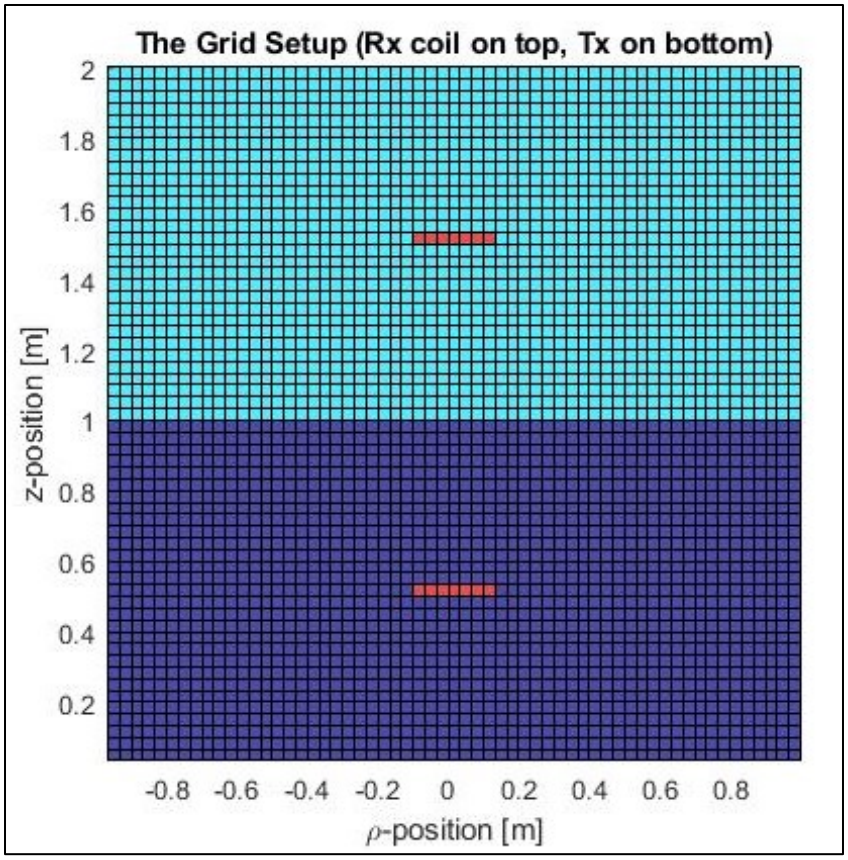

Figure 21: Grid resolution with $N_{dim} = 3$

3.2.4 Numerical Dispersion

Numerical dispersion occurs as a result of the discretization of the derivatives in Maxwell's equations and are inherent in the FDTD method but not present in real electromagnetic waves (Taflove and Hagness, 2005). As discussed in Chapter 2, in a physical system, dispersion describes the relationships between the wave number, speed of propagation, and frequency. In the FDTD algorithm, additional dispersive effects occur due to the fact that the distance from one corner of a Yee cell to the opposite corner, across the diagonal, is further than corners on the same side, so wave traveling from one cell to adjacent cells travels at different speeds due to the different distances travelled per timestep. The speed of the numerical EM waves can differ from c_o by an amount dependant upon the frequency, direction of propagation in the Yee lattice, and the grid discretization (Taflove and Hagness, 2005). Further, numerical instability can occur as a result of this numerical dispersion. From the numerical dispersion relation, an

expression can be derived, called the Courant stability criterion (see the next section), which places a limit on the relationship between the temporal and spatial resolutions. To this end, consider the FDTD update equations in free space.

$$H_x\big|_{t+\frac{\Delta t}{2}}^{i,j} = H_x\big|_{t-\frac{\Delta t}{2}}^{i,j} - \frac{\Delta t}{\Delta y \mu\big|^{i,j}}\left(E_z\big|_t^{i,j+1} - E_z\big|_t^{i,j}\right) \tag{3.15}$$

$$H_y\big|_{t+\frac{\Delta t}{2}}^{i,j} = H_y\big|_{t-\frac{\Delta t}{2}}^{i,j} + \frac{\Delta t}{\Delta x \mu\big|^{i,j}}\left(E_z\big|_t^{i+1,j} - E_z\big|_t^{i,j}\right) \tag{3.16}$$

$$E_z\big|_{t+\Delta t}^{i,j} = E_z\big|_t^{i,j} - \frac{\Delta t}{\varepsilon\big|^{i,j}}\left(\frac{H_y\big|_{t+\frac{\Delta t}{2}}^{i,j} - H_y\big|_{t+\frac{\Delta t}{2}}^{i-1,j}}{\Delta x} - \frac{H_x\big|_{t+\frac{\Delta t}{2}}^{i,j} - H_x\big|_{t+\frac{\Delta t}{2}}^{i,j-1}}{\Delta y}\right) \tag{3.17}$$

Using an approach similar to the one used in Chapter 2, assume the field components can be defined by plane waves of the form $E_z\big|_n^{I,J} = E_{z,0}e^{j(\omega n\Delta t - k_x I\Delta x - k_y I\Delta y)}$, $H_x\big|_n^{I,J} = H_{x,0}e^{j(\omega n\Delta t - k_x I\Delta x - k_y I\Delta y)}$, and $H_y\big|_n^{I,J} = H_{y,0}e^{j(\omega n\Delta t - k_x I\Delta x - k_y I\Delta y)}$. Following Taflove and Hagness, substituting these expressions into the FDTD form of Maxwell's equations results in

$$H_{x,0} = \frac{E_{z,0}\Delta \mathrm{t}}{\mu_0 \Delta y}\frac{\sin\left(\frac{k_y \Delta y}{2}\right)}{\sin\left(\frac{\omega \Delta \mathrm{t}}{2}\right)} \tag{3.18}$$

$$H_{y,0} = -\frac{E_{z,0}\Delta \mathrm{t}}{\mu_0 \Delta \mathrm{x}}\frac{\sin\left(\frac{k_x \Delta \mathrm{x}}{2}\right)}{\sin\left(\frac{\omega \Delta \mathrm{t}}{2}\right)} \tag{3.19}$$

$$E_{z,0}\sin\left(\frac{\omega \Delta \mathrm{t}}{2}\right) = \frac{\Delta t}{\varepsilon_0}\left[\frac{H_{x,0}}{\Delta y}\sin\left(\frac{k_y \Delta y}{2}\right) - \frac{H_{y,0}}{\Delta \mathrm{x}}\sin\left(\frac{k_x \Delta \mathrm{x}}{2}\right)\right] \tag{3.20}$$

After the first two equations are substituted into the third, we have the desired

$$\left[\frac{\sqrt{\mu_0\varepsilon_0}}{\Delta t}\sin\left(\frac{\omega\Delta t}{2}\right)\right]^2 = \left[\frac{1}{\Delta \mathrm{x}}\sin\left(\frac{k_x\Delta \mathrm{x}}{2}\right)\right]^2 + \left[\frac{1}{\Delta \mathrm{y}}\sin\left(\frac{k_y\Delta \mathrm{y}}{2}\right)\right]^2 \qquad 3.21$$

This is the general dispersion relation of the Yee algorithm for the TE case (it is assumed the plane of incidence is in the xy-plane). The implication of this is the introduction of numerical error which is inherent in the FDTD algorithm. In the limit where $\Delta \mathrm{x}$, $\Delta \mathrm{y}$, and $\Delta \mathrm{t}$ go to zero, the numerical dispersion relation reduces to the relation developed in Chapter 2 (i.e. $\mathrm{k}^2 = \omega^2\mu_0\varepsilon_0$). Decreasing the spatial and temporal resolution to zero is analogous to converting the discrete domain to a continuum, so we expect the real dispersion relation to have some connection to the numerical counterpart. In the next section, the numerical dispersion relation will be used to derive a condition for numerical stability. This is an extremely important concept in numerical computing.

3.2.5 The Courant Stability Criterion

The method used to find the Courant stability criterion is from the 2005 textbook called *Computational Electrodynamics: The Finite-Difference Time-Domain Method*, by Taflove and Hagness. This is considered the "bible" of the FDTD method. It begins by defining the frequency as a complex quantity $\tilde{\omega} = \omega_{real} + j\omega_{imag}$ and substituting into the equation describing the numerical dispersion developed in the last section.

$$\left[\frac{1}{c_0\Delta t}\sin\left(\frac{\tilde{\omega}\Delta t}{2}\right)\right]^2 = \left[\frac{1}{\Delta \mathrm{x}}\sin\left(\frac{k_x\Delta \mathrm{x}}{2}\right)\right]^2 + \left[\frac{1}{\Delta \mathrm{y}}\sin\left(\frac{k_y\Delta \mathrm{y}}{2}\right)\right]^2 \qquad 3.22$$

Equation 3.22 can then be solved for $\tilde{\omega}$ resulting in

$$\tilde{\omega} = \frac{2}{\Delta \mathrm{t}}\sin^{-1}(\xi) \qquad 3.23$$

$$\xi = c_0 \Delta t \sqrt{\left[\frac{1}{\Delta \mathrm{x}} \sin\left(\frac{k_x \Delta \mathrm{x}}{2}\right)\right]^2 + \left[\frac{1}{\Delta \mathrm{y}} \sin\left(\frac{k_y \Delta \mathrm{y}}{2}\right)\right]^2} \tag{3.24}$$

Where from the second equation, the term ξ is bounded such that

$$0 \leq \xi \leq c_0 \Delta t \sqrt{\left[\frac{1}{\Delta \mathrm{x}}\right]^2 + \left[\frac{1}{\Delta \mathrm{y}}\right]^2} \tag{3.25}$$

To avoid complex values of $\sin^{-1}(\xi)$ (and thus $\tilde{\omega}$ which give rise to numerical instability), we need to ensure $\xi < 1$. Therefore, we want $c_0 \Delta t \sqrt{\left[\frac{1}{\Delta \mathrm{x}}\right]^2 + \left[\frac{1}{\Delta \mathrm{y}}\right]^2}$ to be less than one. This results in the Courant stability criterion which places limits on the relationship between Δt and the spatial discretization defined by $\Delta \mathrm{x}$ and $\Delta \mathrm{y}$. The temporal resolution is calculated using the Courant stability criterion shown in Equation 3.26.

$$\Delta t < \frac{1}{c_0 \sqrt{\left(\frac{1}{\Delta x}\right)^2 + \left(\frac{1}{\Delta y}\right)^2}} \tag{3.26}$$

Throughout this work, the time step is calculated such that the Courant stability criterion is always satisfied. This has important implications on the FDTD simulation runtimes. When the frequency of operation is low, the long wavelengths are divided into very small sections of width Δt. Since this is determined by the grid resolution - which is the same for all test conditions - this can result in very long computational times.

3.2.6 Applying Boundary Conditions

The boundary conditions $\hat{n} \times \left(\vec{E}_1 - \vec{E}_2\right) = \vec{0}$ and $\hat{n} \cdot \left(\vec{B}_1 - \vec{B}_2\right) = 0$ were derived in Chapter 2 and now these expressions will be applied in the FDTD algorithm. A Perfectly Matched Layer (PML) was implemented in the FDTD simulator, but the details will be saved for later. The PML is not a substitute for boundary conditions; rather, the PML acts to absorb outgoing electromagnetic fields to simulate the fields traveling out to infinity. Boundary conditions must be defined in order for the mathematical problem to be considered well posed. The three main choices are Dirichlet, Neumann, and periodic boundary conditions. Dirichlet boundary conditions were used in the FDTD simulator and were defined at the edges of the computational space. This is equivalent to the walls acting as Perfect Electric Conductors (PEC), where the fields are assumed to decay rapidly to zero.

From $\hat{n} \times \left(\vec{E}_1 - \vec{E}_2\right) = \vec{0}$ and $\hat{n} \cdot \left(\vec{B}_1 - \vec{B}_2\right) = 0$, if we assume the interior domain is defined by the fields with the subscript one, $\vec{E}_1$ and $\vec{B}_1$, then applying the Dirichlet boundary conditions to region 2 results in $\vec{E}_2 = \vec{B}_2 = 0$ so we have

$$\hat{n} \times \vec{E}_1 = \vec{0} \text{ and } \hat{n} \cdot \vec{B}_1 = 0 \tag{3.27}$$

That is, $\vec{E}$ is parallel to $\hat{n}$ on the boundary which means its perpendicular component must be zero (i.e. $E_z = 0$ at the edge of the boundary). Similarly, $\vec{H}$ is perpendicular to $\hat{n}$ on the boundary which means its parallel component must be zero (that is, $H_x = 0$ along one wall, and $H_y = 0$ along the other). Using this logic, the boundary conditions were implemented in code as

$$\begin{aligned} E_z = H_x = 0 \text{ for } i = 1, N_x + 1 \\ E_z = H_y = 0 \text{ for } j = 1, N_y + 1 \end{aligned} \tag{3.28}$$

These are easily implemented in the FDTD algorithm by avoiding the edge nodes when applying the field update equations as shown in the pseudo-code snippet below.

```
for j = 1:Ny-1
   for i = 2:Nx
      % update equation for Hx
   end
end
% apply BC for Hx at j = Ny
for j = 2:Ny
   for i = 1:Nx-1
      % update equation for Hy
   end
end
% apply BC for Hy at i = Nx
for j = 2:Ny
   for i = 2:Nx
      % update equation for Ez
   end
end
```

3.3 Transmitting and Receiving Coils

The transmitting and receiving coils are both modelled using a series RLC circuit. The methods used for each circuit are nearly identical, except for one extra and very important step in the receiving coil. Each circuit will be discussed individually, here.

3.3.1 The Transmitter

The input signal, into the transmitting coil, can be selected as either a voltage or current. If the input signal is a current, the magnitude and frequency is defined, and the resulting magnetic fields are found directly, as will be discussed later. The magnetic field in then injected into the FDTD channel model. However, if the input signal is defined as a voltage, the coil current is found by numerically solving the differential equation describing the current in a series RLC circuit, as was discussed in Chapter 2. The second order equation is repeated here in Equation 3.29 for convenience.

$$\frac{d^2 I_L}{dt^2} + \frac{R}{L}\frac{dI_L}{dt} + \frac{1}{LC} I_L = \frac{1}{L}\frac{dV_{in}}{dt} \tag{3.29}$$

This equation can be solved analytically for simple cases of V_{in} (for example, if $V_{in} = \sin(2\pi f t)$); however, to allow the possibility of arbitrary input waveforms, this equation is solved numerically. One way to solve this equation on the computer is by approximating each term in the differential equation by a finite-difference representation. This is the basic approach taken for every differential equation encountered in this work. The derivation of these discrete approximations was discussed in Chapter 2. Applied to this equation, the following central difference is used to approximate the send order term.

$$\frac{d^2 I}{dt^2} \approx \frac{I_{n+1} - 2I_n + I_{n-1}}{(\Delta t)^2} \tag{3.30}$$

where it is implied $I = I_L$, for the purposes of simplifying the notation. The first order terms are also discretized using central differences:

$$\frac{d\psi}{dt} \approx \frac{\psi_{n+1} - \psi_{n-1}}{2\Delta t} \tag{3.31}$$

where ψ is I_L and V_{in}. Finally, assuming the initial conditions $I_1 = I_0 = 0$, for $n \geq 2$ Equation 3.32 is used to find the current in the transmitting coil when the input is a voltage signal.

$$I_{n+1} = AI_n + BI_{n-1} + C(V_{n+1} - V_{n-1}) \tag{3.32}$$

where the A, B, and C terms are constants defined by

$$A = \frac{\left(\frac{2}{(\Delta t)^2} - \frac{1}{LC}\right)}{\left(\frac{1}{(\Delta t)^2} + \frac{R}{2L\Delta t}\right)} \tag{3.33}$$

$$B = \frac{\left(\frac{R}{2L\Delta t} - \frac{1}{(\Delta t)^2}\right)}{\left(\frac{1}{(\Delta t)^2} + \frac{R}{2L\Delta t}\right)} \tag{3.34}$$

$$C = \frac{\frac{1}{2L\Delta t}}{\left(\frac{1}{(\Delta t)^2} + \frac{R}{2L\Delta t}\right)} \tag{3.35}$$

3.3.2 The Receiver

For the receiving RLC circuit model, the equations are identical, except that V_{in} is replaced with V_{emf}, which is the voltage included in the receiving coil. As discussed in Chapter 2, the induced voltage is found by taking the time derivative of the magnetic flux, Ψ, through the coil, as shown below.

$$V_{emf} = -N_{Rx}\frac{d\Psi}{dt} \tag{3.36}$$

As before, the first order term is discretized using central differences:

$$\frac{d\Psi}{dt} \approx -N_{Rx}\left(\frac{\Psi_{n+1} - \Psi_{n-1}}{2\Delta t}\right) \tag{3.37}$$

The flux term is found by sampling H_z at each grid point located along the line representing the receiving coil and averaging it, $H_{z,avg}$. The cross-sectional area of the receiving coil is assumed to be πr^2; thus, the flux is approximated using Equation 3.38.

$$\Psi \approx \pi r^2 \mu_o H_{z,avg} \tag{3.38}$$

3.4 Injecting the Source Signal

After the current in the transmitting coil has been determined, the next step is to determine the electromagnetic field source terms to inject into the FDTD computational domain for direct numerical evaluation of Maxwell's equations. In early versions of the

simulation tool (pre-V0.10.1), the conversion from current to electromagnetic fields was based on the point form of Ohm's law, as shown in Equation 3.39.

$$\vec{E} = \sigma\vec{J} \tag{3.39}$$

where the current density, $\vec{J}$, was calculated using either $\vec{J} = \frac{I}{\pi b^2}$, where b is the radius of the coil wire, or by using $\vec{J} = \frac{I}{\pi}\left(\frac{1}{b^2} - \frac{1}{\delta^2}\right)$, where $\delta = \sqrt{\frac{1}{2\pi f \mu\sigma}}$ is the skin depth of the currents flowing on the outer surface of the coil wire. This approach was determined to be incorrect. The main issue observed was the high sensitivity to the b term. Further, preliminary validation checks - which included finding the radiated magnetic field components for simple cases where analytical expressions exist - yielded poor and inconsistent results.

As an alternative method, the decions was made to use Ampere's law in its integral form as shown in Equation 3.40.

$$\oint_l \vec{H} \cdot d\vec{l} = I \tag{3.40}$$

Figure 22 shows a cross section of the coil wire with its center corresponding to the union of four Yee cells. Rather than injecting the electric field into the domain at the location of the wire, the integral form of Ampere's law was solved analytically and the H_ϕ and H_ρ components of $\vec{H}$ are determined at a distance of $\frac{\Delta\rho}{2}$ and used as source terms.

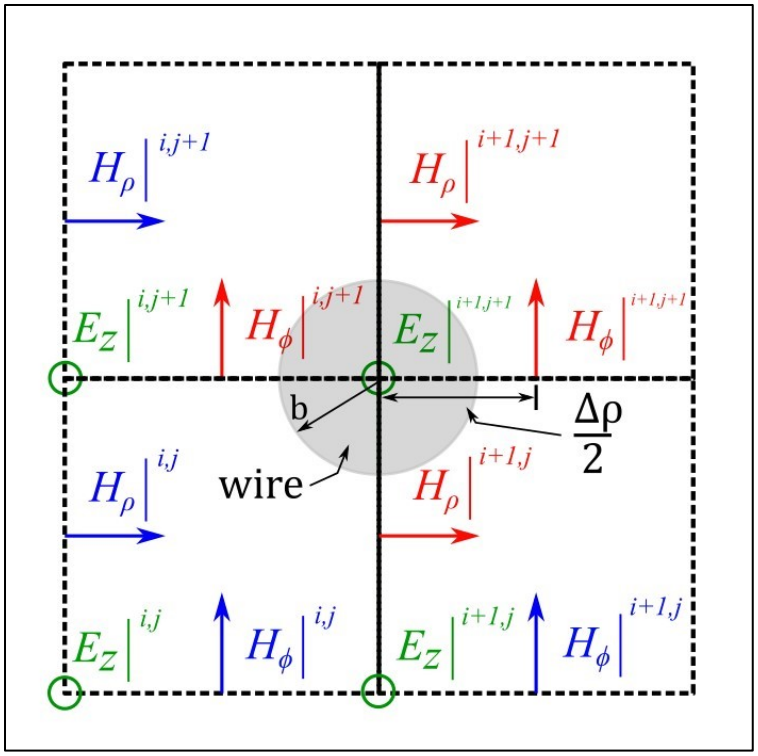

Figure 22: Geometry of source injection

In Figure 22, the H_ϕ terms are calculated using Equation 3.41 where, in this case, $\rho = \frac{\Delta\rho}{2}$ and $\rho \geq b$. This equation was derived in Chapter 2. The components of $\vec{H}$ are related such that $H_\phi|^{i+1,j+1} = -H_\phi|^{i,j+1}$ and $H_\rho|^{i+1,j+1} = -H_\rho|^{i+1,j}$ where we take advantage of cylindrical symmetry about the z-axis and $H_\phi = H_\rho$.

$$H_\phi = \frac{I}{2\pi\rho} \tag{3.41}$$

To account for the case where the transmitting coil is constructed using multiple turns of wire, the expressions for H_ϕ and H_ρ are scaled by the factor N_{Tx} representing the number of turns.

3.5 The Uniaxial Perfectly Matched Layer

The purpose of a Perfectly Matched Layer (PML) is to provide the ability to truncate the computational domain by simulating outgoing electromagnetic waves. The PML greatly

reduces the amount of reflection at the boundary by introducing a fictitious lossy material along the border of the domain. The material must be reflectionless to all incoming traveling waves regardless of their angle of incidence, so to accomplish this, the PML is defined as a uniaxial tensor: where the material's impedance depends on the direction the wave is traveling. This allows the simulation to run faster by decreasing the size of the domain. The derivations of the equations describing the Uniaxial PML (UPML) will be described here.

3.5.1 Matching Impedances

When two regions have mismatched impedances, an electromagnetic wave incident upon the boundary will be partially transmitted and partially reflected. The transmitted wave will undergo refraction according to Snell's law. Snell's law is shown in Equation 3.42.

$$\eta_1 \sin\theta_1 = \eta_2 \sin\theta_2 \tag{3.42}$$

The reflected wave will behave according to the Fresnel reflection coefficient equations. Fresnel equations are shown in Equations 3.43 and 3.44 and were derived in Chapter 2.

$$\Gamma_{TE} = \frac{\eta_2 \cos\theta_1 - \eta_1 \cos\theta_2}{\eta_2 \cos\theta_1 + \eta_1 \cos\theta_2} \tag{3.43}$$

$$\Gamma_{TM} = \frac{\eta_2 \cos\theta_2 - \eta_1 \cos\theta_1}{\eta_2 \cos\theta_2 + \eta_1 \cos\theta_1} \tag{3.44}$$

The goal is to eliminate reflections completely; therefore, we want $\Gamma_{TE} = \Gamma_{TM} = 0$, but inspection of the Fresnel equations shows that doing so results in the conditions

$$\eta_2 \cos\theta_{1,2} = \eta_1 \cos\theta_{2,1} \tag{3.45}$$

which are in addition to Snell's law. These conditions suggest that if the impedance of the UPML matches that of the interior domain, then both the refraction and reflections will be eliminated. To this end, the impedance is given by Equation 3.46.

$$\eta = \sqrt{\frac{\mu}{\varepsilon}} \tag{3.46}$$

For the case of $\eta = \eta_0$ (i.e. air), if we equate the permittivity and permeability of the medium and define them as anisotropic tensors, then the impedance of the UPML will be that of air. To this end, let

$$[\mu_r] = [\varepsilon_r] = \begin{bmatrix} a & 0 & 0 \\ 0 & b & 0 \\ 0 & 0 & c \end{bmatrix} \tag{3.47}$$

According to Rumph, with the permittivity and permeability defined like this, for a wave travelling in the z-direction, Snell's law can be rewritten as Equation 3.48

$$\sin\theta_1 = \sqrt{bc}\sin\theta_2 \tag{3.48}$$

and the Fresnel equations can be rewritten as Equations 3.49 and 3.50.

$$\Gamma_{TE} = \frac{\sqrt{a}\cos\theta_1 - \sqrt{b}\cos\theta_2}{\sqrt{a}\cos\theta_1 + \sqrt{b}\cos\theta_2} \tag{3.49}$$

$$\Gamma_{TM} = \frac{\sqrt{b}\cos\theta_2 - \sqrt{a}\cos\theta_1}{\sqrt{b}\cos\theta_2 + \sqrt{a}\cos\theta_1} \tag{3.50}$$

By choosing $\sqrt{bc} = 1$, Snell's law shows $\theta_1 = \theta_2$ so there is no refraction. With this, and by setting $\Gamma_{TE} = \Gamma_{TM} = 0$ which is the desired case, the Fresnel equations yield $a = b$. Therefore, for a wave travelling in the z-direction

$$[\mu_r] = [\varepsilon_r] = \begin{bmatrix} a & 0 & 0 \\ 0 & a & 0 \\ 0 & 0 & a^{-1} \end{bmatrix} \tag{3.51}$$

Next, these results will be used to derive the uniaxial tensor, $[S]$, defining the UPML.

3.5.2 Final UPML Equation

The idea here is to put the formulation for impedance matching on the parameter $[S]$ rather than on the permittivity and permeability. Therefore, for a wave travelling in the z-direction, let $[\mu_r] = \mu[S_z]$ and $[\varepsilon_r] = \varepsilon[S_z]$ and we define $[S_z]$ such that

$$[S_z] = \begin{bmatrix} s_z & 0 & 0 \\ 0 & s_z & 0 \\ 0 & 0 & {s_z}^{-1} \end{bmatrix} \tag{3.52}$$

Using similar reasoning, expressions for waves travelling in the x- and y-directions (represented using $[S_{x,y}]$) can be obtained

$$[S_x] = \begin{bmatrix} {s_x}^{-1} & 0 & 0 \\ 0 & s_x & 0 \\ 0 & 0 & s_x \end{bmatrix} \tag{3.53}$$

$$[S_y] = \begin{bmatrix} s_y & 0 & 0 \\ 0 & {s_y}^{-1} & 0 \\ 0 & 0 & s_y \end{bmatrix} \tag{3.54}$$

Finally, we define $[S] = [S_x][S_y][S_z]$ in Equation 3.55

$$[S] = \begin{bmatrix} \frac{s_y s_z}{s_x} & 0 & 0 \\ 0 & \frac{s_x s_z}{s_y} & 0 \\ 0 & 0 & \frac{s_x s_y}{s_z} \end{bmatrix} \tag{3.55}$$

which is the form of the uniaxial tensor defining the UPML used in this FDTD simulator. The idea is to introduce loss into the UPML material similar to how a complex relative permittivity accomplishes this: $\tilde{\varepsilon}_r = \varepsilon_r + \frac{\sigma}{j\omega\varepsilon_0}$. Using this, we define the UPML parameters as shown in Equation 3.56.

$$s_i = 1 + \frac{\sigma_i}{j\omega\varepsilon} \tag{3.56}$$

for $i = x, y,$ and z. The next section will show how $[S]$ is incorporated into the update equations for the FDTD algorithm for the case of a Cartesian coordinate system.

3.6 FDTD Update Equations with a UPML

With the UPML fully defined, this section will derive the resulting update equations for the FDTD algorithm in continuous and discrete form. The development of the update equations requires long and messy looking formulae, so a summary will be provided at the end of this section. The formulation in Cartesian coordinates will be presented first, and then the necessary modification for implementation in cylindrical coordinates will follow. The FDTD simulations are performed in cylindrical coordinates.

3.6.1 Update Equations: Continuous Form

The UPML tensor is introduced in Maxwell's equations according to Equations 3.57 and 3.58.

$$\nabla \times \vec{E} = -j\omega\mu[S]\vec{H} \tag{3.57}$$

$$\nabla \times \vec{H} = \sigma\vec{E} + j\omega\varepsilon[S]\vec{E} \tag{3.58}$$

Further, we rewrite the UPML tensor as shown in Equation 3.59.

$$[S] = \begin{bmatrix} s_{xx} & 0 & 0 \\ 0 & s_{yy} & 0 \\ 0 & 0 & s_{zz} \end{bmatrix} \tag{3.59}$$

where, for ease of notation, we will use the following expressions for s_{ii}, $i = x, y,$ and z.

$$s_{xx} = \frac{s_y s_z}{s_x} \tag{3.60}$$

$$s_{yy} = \frac{s_x s_z}{s_y} \tag{3.61}$$

$$s_{zz} = \frac{s_x s_y}{s_z} \tag{3.62}$$

It was shown earlier that the TM and TE modes are decoupled in 2D, and since we will only be focusing on the TE mode, the associated update equations are shown in Equations 3.63 to 3.65.

$$\frac{1}{\mu}\frac{\partial E_z}{\partial y} = -j\omega s_{xx} H_x \tag{3.63}$$

$$\frac{1}{\mu}\frac{\partial E_z}{\partial x} = j\omega s_{yy} H_y \tag{3.64}$$

$$\frac{\partial H_y}{\partial x} - \frac{\partial H_x}{\partial y} = \sigma E_z + j\omega\varepsilon s_{zz} E_z \tag{3.65}$$

Using the definitions for s_{ii} and s_i, where $i = x, y,$ or z, the update equations become

$$\frac{1}{\mu}\frac{\partial E_z}{\partial y} = -j\omega\left(1 + \frac{\sigma_x}{j\omega\varepsilon}\right)^{-1}\left(1 + \frac{\sigma_y}{j\omega\varepsilon}\right)\left(1 + \frac{\sigma_z}{j\omega\varepsilon}\right) H_x \tag{3.66}$$

$$\frac{1}{\mu}\frac{\partial E_z}{\partial x} = j\omega\left(1+\frac{\sigma_x}{j\omega\varepsilon}\right)\left(1+\frac{\sigma_y}{j\omega\varepsilon}\right)^{-1}\left(1+\frac{\sigma_z}{j\omega\varepsilon}\right)H_y \tag{3.67}$$

$$\frac{\partial H_y}{\partial x} - \frac{\partial H_x}{\partial y} = \sigma E_z + j\omega\varepsilon\left(1+\frac{\sigma_x}{j\omega\varepsilon}\right)\left(1+\frac{\sigma_y}{j\omega\varepsilon}\right)\left(1+\frac{\sigma_z}{j\omega\varepsilon}\right)^{-1}E_z \tag{3.68}$$

which can be rewritten as

$$\frac{1}{\mu}\frac{\partial E_z}{\partial y}\left(1+\frac{\sigma_x}{j\omega\varepsilon}\right) = -\left(j\omega + \frac{\sigma_y+\sigma_z}{\varepsilon} + \frac{\sigma_y\sigma_z}{j\omega\varepsilon^2}\right)H_x \tag{3.69}$$

$$\frac{1}{\mu}\frac{\partial E_z}{\partial x}\left(1+\frac{\sigma_y}{j\omega\varepsilon}\right) = \left(j\omega + \frac{\sigma_x+\sigma_z}{\varepsilon} + \frac{\sigma_x\sigma_z}{j\omega\varepsilon^2}\right)H_y \tag{3.70}$$

$$\left(\frac{\partial H_y}{\partial x} - \frac{\partial H_x}{\partial y}\right)\left(1+\frac{\sigma_z}{j\omega\varepsilon}\right) = \sigma\left(1+\frac{\sigma_z}{j\omega\varepsilon}\right)E_z + \left(j\omega + \frac{\sigma_x+\sigma_y}{\varepsilon} + \frac{\sigma_x\sigma_y}{j\omega\varepsilon^2}\right)\varepsilon E_z \tag{3.71}$$

Next, the equations are converted back into the time domain using the inverse Fourier transform operations $j\omega \rightarrow \frac{\partial}{\partial t}$ and $\frac{1}{j\omega} \rightarrow \int_{-\infty}^{t} d\tau$

$$\frac{1}{\mu}\frac{\partial E_z}{\partial y} + \frac{\sigma_x}{\mu\varepsilon}\int_{-\infty}^{t}\frac{\partial E_z}{\partial y}d\tau = -\frac{\partial H_x}{\partial t} - \frac{\sigma_y+\sigma_z}{\varepsilon}H_x - \frac{\sigma_y\sigma_z}{\varepsilon^2}\int_{-\infty}^{t}H_x d\tau \tag{3.72}$$

$$\frac{1}{\mu}\frac{\partial E_z}{\partial x} + \frac{\sigma_y}{\mu\varepsilon}\int_{-\infty}^{t}\frac{\partial E_z}{\partial x}d\tau = \frac{\partial H_y}{\partial t} + \frac{\sigma_x+\sigma_z}{\varepsilon}H_y + \frac{\sigma_x\sigma_z}{\varepsilon^2}\int_{-\infty}^{t}H_y d\tau \tag{3.73}$$

$$\begin{aligned}\frac{\partial H_y}{\partial x} - \frac{\partial H_x}{\partial y} + \frac{\sigma_z}{\varepsilon}\int_{-\infty}^{t}\left(\frac{\partial H_y}{\partial x} - \frac{\partial H_x}{\partial y}\right)d\tau = \cdots \\ \cdots = (\sigma+\sigma_x+\sigma_y)E_z + \varepsilon\frac{\partial E_z}{\partial t} + \left(\frac{\sigma_z}{\varepsilon}+\frac{\sigma_x\sigma_y}{\varepsilon^2}\right)\int_{-\infty}^{t}E_z d\tau\end{aligned} \tag{3.74}$$

Equations 3.72 through 3.74 are the continuous form of the update equations for the FDTD algorithm which include the effects of a uniaxial tensor describing the UPML. The next section will show the discrete form of these equations which were implemented in the FDTD simulation.

3.6.2 Update Equations: Discrete Form

In order to discretize Equations 3.72 through 3.74 for implementation on the computer, each term must be approximated using numerical approximations. The derivatives were approximated using finite differences, and the integrals were done so using numerical integration. Earlier in this chapter, the finite difference form of the derivatives was shown. Here, the numerical approximation of the other terms will be presented.

As an example, take the integral term involving H_x. Because of the leap-frog method being employed, careful consideration must be given to when each term is being evaluated (that is, if either at t or $t + \frac{\Delta t}{2}$). Equation 3.72 is for $H_x|_{t+\frac{\Delta t}{2}}^{i,j}$, however, H_x at the next half-time step is being evaluated based on terms at time t (the curl of E_z). Therefore, the integrals must go to t and the H_x term must be approximated at time t using an average since it only exists at $t \pm \frac{\Delta t}{2}$. The average value of H_x at t was taken to be

$$H_x|_t^{i,j} \approx \frac{H_x|_{t+\frac{\Delta t}{2}}^{i,j} + H_x|_{t-\frac{\Delta t}{2}}^{i,j}}{2} \tag{3.75}$$

The numerical integration relies on taking the average value of H_x like this because the integral is supposed to go to t. Ideally, with sufficiently small Δt, the integral of H_x would be approximated using

$$\int_{-\infty}^{t} H_x d\tau \approx \sum_{n=\frac{\Delta t}{2}}^{t} H_x|_n^{i,j}\, \Delta t \tag{3.76}$$

However, since $H_x|_t^{i,j}$ does not exist (i.e. the last term in the summation), it is pulled out of the integral and approximated over half of a time step, and the result is shown in Equation 3.77.

$$\int_{-\infty}^{t} H_x d\tau \approx \left(\frac{H_x|_{t+\frac{\Delta t}{2}}^{i,j} + H_x|_{t-\frac{\Delta t}{2}}^{i,j}}{2} \right) \frac{\Delta t}{2} + \sum_{n=\frac{\Delta t}{2}}^{t-\frac{\Delta t}{2}} H_x|_n^{i,j} \, \Delta t \tag{3.77}$$

Additionally, for ease of notation, and using the nomenclature used by Rumph, we define the term $C_x^E|_t^{i,j}$ to mean *the x-component of the curl of E*, the term $C_y^E\big|_t^{i,j}$ to mean *the y-component of the curl of E*, and the term $C_z^H|_t^{i,j}$ to mean *the z-component of the curl of H*. So again, focusing on discretizing Equation 3.72 only for now,

$$C_x^E|_t^{i,j} \equiv \frac{\partial E_z}{\partial y} \approx \frac{E_z|_t^{i,j+1} - E_z|_t^{i,j}}{\Delta y} \tag{3.78}$$

Putting all of this together, Equation 3.72 is discretized according to Equation 3.79.

$$\begin{aligned} \frac{1}{\mu|^{i,j}} C_x^E|_t^{i,j} + \frac{\sigma_x|^{i,j} \Delta t}{\mu|^{i,j} \varepsilon|^{i,j}} \sum_{n=\frac{\Delta t}{2}}^{t} C_x^E|_n^{i,j} = & -\left(\frac{H_x|_{t+\frac{\Delta t}{2}}^{i,j} - H_x|_{t-\frac{\Delta t}{2}}^{i,j}}{\Delta t} \right) - \cdots \\ \cdots - \left(\frac{\sigma_y\big|^{i,j} + \sigma_z|^{i,j}}{\varepsilon|^{i,j}} \right) & \left(\frac{H_x|_{t+\frac{\Delta t}{2}}^{i,j} + H_x|_{t-\frac{\Delta t}{2}}^{i,j}}{2} \right) - \cdots \\ \cdots - \left(\frac{\sigma_y\big|^{i,j} \sigma_z|^{i,j} \Delta t}{(\varepsilon|^{i,j})^2} \right) & \left(\left(\frac{H_x|_{t+\frac{\Delta t}{2}}^{i,j} + H_x|_{t-\frac{\Delta t}{2}}^{i,j}}{4} \right) + \sum_{n=\frac{\Delta t}{2}}^{t-\frac{\Delta t}{2}} H_x|_n^{i,j} \right) \end{aligned} \tag{3.79}$$

Finally, after rearranging and solving for $H_x|^{i,j}_{t+\frac{\Delta t}{2}}$, the resulting discretized update equation for Equation 3.72 is

$$H_x|^{i,j}_{t+\frac{\Delta t}{2}} = (A)H_x|^{i,j}_{t-\frac{\Delta t}{2}} + (B)C_x^E|^{i,j}_t + (C)\sum_{n=\frac{\Delta t}{2}}^{t} C_x^E|^{i,j}_n + (D)\sum_{n=\frac{\Delta t}{2}}^{t-\frac{\Delta t}{2}} H_x|^{i,j}_n \tag{3.80}$$

where the constant terms $A, B, C,$ and D are defined as

$$A = \frac{\frac{1}{\Delta t} - \frac{\sigma_y|^{i,j} + \sigma_z|^{i,j}}{2\varepsilon|^{i,j}} - \frac{\sigma_y|^{i,j}\sigma_z|^{i,j}\Delta t}{4(\varepsilon|^{i,j})^2}}{\frac{1}{\Delta t} + \frac{\sigma_y|^{i,j} + \sigma_z|^{i,j}}{2\varepsilon|^{i,j}} + \frac{\sigma_y|^{i,j}\sigma_z|^{i,j}\Delta t}{4(\varepsilon|^{i,j})^2}} \tag{3.81}$$

$$B = \frac{-\frac{1}{\mu|^{i,j}}}{\frac{1}{\Delta t} + \frac{\sigma_y|^{i,j} + \sigma_z|^{i,j}}{2\varepsilon|^{i,j}} + \frac{\sigma_y|^{i,j}\sigma_z|^{i,j}\Delta t}{4(\varepsilon|^{i,j})^2}} \tag{3.82}$$

$$C = \frac{-\frac{\sigma_x|^{i,j}\Delta t}{\mu|^{i,j}\varepsilon|^{i,j}}}{\frac{1}{\Delta t} + \frac{\sigma_y|^{i,j} + \sigma_z|^{i,j}}{2\varepsilon|^{i,j}} + \frac{\sigma_y|^{i,j}\sigma_z|^{i,j}\Delta t}{4(\varepsilon|^{i,j})^2}} \tag{3.83}$$

$$D = \frac{-\frac{\sigma_y|^{i,j}\sigma_z|^{i,j}\Delta t}{(\varepsilon|^{i,j})^2}}{\frac{1}{\Delta t} + \frac{\sigma_y|^{i,j} + \sigma_z|^{i,j}}{2\varepsilon|^{i,j}} + \frac{\sigma_y|^{i,j}\sigma_z|^{i,j}\Delta t}{4(\varepsilon|^{i,j})^2}} \tag{3.84}$$

Finally, the terms representing the conductivity of the UPML are tapered from the start of the PML interior to the domain outwards to the boundary.

$$\sigma_x|^{i,j} = \left(\frac{\varepsilon|^{i,j}}{2\Delta t}\right)\left(\frac{i'}{l}\right)^3 \tag{3.85}$$

$$\sigma_y\big|^{i,j} = \left(\frac{\varepsilon|^{i,j}}{2\Delta t}\right)\left(\frac{j'}{l}\right)^3 \tag{3.86}$$

$$\sigma_z|^{i,j} = \left(\frac{\varepsilon|^{i,j}}{2\Delta t}\right)\left(\frac{1}{l}\right)^3 \tag{3.87}$$

where i' and j' are not to be confused with i and j (which represent grid coordinates); rather i' and j' are inside the UPML only, such that $1 \leq i' \leq l$ and $1 \leq j' \leq l$, where l is the length of the PML in number of grids. Note that $\sigma_z|^{i,j}$ is set to a constant since the simulator is in 2D and there are no waves incident from the z-direction. Equations 3.80 through 3.84 were implemented in the FDTD simulator developed for this thesis. The next section will provide a summary of all three update equations for $H_x|^{i,j}_{t+\frac{\Delta t}{2}}$, $H_y\big|^{i,j}_{t+\frac{\Delta t}{2}}$, and $E_z|^{i,j}_t$.

3.6.3 Summary of Update Equations

The update equation for H_x is shown in Equation 3.88. This represents Equation 3.72.

$$H_x|^{i,j}_{t+\frac{\Delta t}{2}} = (A)H_x|^{i,j}_{t-\frac{\Delta t}{2}} + (B)C_x^E|^{i,j}_t + (C)\sum_{n=\frac{\Delta t}{2}}^{t} C_x^E|^{i,j}_n + (D)\sum_{n=\frac{\Delta t}{2}}^{t-\frac{\Delta t}{2}} H_x|^{i,j}_n \tag{3.88}$$

where the constant terms $A, B, C,$ and D are defined as

$$A = \frac{\frac{1}{\Delta t} - \frac{\sigma_y\big|^{i,j} + \sigma_z|^{i,j}}{2\varepsilon|^{i,j}} - \frac{\sigma_y\big|^{i,j}\sigma_z|^{i,j}\Delta t}{4(\varepsilon|^{i,j})^2}}{\frac{1}{\Delta t} + \frac{\sigma_y\big|^{i,j} + \sigma_z|^{i,j}}{2\varepsilon|^{i,j}} + \frac{\sigma_y\big|^{i,j}\sigma_z|^{i,j}\Delta t}{4(\varepsilon|^{i,j})^2}} \tag{3.89}$$

$$B = \frac{-\frac{1}{\mu|^{i,j}}}{\frac{1}{\Delta t} + \frac{\sigma_y\big|^{i,j} + \sigma_z|^{i,j}}{2\varepsilon|^{i,j}} + \frac{\sigma_y\big|^{i,j}\sigma_z|^{i,j}\Delta t}{4(\varepsilon|^{i,j})^2}} \tag{3.90}$$

$$C = \frac{-\frac{\sigma_x|^{i,j}\Delta t}{\mu|^{i,j}\varepsilon|^{i,j}}}{\frac{1}{\Delta t} + \frac{\sigma_y\big|^{i,j} + \sigma_z|^{i,j}}{2\varepsilon|^{i,j}} + \frac{\sigma_y\big|^{i,j}\sigma_z|^{i,j}\Delta t}{4(\varepsilon|^{i,j})^2}} \tag{3.91}$$

$$D = \frac{-\frac{\sigma_y\big|^{i,j}\sigma_z|^{i,j}\Delta t}{(\varepsilon|^{i,j})^2}}{\frac{1}{\Delta t} + \frac{\sigma_y\big|^{i,j} + \sigma_z|^{i,j}}{2\varepsilon|^{i,j}} + \frac{\sigma_y\big|^{i,j}\sigma_z|^{i,j}\Delta t}{4(\varepsilon|^{i,j})^2}} \tag{3.92}$$

The update equation for H_y is shown in Equation 3.93. This represents Equation 3.73.

$$H_y\big|^{i,j}_{t+\frac{\Delta t}{2}} = (E)H_y\big|^{i,j}_{t-\frac{\Delta t}{2}} + (F)C_y^E\big|^{i,j}_{t} + (G)\sum_{n=\frac{\Delta t}{2}}^{t} C_y^E\big|^{i,j}_{n} + (H)\sum_{n=\frac{\Delta t}{2}}^{t-\frac{\Delta t}{2}} H_y\big|^{i,j}_{n} \tag{3.93}$$

where the constant terms E, F, G, and H are defined as

$$E = \frac{\frac{1}{\Delta t} - \frac{\sigma_x|^{i,j} + \sigma_z|^{i,j}}{2\varepsilon|^{i,j}} - \frac{\sigma_x|^{i,j}\sigma_z|^{i,j}\Delta t}{4(\varepsilon|^{i,j})^2}}{\frac{1}{\Delta t} + \frac{\sigma_x|^{i,j} + \sigma_z|^{i,j}}{2\varepsilon|^{i,j}} + \frac{\sigma_x|^{i,j}\sigma_z|^{i,j}\Delta t}{4(\varepsilon|^{i,j})^2}} \tag{3.94}$$

$$F = \frac{\frac{1}{\mu|^{i,j}}}{\frac{1}{\Delta t} + \frac{\sigma_x|^{i,j} + \sigma_z|^{i,j}}{2\varepsilon|^{i,j}} + \frac{\sigma_x|^{i,j}\sigma_z|^{i,j}\Delta t}{4(\varepsilon|^{i,j})^2}} \tag{3.95}$$

$$G = \frac{\frac{\sigma_y\big|^{i,j}\Delta t}{\mu|^{i,j}\varepsilon|^{i,j}}}{\frac{1}{\Delta t} + \frac{\sigma_x|^{i,j} + \sigma_z|^{i,j}}{2\varepsilon|^{i,j}} + \frac{\sigma_x|^{i,j}\sigma_z|^{i,j}\Delta t}{4(\varepsilon|^{i,j})^2}} \tag{3.96}$$

$$H = \frac{\frac{\sigma_x|^{i,j}\sigma_z|^{i,j}\Delta t}{(\varepsilon|^{i,j})^2}}{\frac{1}{\Delta t} + \frac{\sigma_x|^{i,j} + \sigma_z|^{i,j}}{2\varepsilon|^{i,j}} + \frac{\sigma_x|^{i,j}\sigma_z|^{i,j}\Delta t}{4(\varepsilon|^{i,j})^2}} \tag{3.97}$$

Finally, the update equation for E_z is shown in Equation 3.98. This represents Equation 3.74.

$$E_z|_{t+\Delta t}^{i,j} = (I)E_z|_t^{i,j} + (J)C_z^H|_t^{i,j} + (K)\sum_{n=\frac{\Delta t}{2}}^{t} C_z^H|_n^{i,j} + (L)\sum_{n=\frac{\Delta t}{2}}^{t} E_z|_n^{i,j} \tag{3.98}$$

where the constant terms I, J, K and L are defined as

$$I = \frac{\frac{1}{\Delta t} - \frac{\sigma_x|^{i,j} + \sigma_y\big|^{i,j} + \sigma|^{i,j}}{2\varepsilon|^{i,j}} - \frac{\sigma_x|^{i,j}\sigma_y\big|^{i,j}\Delta t}{4(\varepsilon|^{i,j})^2}}{\frac{1}{\Delta t} + \frac{\sigma_x|^{i,j} + \sigma_y\big|^{i,j} + \sigma|^{i,j}}{2\varepsilon|^{i,j}} + \frac{\sigma_x|^{i,j}\sigma_y\big|^{i,j}\Delta t}{4(\varepsilon|^{i,j})^2}} \tag{3.99}$$

$$J = \frac{1}{\frac{1}{\Delta t} + \frac{\sigma_x|^{i,j} + \sigma_y\big|^{i,j} + \sigma|^{i,j}}{2\varepsilon|^{i,j}} + \frac{\sigma_x|^{i,j}\sigma_y\big|^{i,j}\Delta t}{4(\varepsilon|^{i,j})^2}} \tag{3.100}$$

$$K = \frac{-\frac{\sigma_z|^{i,j}\Delta t}{\varepsilon|^{i,j}}}{\frac{1}{\Delta t} + \frac{\sigma_x|^{i,j} + \sigma_y\big|^{i,j} + \sigma|^{i,j}}{2\varepsilon|^{i,j}} + \frac{\sigma_x|^{i,j}\sigma_y\big|^{i,j}\Delta t}{4(\varepsilon|^{i,j})^2}} \tag{3.101}$$

$$L = \frac{-\frac{\sigma_x|^{i,j}\sigma_y\big|^{i,j}\Delta t}{(\varepsilon|^{i,j})^2}}{\frac{1}{\Delta t} + \frac{\sigma_x|^{i,j} + \sigma_y\big|^{i,j} + \sigma|^{i,j}}{2\varepsilon|^{i,j}} + \frac{\sigma_x|^{i,j}\sigma_y\big|^{i,j}\Delta t}{4(\varepsilon|^{i,j})^2}} \tag{3.102}$$

3.7 FDTD in Cylindrical Coordinates

The formulation of the FDTD update equations in the preceding section are valid for a 2D geometry in Cartesian coordinates. A 2D formulation like this assumes $\frac{\partial \psi}{\partial z} = 0$ which states there is no variation of ψ in the z-direction. This type of assumption is justified if the problem of interest has this type of symmetry (for example, a long straight wire). However, the problem of modelling a coil does not contain this type of symmetry; rather, this problem possesses cylindrical symmetry. This section will show how the FDTD update equations were modified and implemented in cylindrical coordinates.

3.7.1 Cylindrical Symmetry

Since a coil of wire exhibits cylindrical symmetry about the z-axis, if the z-axis is placed in the center of the transmitting coil, then the problem of solving for the fields being radiated by the transmitting coil will also have cylindrical symmetry. The benefit of taking this approach is the reduction in computational effort since only half of the domain needs to be included in the computational space (since the rest of the space is obtained by simply revolving the fields around the z-axis).

Figure 23 shows a sketch of the portion of the ρ, z-plane required by the FDTD algorithm in cylindrical coordinates. The circles above and below the water's surface are cross-sections of the receiving and transmitting coils, respectively, represented here as a single turn of wire. Following the computation of the electromagnetic fields in this half of the ρ, z-plane, at each time step, the fields obtained in this portion of the domain are simply copied to the hidden half of the ρ, z-plane for inclusion in the 2D algorithm. Rather than iterating through $N_\rho \times N_z$ Yee cells, the problem is reduced to $\frac{N_\rho}{2} \times \frac{N_z}{2}$.

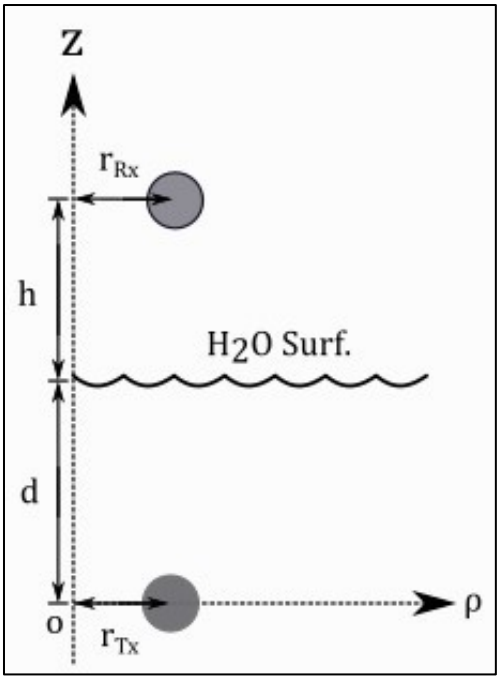

Figure 23: The 2D problem space in cylindrical coordinates

Note: with this implementation of cylindrical coordinates, since the cylindrical symmetry is dependant upon the horizontal orientation of the transmitting coil, the transmitting coil must be horizontal. This was not the case for earlier versions of the simulator prior to the application of cylindrical coordinates.

3.7.2 Maxwell's Equations in Cylindrical Coordinates

To take advantage of the inherent cylindrical symmetry, Maxwell's equations must be written in cylindrical coordinates. The curl operator for cylindrical coordinates is shown in Equation 3.103.

$$\nabla \times \vec{\psi} = \left(\frac{1}{\rho}\frac{\partial \psi_z}{\partial \varphi} - \frac{\partial \psi_\varphi}{\partial z}\right)\hat{\rho} + \left(\frac{\partial \psi_\rho}{\partial z} - \frac{\partial \psi_z}{\partial \rho}\right)\hat{\varphi} + \frac{1}{\rho}\left(\frac{\partial(\rho\psi_\varphi)}{\partial \rho} - \frac{\partial \psi_\rho}{\partial \varphi}\right)\hat{z} \qquad 3.103$$

Cylindrical symmetry about the z-axis is obtained by setting $\frac{\partial}{\partial \varphi} = 0$. Maxwell's equations become

$$\frac{\partial E_\varphi}{\partial z} = s_{\rho\rho}\mu\frac{\partial H_\rho}{\partial t} \tag{3.104}$$

$$\frac{1}{\rho}\frac{\partial\left(\rho E_\varphi\right)}{\partial \rho} = -s_{zz}\mu\frac{\partial H_z}{\partial t} \tag{3.105}$$

$$\frac{\partial H_\rho}{\partial z} - \frac{\partial H_z}{\partial \rho} = \sigma E_\varphi + \varepsilon s_{\varphi\varphi}\frac{\partial E_\varphi}{\partial t} \tag{3.106}$$

Equations 3.104 and 3.106 can be approximated using finite differences, as before, in a straight forward manner; however, Equation 3.105 is converted into its nonconservative form using the product rule of differentiation as shown in Equation 3.107.

$$\frac{1}{\rho}\frac{\partial\left(\rho E_\varphi\right)}{\partial \rho} = \frac{1}{\rho}E_\varphi + \frac{\partial E_\varphi}{\partial \rho} = -s_{zz}\mu\frac{\partial H_z}{\partial t} \tag{3.107}$$

The terms s_{jj}, $j = \rho, \varphi$, and z, are the cylindrical counterparts of s_{ii}, $i = x, y$, and z, as described in the preceding sections.

3.7.3 Update Equations in Cylindrical Coordinates

The update equation for H_ρ is shown in Equation 3.108. This represents Equation 3.104.

$$H_\rho\Big|_{t+\frac{\Delta t}{2}}^{i,j} = (A')H_\rho\Big|_{t-\frac{\Delta t}{2}}^{i,j} + (B')C_\rho^E\Big|_t^{i,j} + (C')\sum_{n=\frac{\Delta t}{2}}^{t} C_\rho^E\Big|_n^{i,j} + (D')\sum_{n=\frac{\Delta t}{2}}^{t-\frac{\Delta t}{2}} H_\rho\Big|_n^{i,j} \tag{3.108}$$

where the constant terms A', B', C', and D' are defined as

$$A' = \frac{\frac{1}{\Delta t} - \frac{\sigma_\varphi\big|^{i,j} + \sigma_z|^{i,j}}{2\varepsilon|^{i,j}} - \frac{\sigma_\varphi\big|^{i,j}\sigma_z|^{i,j}\Delta t}{4(\varepsilon|^{i,j})^2}}{\frac{1}{\Delta t} + \frac{\sigma_\varphi\big|^{i,j} + \sigma_z|^{i,j}}{2\varepsilon|^{i,j}} + \frac{\sigma_\varphi\big|^{i,j}\sigma_z|^{i,j}\Delta t}{4(\varepsilon|^{i,j})^2}} \tag{3.109}$$

$$B' = \frac{-\frac{1}{\mu|^{i,j}}}{\frac{1}{\Delta t} + \frac{\sigma_\varphi\big|^{i,j} + \sigma_z|^{i,j}}{2\varepsilon|^{i,j}} + \frac{\sigma_\varphi\big|^{i,j}\sigma_z|^{i,j}\Delta t}{4(\varepsilon|^{i,j})^2}} \tag{3.110}$$

$$C' = \frac{-\frac{\sigma_\rho\big|^{i,j}\Delta t}{\mu|^{i,j}\varepsilon|^{i,j}}}{\frac{1}{\Delta t} + \frac{\sigma_\varphi\big|^{i,j} + \sigma_z|^{i,j}}{2\varepsilon|^{i,j}} + \frac{\sigma_\varphi\big|^{i,j}\sigma_z|^{i,j}\Delta t}{4(\varepsilon|^{i,j})^2}} \tag{3.111}$$

$$D' = \frac{-\frac{\sigma_\varphi\big|^{i,j}\sigma_z|^{i,j}\Delta t}{(\varepsilon|^{i,j})^2}}{\frac{1}{\Delta t} + \frac{\sigma_\varphi\big|^{i,j} + \sigma_z|^{i,j}}{2\varepsilon|^{i,j}} + \frac{\sigma_\varphi\big|^{i,j}\sigma_z|^{i,j}\Delta t}{4(\varepsilon|^{i,j})^2}} \tag{3.112}$$

The update equation for H_z is shown in Equation 3.113, and it includes the effects of the modified curl term, C_z^E. This represents Equation 3.107.

$$H_z|^{i,j}_{t+\frac{\Delta t}{2}} = (E')H_z|^{i,j}_{t-\frac{\Delta t}{2}} + (F')C_z^E|^{i,j}_t + (G')\sum_{n=\frac{\Delta t}{2}}^{t} C_z^E|^{i,j}_n + (H')\sum_{n=\frac{\Delta t}{2}}^{t-\frac{\Delta t}{2}} H_z|^{i,j}_n \tag{3.113}$$

where the constant terms E', F', G', and H' are defined as

$$E' = \frac{\frac{1}{\Delta t} - \frac{\sigma_\rho\big|^{i,j} + \sigma_z|^{i,j}}{2\varepsilon|^{i,j}} - \frac{\sigma_\rho\big|^{i,j}\sigma_z|^{i,j}\Delta t}{4(\varepsilon|^{i,j})^2}}{\frac{1}{\Delta t} + \frac{\sigma_\rho\big|^{i,j} + \sigma_\varphi\big|^{i,j}}{2\varepsilon|^{i,j}} + \frac{\sigma_\rho\big|^{i,j}\sigma_\varphi\big|^{i,j}\Delta t}{4(\varepsilon|^{i,j})^2}} \tag{3.114}$$

$$F' = \frac{\frac{1}{\mu|^{i,j}}}{\frac{1}{\Delta t} + \frac{\sigma_\rho\big|^{i,j} + \sigma_\varphi\big|^{i,j}}{2\varepsilon|^{i,j}} + \frac{\sigma_\rho\big|^{i,j}\sigma_\varphi\big|^{i,j}\Delta t}{4(\varepsilon|^{i,j})^2}} \tag{3.115}$$

$$G' = \frac{\frac{\sigma_z|^{i,j}\Delta t}{\mu|^{i,j}\varepsilon|^{i,j}}}{\frac{1}{\Delta t} + \frac{\sigma_\rho\big|^{i,j} + \sigma_\varphi\big|^{i,j}}{2\varepsilon|^{i,j}} + \frac{\sigma_\rho\big|^{i,j}\sigma_\varphi\big|^{i,j}\Delta t}{4(\varepsilon|^{i,j})^2}} \tag{3.116}$$

$$H' = \frac{\frac{\sigma_\rho\big|^{i,j}\sigma_\varphi\big|^{i,j}\Delta t}{(\varepsilon|^{i,j})^2}}{\frac{1}{\Delta t} + \frac{\sigma_\rho\big|^{i,j} + \sigma_\varphi\big|^{i,j}}{2\varepsilon|^{i,j}} + \frac{\sigma_\rho\big|^{i,j}\sigma_\varphi\big|^{i,j}\Delta t}{4(\varepsilon|^{i,j})^2}} \tag{3.117}$$

and the curl term is now represented as shown in Equation 3.118. This is the main difference between the cylindrical and Cartesian formulations in terms of the effects on the update equations.

$$C_z^E|_t^{i,j} = \frac{1}{i\Delta\rho} E_\varphi\big|_n^{i,j} + \frac{E_\varphi\big|_t^{i+1,j} - E_\varphi\big|_t^{i,j}}{\Delta\rho} \tag{3.118}$$

Finally, the update equation for E_φ is shown in Equation 3.119. This represents Equation 3.106.

$$E_\varphi\big|_{t+\Delta t}^{i,j} = (I')E_\varphi\big|_t^{i,j} + (J')C_\varphi^H\big|_t^{i,j} + (K')\sum_{n=\frac{\Delta t}{2}}^{t} C_\varphi^H\big|_n^{i,j} + (L')\sum_{n=\frac{\Delta t}{2}}^{t} E_\varphi\big|_n^{i,j} \tag{3.119}$$

where the constant terms I', J', K' and L' are defined as

$$I' = \frac{\frac{1}{\Delta t} - \frac{\sigma_\rho\big|^{i,j} + \sigma_z|^{i,j} + \sigma|^{i,j}}{2\varepsilon|^{i,j}} - \frac{\sigma_\rho\big|^{i,j}\sigma_z|^{i,j}\Delta t}{4(\varepsilon|^{i,j})^2}}{\frac{1}{\Delta t} + \frac{\sigma_\rho\big|^{i,j} + \sigma_z|^{i,j} + \sigma|^{i,j}}{2\varepsilon|^{i,j}} + \frac{\sigma_\rho\big|^{i,j}\sigma_z|^{i,j}\Delta t}{4(\varepsilon|^{i,j})^2}} \tag{3.120}$$

$$J' = \frac{1}{\frac{1}{\Delta t} + \frac{\sigma_\rho\big|^{i,j} + \sigma_z|^{i,j} + \sigma|^{i,j}}{2\varepsilon|^{i,j}} + \frac{\sigma_\rho\big|^{i,j}\sigma_z|^{i,j}\Delta t}{4(\varepsilon|^{i,j})^2}} \tag{3.121}$$

$$K' = \frac{-\frac{\sigma_\varphi\big|^{i,j}\Delta t}{\varepsilon|^{i,j}}}{\frac{1}{\Delta t} + \frac{\sigma_\rho\big|^{i,j} + \sigma_z|^{i,j} + \sigma|^{i,j}}{2\varepsilon|^{i,j}} + \frac{\sigma_\rho\big|^{i,j}\sigma_z|^{i,j}\Delta t}{4(\varepsilon|^{i,j})^2}} \tag{3.122}$$

$$L' = \frac{-\frac{\sigma_\rho\big|^{i,j}\sigma_z|^{i,j}\Delta t}{(\varepsilon|^{i,j})^2}}{\frac{1}{\Delta t} + \frac{\sigma_\rho\big|^{i,j} + \sigma_z|^{i,j} + \sigma|^{i,j}}{2\varepsilon|^{i,j}} + \frac{\sigma_\rho\big|^{i,j}\sigma_z|^{i,j}\Delta t}{4(\varepsilon|^{i,j})^2}} \tag{3.123}$$

3.8 Increasing the Speed of Simulation

FDTD based simulations are notorious for their long runtimes. Since the time step, Δt, is chosen based on the Courant stability criterion, with a fixed grid resolution, the time step is on the order of nano to pico-seconds. Further, for continuous tone signals, given the phase delay between the transmitter and receiver due to the propagation of the electromagnetic fields, it is desirable to allow several periods of the input signal to be injected into the computational space. For low frequency signals, this results in a total number of time steps in the thousands and even millions.

In an effort to decrease the runtime of the FDTD simulations, two different approaches were taken in terms of the FDTD algorithm and each approach was benchmarked in terms of the total runtime (which includes other aspects of the simulation, not just the FDTD channel model), the time per time step, and the total FDTD algorithm time over all the time steps. The times measured using the two approaches are shown in Table 1.

Table 1: Data obtained using different FDTD algorithms

Vectorized MATLAB			**For-Loops**		
Tot [s]	**Per Step [ms]**	**Full [s]**	**Tot [s]**	**Per Step [ms]**	**Full [s]**
22.4	0.71	14.7	16.7	0.37	9.4
20.0	0.67	13.8	17.6	0.38	10.0
22.1	0.77	14.7	17.1	0.36	9.8
21.9	0.69	14.2	17.4	0.40	9.9
21.8	0.69	14.3	17.1	0.36	9.9

The FDTD algorithm was implemented two different ways. The first method was by utilizing the matrix nature of data in MATLAB by using vectorized MATLAB since MATLAB is optimized for operations involving matrices and vectors. The second approach was by using nested for-loops to evaluate the fields at each point in the domain. The vectorized MATLAB approach was assumed to be the faster approach, but surprisingly, this was not the case. It is believed that in this application, the vectorized implementation requires significant memory which is not required in the alternative approach.

One simulation configuration was implemented and ran five times each using both FDTD algorithm methods. The average total runtimes were 21.6 and 17.8 seconds for the vectorized and for-loop approaches, respectively. The average times required to run through the 80 x 80 grid was 0.71 and 0.37 milliseconds with the nested for-loop method nearly twice as fast. Finally, the full FDTD component of the simulation, consisting of 14133 time steps, took an average time of 14.3 and 9.8 seconds, with the nested for-loop approach being nearly 31 % faster than the vectorized method.

4 Validating the Simulation Tool

This section provides methods used to validate the results of the simulation tool. First, comparisons of simulation results with several analytical models will be discussed. Next, COMSOL Multiphysics simulation results are presented and compared with the custom FDTD simulation tool. Finally, experimental results will be provided.

4.1 Analytical Models

This section will present three analytical models used to validate the FDTD-based simulation tool developed in this thesis. All three models consider the effects of the water's conductivity on the electromagnetic fields and the presence of the air-water interface. First, the simplest model described by Butler will be introduced. Butler's model provides an estimate of the signal attenuation due to two effects: the first being the propagation of the fields in a conductive medium and the second being attenuation due to reflection at the air-water interface. The second analytical model used here is based on the work of Wait but was implemented based on the work of Gibson. Gibson presents a model of a magnetic dipole submerged in a good conductor with a receiver position located above the interface in a semi-infinite medium. Finally, the third model is the result of the work of my colleague Adam Forget, MSc. Forget has developed an integral equation similar to that of Gibson, with a lot of the same numerical challenges; however, Forget's model also includes the effects of the hardware of the transmitting and receiving coils, so it can potentially be of very practical use.

4.1.1 Frequency Modes in Cavity

As an early means of evaluating the FDTD algorithm, the analytical expressions for the frequency modes inside a cavity (discussed in Chapter 2) were used together with the FDTD simulation results. A cavity surrounded by a perfect electric conductor was constructed and a Gaussian pulse injected into the domain. The z-component of the electric field, E_z, was sampled at the center of the cavity and a Discrete Fourier transform performed, as shown in Equation 4.1.

$$\mathcal{F}\{E_z\} = \sum_{n=0}^{N-1} E_z[n] e^{-j2\pi f k \frac{n}{N}} \qquad 4.1$$

Figure 24 shows E_z as it propagates through the cavity. The cavity dimensions used here are 30 mm wide by 20 mm tall. The perfect electrically conducting walls were achieved using Dirichlet boundary conditions.

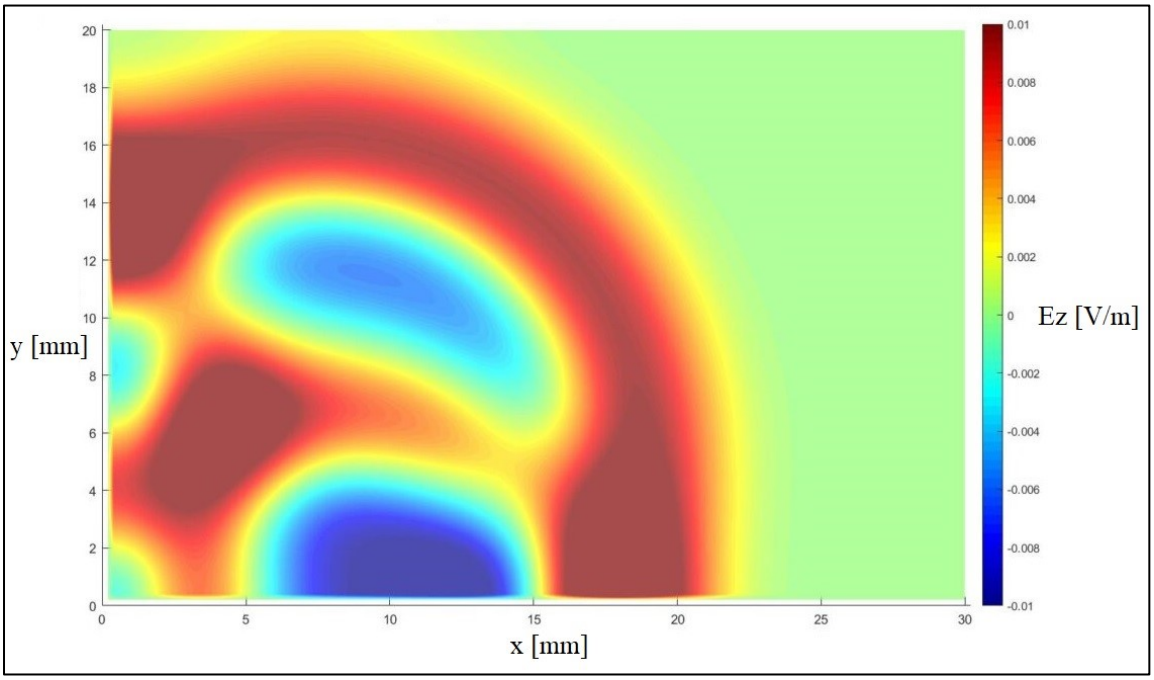

Figure 24: Testing the FDTD algorithm by measuring frequency content in cavity

$\mathcal{F}\{E_z\}$ was then plotted against f_{mn} and the result is shown in Figure 25. The frequency components of E_z perfectly match those predicted by f_{mn}. Since the theoretical frequency modes have been confirmed, the basic FDTD algorithm used here appears valid.

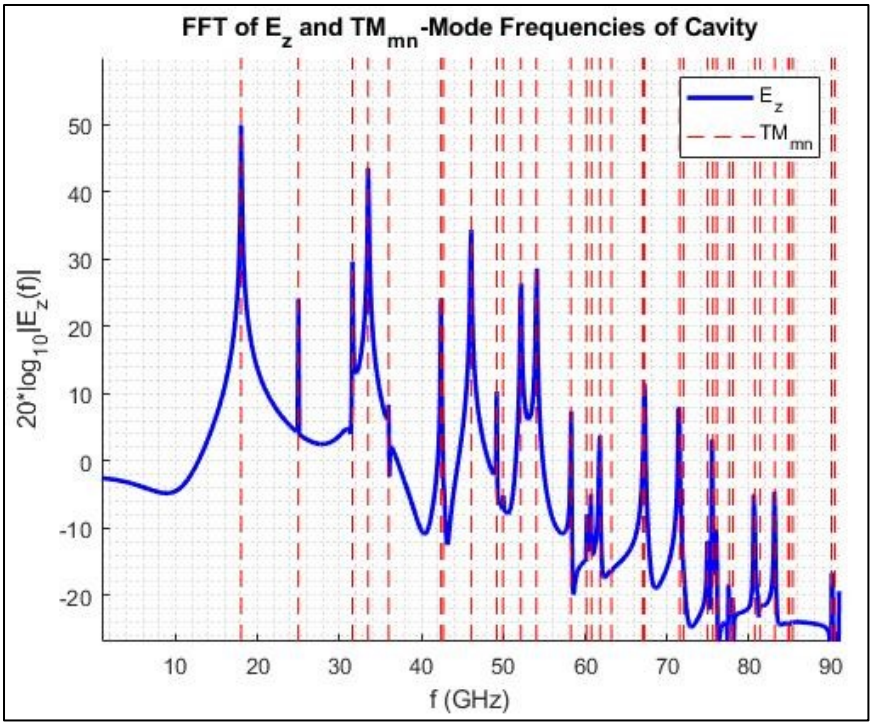

Figure 25: FFT of E_z (blue) and theoretical frequency modes (red)

4.1.2 Field Expressions for Circular Loop

The next method used to validate the FDTD tool was to simulate the magnetic field strength generated by a single turn circular loop of wire, in the absence of water, at varying distances from 40 cm to 3 m. The analytical equations for the radiated fields from a circular loop were discussed in Chapter 2. Since the magnetic field was sampled coaxially, the relevant equation is repeated here for convenience except that it has been converted to cylindrical coordinates using the transformations $\rho = r\sin\theta$, $\phi = \phi$, and $z = r\cos\theta$ where $\theta = 0°$ thus $z = r$.

$$H_z = j\frac{\omega^2\mu\varepsilon a^2 I}{2z^2}\left[1 + \frac{1}{j\omega^2\mu\varepsilon z}\right]e^{-j\omega^2\mu\varepsilon z} \qquad 4.2$$

The test was performed at f = 100 MHz with a grid size of 10/3 cm (N_{dim} = 3). The PML was set to more than one wavelength away. The result is shown in Figure 26.

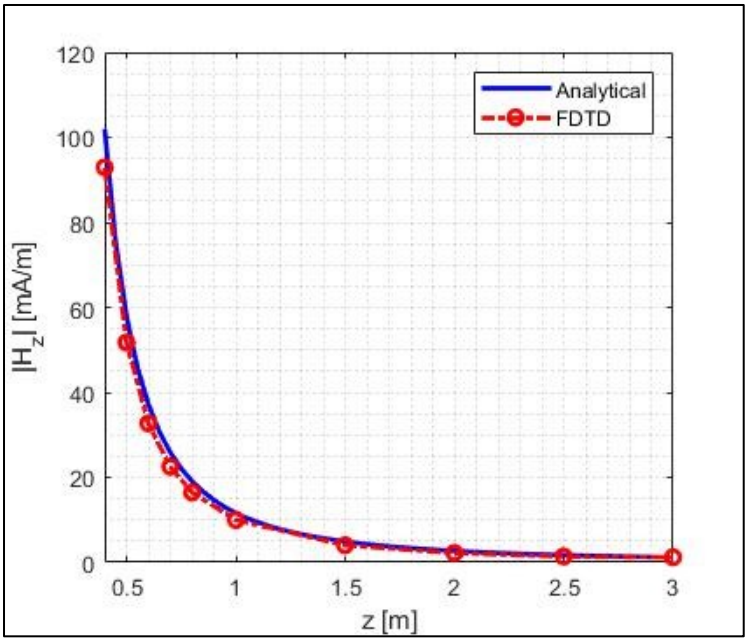

Figure 26: Comparing FDTD results with H-field expressions

As shown in the figure above, the results of this test were very promising thus increasing my confidence further that the FDTD simulator is able to generate accurate results.

4.1.3 Wait's Sommerfeld Integral

Based on the 1969-1971 work of Wait, Gibson presents an alternative form for a transmitting coil submerged in a good conductor and a receiver located above the interface in a semi-infinite medium. The magnetic field at the receiver is expressed as

$$\vec{H} = \frac{m_d}{2\pi h^3}[P\hat{\rho} + Q\hat{z}] \tag{4.3}$$

where P and Q are based on Wait's Sommerfeld integral involving the Bessel functions, J_1 and J_0, and expressed as

$$(P, Q) = \int_0^\infty \frac{x^3 e^{-xZ}}{x + U} e^{-U}\big(J_1(xD), J_o(xD)\big)\, dx \tag{4.4}$$

Where the parameters $U^2 = x^2 + j2\left(\frac{h}{\delta}\right)^2$, $D = \frac{\rho}{h}$, $Z = \frac{z}{h}$, $\delta = \sqrt{\frac{1}{\pi f \sigma}}$, and $m_d = NI\pi r^2$ are used to simplify the integral expression.

Gibson provides details on how to numerically evaluate the Sommerfeld integral; doing so, the magnitude of the magnetic field component H_z can be evaluated at the receiver for different transmitter depths. Figure 27 shows the magnitude of H_z at a few depths.

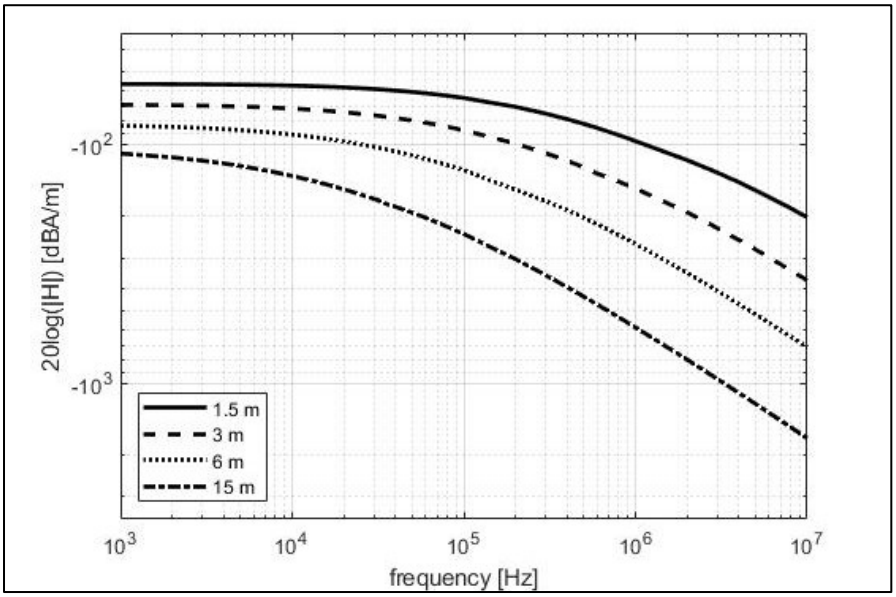

Figure 27: Magnetic field strength using Wait's Sommerfeld integral

Further, from the results shown above, additional information can be extracted and then used for validation of the FDFD simulation. From the definition of Faraday's law, $V_{emf} = \mu \frac{d}{dt} \iint_S \vec{H} \cdot d\vec{S}$, if we assume $\vec{H}$ is nearly constant across the plane of the receiving antenna (with respect to the space variables), then $V_{emf} \approx \mu \frac{d}{dt} \vec{H} \iint_S d\vec{S}$. Since $\iint_S d\vec{S}$ is just the surface area of the receiving antenna, $r^2\pi$, where r is the radius of the receiving coil, then $V_{emf} \approx \mu\pi r^2 \frac{d}{dt} \vec{H}$. Taking the Fourier transform of this expression results in $V_{emf}(f) \approx j2f\mu\pi^2 r^2 \vec{H}(f)$, where finally we have Equation 4.5.

$$|V_{emf}(f)| \approx 2f\mu N\pi^2 r^2 |\vec{H}(f)| \qquad 4.5$$

Using the values for $|\vec{H}(f)|$ obtained from evaluating the Sommerfeld integral and shown in Figure 27, a plot can be produced for $|V_{emf}(f)|$ which shows a decrease in the induced voltage at low frequencies which agrees with Faraday's law. Figure 28 shows the Sommerfeld integral evaluated at various transmitter depths from 1.5 to 15 meters with a receiving coil 1 meter above the water's surface. The expected bandpass effects of the channel are visible in Figure 28 and a suitable channel bandwidth can be approximated.

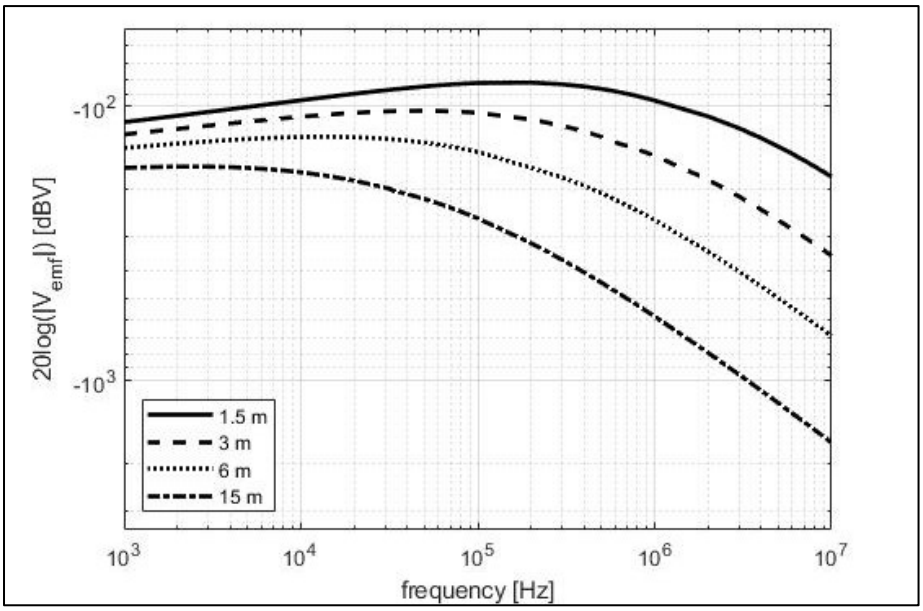

Figure 28: Calculating the induced voltage from |H|

The FDTD simulations were run with the receiver coil fixed horizontally at heights of 0.5 and 1 meter above the water's surface, the transmitter aligned horizontally and coaxial with the receiver, and at transmitter depths of 0.5, 1, 2, and 3 meters. Wait's Sommerfeld integral was evaluated numerically using MATLAB's built-in *quad1()* function which uses adaptive Gauss/Lobatto quadrature. A comparison of the results of these two models is shown in Figure 29. The coils are assumed to have a 10 cm radius, the transmitting coil having 5 turns, the receiving coil having 5 turns, and the driving current having a maximum amplitude of 1 A.

Figure 29 shows a good match between the FDTD simulation results and Wait's analytical expression in terms of cut-off frequencies, but the solutions diverge at the lower frequencies in terms of the magnitude of the induced voltage. If we define a limit for the magnitude of the induced voltage, based on the sensitivity of the measurement equipment, of around -120 dBV ($\sim$1 μV), then for a depth of 2 m, both models predict a center frequency of around 100 kHz. Both models show an induced voltage magnitude of around -100 to -80 dBV (10 to 100 μV) at 100 kHz.

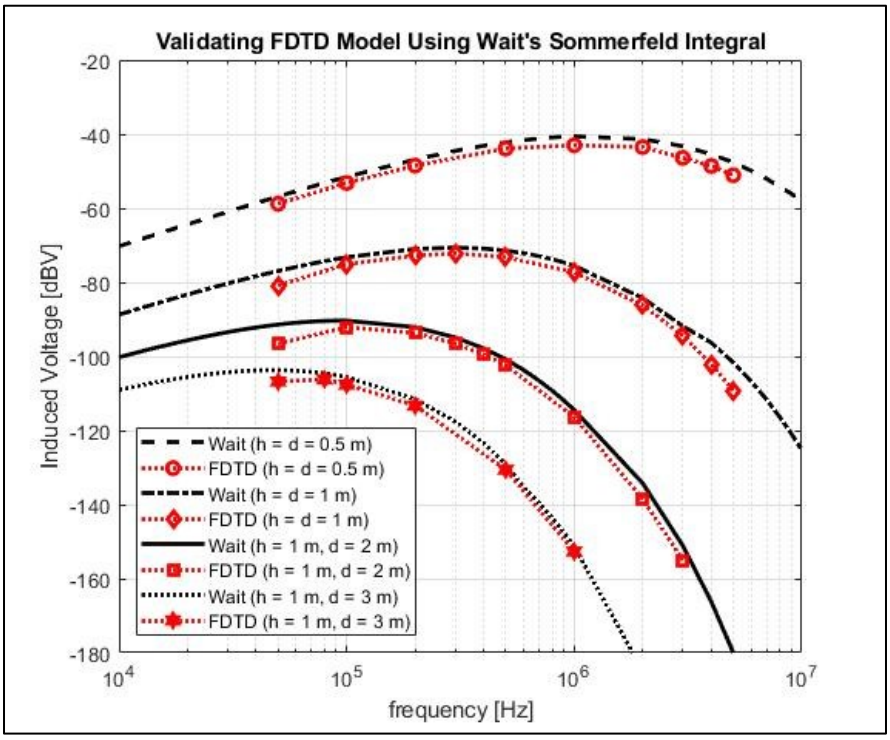

Figure 29: Validating the FDTD simulations using Wait's Sommerfeld integral

4.1.4 Forget's Analytical Model

An analytical model was developed by a colleague, Adam Forget, as part of his M.A.Sc. thesis in Electrical Engineering. Forget was part of the team studying the use of magnetic induction to cross the air-water interface with a focus on the development of an analytical model. Forget's analytical model was used as part of the validation process.

The geometry used by Forget is shown in Figure 30. Forget's approach consists of two key steps: 1) solving for the magnetic field produced by the transmitting coil for the case

of infinitely deep water, and 2) applying the appropriate boundary conditions at the air-water interface. Where Wait's approach using the Sommerfeld integral focus on the magnetic dipole moment of the transmitting coil, Forget's model is based on the mutual inductance between the transmitting and receiving coils.

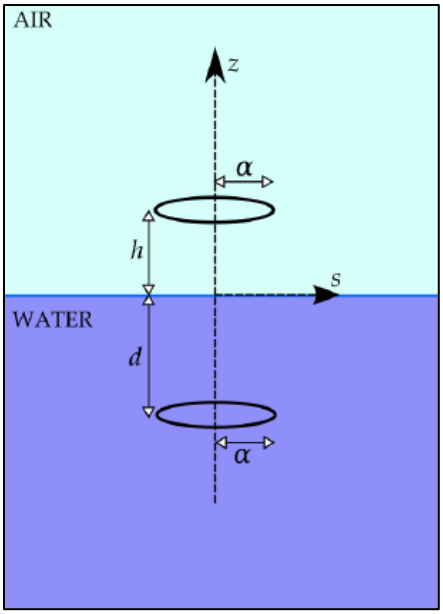

Figure 30: Forget's geometry setup (source: Forget)

Forget's analytical model is in the frequency domain, with the transmitting coil current modelled as an impulse allowing the frequency response of the system to be determined. Forget uses the definition of the magnetic vector potential, $\vec{H} = \frac{1}{\mu}\nabla \times \vec{A}$, and solves the wave equation in terms of $\vec{A}$

$$\nabla^2 \vec{A} + k^2 \vec{A} = -\mu \vec{J} \tag{4.6}$$

which, in cylindrical coordinates, takes the form

$$\frac{\partial^2 A}{\partial s^2} + \frac{1}{s}\frac{\partial A}{\partial s} - \frac{1}{s^2}A + \frac{\partial^2 A}{\partial z^2} + k^2 A = -\mu_0 NI\delta(s-\alpha)\delta(z+d) \tag{4.7}$$

Forget uses a Fourier transform in the spatial variable z followed by a first-order Hankel transform in s to solve Equation 4.7 for A. Boundary condition for the electric and magnetic fields are then applied to the air-water interface resulting in the an expression for $\vec{H}$ as shown in Equation 4.8.

$$\vec{H} = NI\alpha \int_0^\infty \frac{k}{K_w + K_0} J_1(k\alpha) e^{jK_w d} \left[K_0 J_1(ks) e^{jK_o z} \hat{s} + jk J_0(ks) e^{jK_o z} \hat{z} \right] dk \qquad 4.8$$

where $K_w = \sqrt{(2\pi f)^2 \varepsilon_w \mu_0 - k^2}$ and $K_0 = \sqrt{(2\pi f)^2 \varepsilon_0 \mu_0 - k^2}$ are the wave numbers under water and in air, respectively. The induced voltage in the receiving coil is found using Faraday's law resulting in Equation 4.9.

$$V(f) = V_0 \Omega \int_0^\infty \frac{x J_1^2(x) e^{j\left(\frac{h}{\alpha}\sqrt{\Omega^2 - x^2} + \frac{d}{\alpha}\sqrt{\varepsilon_{r,w}\Omega^2 + j\Sigma\Omega - x^2}\right)}}{\sqrt{\Omega^2 - x^2} + \sqrt{\varepsilon_{r,w}\Omega^2 + j\Sigma\Omega - x^2}} dx \qquad 4.9$$

where $x = k\alpha$ is a dimensionless variable of integration, $\varepsilon_{r,w} = \frac{\mathcal{R}e\{\varepsilon_w\}}{\varepsilon_0}$ is the dielectric constant of water, $\Omega = \frac{2\pi\alpha f}{c}$ is a dimensionless frequency parameter, $\Sigma = \mu_0 c \alpha \sigma$ is a dimensionless conductivity parameter, and $V_0 = 2\pi\mu_0 N^2 Ic$ is a voltage parameter in volts.

The FDTD simulator was run with the transmitting coil located at depths 1, 2, and 3 meters, with the receiving coil located at 1 m above the water's surface. The results were plotted with that of Forget and are shown in Figure 31. The results show a good match in terms of the general trend of the frequency response.

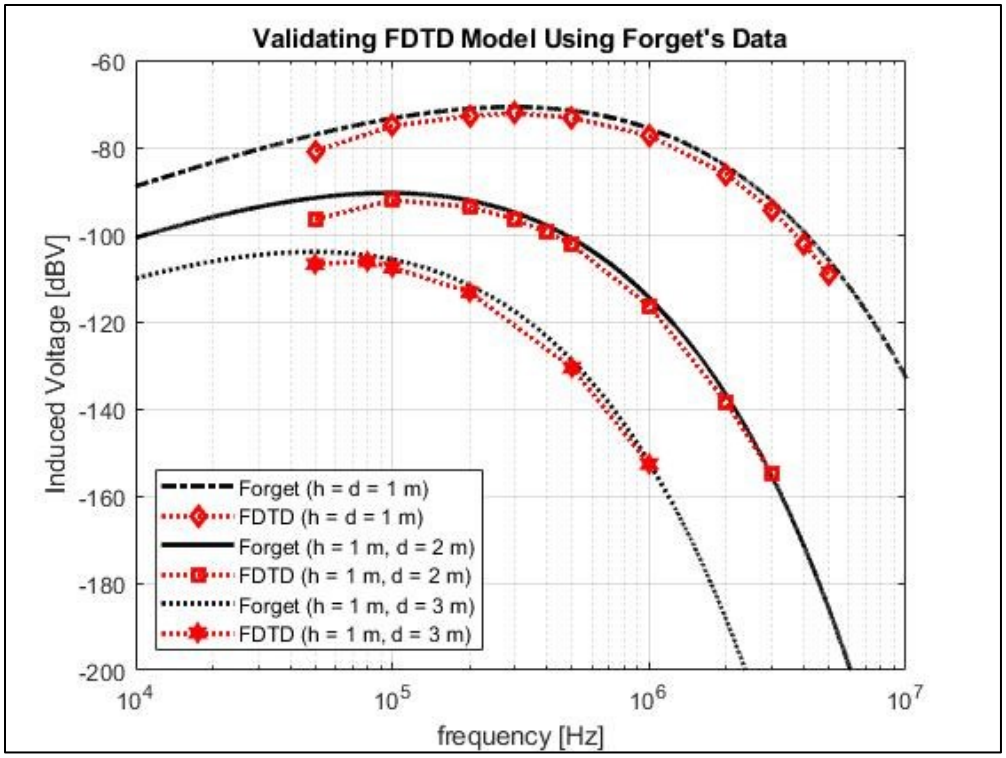

Figure 31: Validating the FDTD tool using Forget

4.2 Test Apparatus for Experiments

The original plan was to design and build an underwater test apparatus intended to test and validate the results of the analytical and FDTD models discussed above early in the Summer of 2020; however, due to the recent social and political ramifications of the COVID-19 virus, the scheduling for these activities have been delayed. At the time of this writing, we expect to be able to test the magnetic induction link some time in late Summer or Fall, 2020. Unfortunately, this timeframe is just outside that of this thesis, so the results of those tests will not be included here. The results of those field experiments will be included in future work. This section will describe the development of the test platform to date and describe, potentially, how the tests will be conducted later this year.

4.2.1 Transmitter Design

The transmitter was designed and is being built by my colleagues Cole Ferguson and Adam Forget. A block diagram of the main system components is shown in Figure 32.

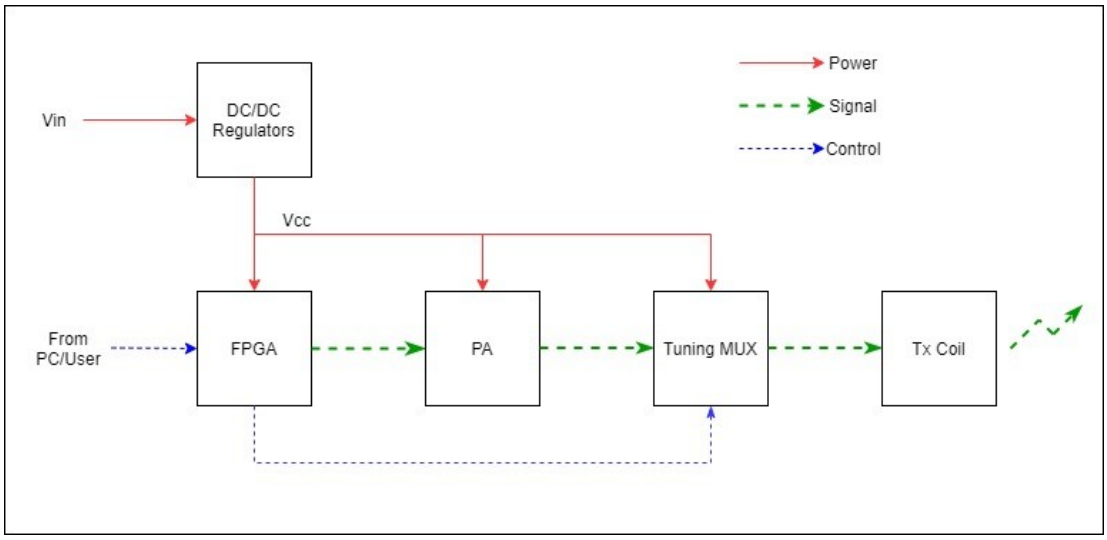

Figure 32: Block diagram of transmitter

The input voltage will be supplied by a 24 V battery pack. Two DC/DC voltage regulators will be used to supply the positive and negative voltage rails for system power. The positive voltage rail will be supplied by the R-735.5P and the negative rail by the PTN78020A. The transmit signals are generated using a Zybo z7-20 development board which includes a 667 MHz dual-core ARM Cortex-A9 processor and a Xilinx 7-series FPGA. The power amplifier is the PA162u capable of 1.5 A output current and a bandwidth above 1 MHz. The tuning multiplexer block (Tuning MUX) consists of a capacitor bank and Single-Pole Double-Throw (SPDT) relays capable of withstanding the expected operating conditions and are intended to tune the transmitting coil to each of the frequencies of interest. The coil itself consists of three perpendicular coils intended to eliminate the dependence on the transmitter coil's orientation. This is a common approach in the literature.

4.2.2 Receiver Design

The author was responsible for the development of the receiver platform. A block diagram of the main system components is shown in Figure 33. The receiving coil and tuning circuits are identical to that of the transmitter. The Low Noise Amplifier (LNA) is the LT1167 which has an easily adjustable gain, G, determined by the resistor between the two R_g pins and is given by $G \approx 1 + 49.4k\Omega/R_g$. The Data Acquisition System

(DAQ) is the NI-PCIe-6321 by National Instruments, which can sample at near 250 kHz which means our frequency of operation is limited by the Nyquist sampling criterion to around 125 kHz.

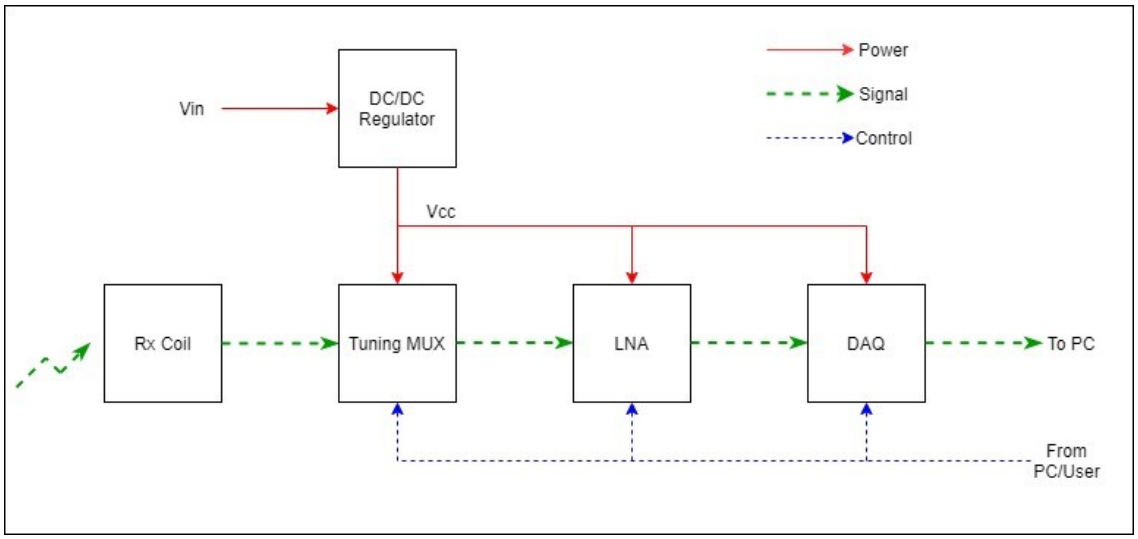

Figure 33: Block diagram of receiver

It was decided that a resonating tank circuit would be used to tune the receiving network, and LTspice simulations verify the need for this tuning. Figure 34 and Figure 35 show the setup in LTspice and the simulation results, respectively. The transmitting circuit (consisting of V1, R1, C1, and L1) is tuned for near 25 kHz. The resonating tank circuit consists of L2 and C2 in the figure below. The value of C2 takes on values above, below, and at the capacitance value necessary for tuning the receiving coil for 25 kHz, which in this case is 270 nF for a 150 μH coil.

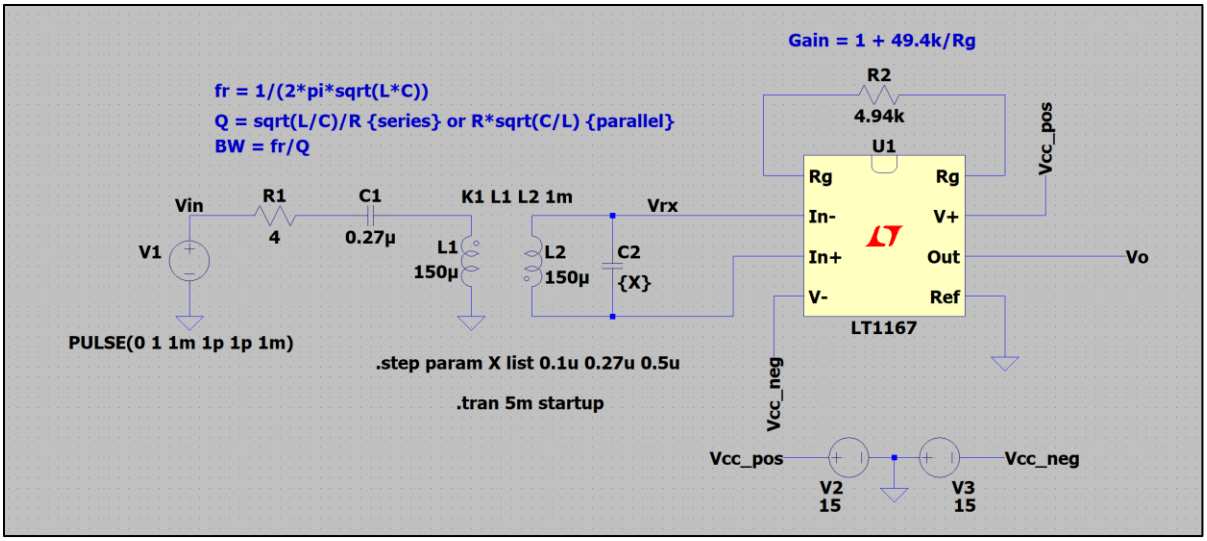

Figure 34: LTspice simulation of resonating tank circuit in receiver

In Figure 35, the Fourier transforms of the signals induced in the receiving coil for each value of C2 is presented when a wideband pulse is injected into the transmitting circuit. It is clear the largest induced voltage occurs when the value for C2 equals 270 nF (the blue curve, run 2/3). The difference is as much as 15 dB, which translates to an increase in the size of the induced voltage on the order of 2^5 for these particular capacitor values. We want to ensure the received signal level is well above the noise floor, so having the ability to tune the receiving circuit for our frequency of operation is paramount.

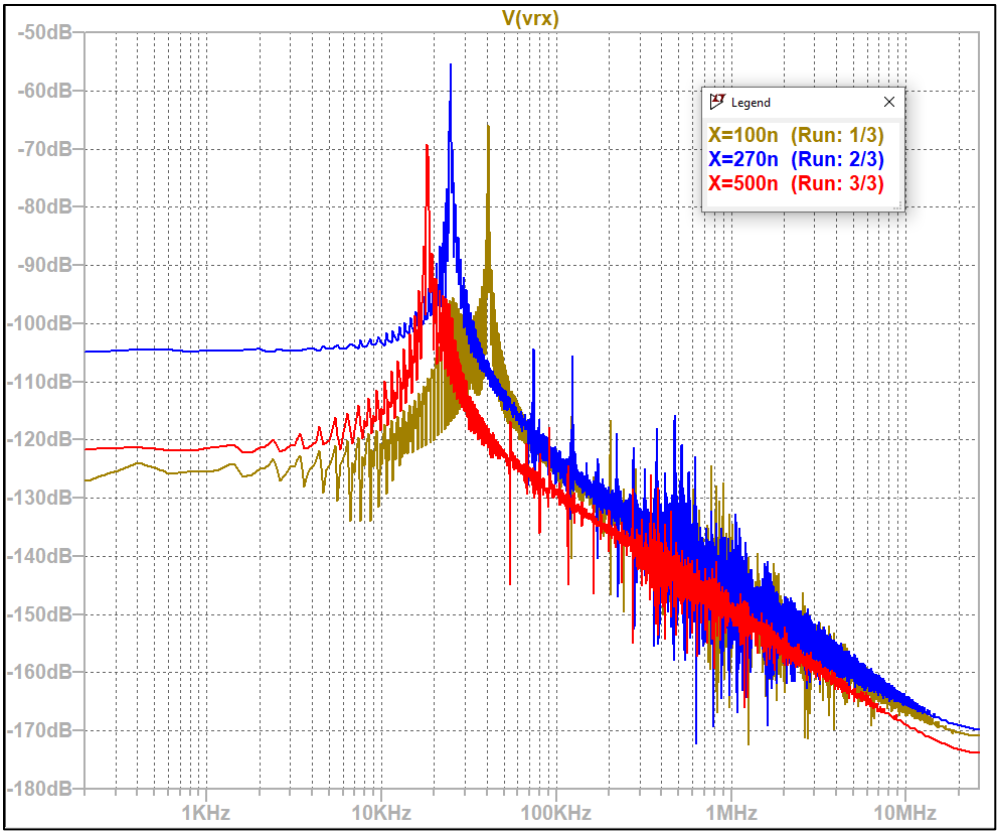

Figure 35: FFT of induced voltage in receiving coil

4.2.3 Preliminary Test Plan

The test will begin by lowering the transmitting coil, in its corresponding pressure case and attached to a vertical member, into the water to a depth of 3 meters. The receiving coil will be fixed at the top the vertical member at a height of 1 meter above the water with the coil plane parallel to the water's surface. The control boxes for both the transmitting and receiving coils will be located outside of the water on a floating platform. The vertical member will be fixed to the floating platform such that it remains vertical and the two coils are coaxially oriented. The transmitting coil will be set to transmit a continuous wave signal adjustable from 10 to about 150 kHz. The receiving coil will measure and record the resulting induced voltage for comparison with the analytical and FDTD models.

Next, the transmitting coil will be lowered to depths of 4, 5, 6, 7, 8, 8, and 10 meters and the frequency of the transmitted signal at each depth will be adjusted such that the

maximum induced voltage in the receiving coil is obtained. This data will be used in additional models and simulations for comparison. Finally, the transmitting coil will be lowered deeper until the Signal-to-Noise (SNR) ratio reaches the level of 10 dB which is a typical SNR used to define the limits of barely intelligible speech (Blake, 2002). The associated depth will be assumed to be the maximum practical depth.

5 Discussion of Results and Conclusion

This chapter will provide a discussion of the simulation results followed by the final closing remarks.

5.1 Simulation Results

Before the simulation results are presented, a description of the FDTD simulation setup will be discussed. The FDTD simulation setup is very sensitive to the parameters mentioned here, so these important details will be provided first. The FDTD simulation results will be presented and compared with the results of numerically integrating Wait's Sommerfeld, according to the work of Gibson, as was discussed in the preceding chapter. The FDFD results will then be used to evaluate the communication system, as was discussed in Chapter 2. Finally, issues with the FDTD simulator (for example: long runtime, sufficient computational domain size, etc.) will be discussed.

5.1.1 Setup of the FDTD Simulations

The simulations performed during this analysis were configured according to the parameters listed in Table 2. These parameters are important in terms of repeatability, as the FDTD simulations are sensitive to them.

Table 2: FDTD simulation configuration parameters

Parameter	**Value**
Number of Turns (Both Coils)	5.0
Transmit Coil Current	1.0 A
Coil Radius (Both Coils)	10.0 cm
Water Conductivity	4.0 S/m
Water Permittivity	81.0
Air Conductivity	0.0 S/m
Air Permittivity	1.0
FDTD Grid Size	3.333 cm
Receiver Heights	0.5, 1 m
Transmitter Depths	0.5, 1, 2, 3 m
Periods of Input Signal	1.5 to 6.0
Distance from Tx Coil to Domain Edge	$> \lambda_{H_2O}$
Frequency Range	50 to 5000 kHz

5.1.2 Comparing FDTD Results with Wait/Gibson

Wait's Sommerfeld integral was the main tool used to validate the FDTD simulation results. The induced voltage determined by the Sommerfeld integral, as described in the previous chapter, was used to troubleshoot the FDTD simulator throughout the development process. Since the work of Wait and Gibson directly relates to the problem of magnetic fields crossing the interface of air with a conductive medium (not necessarily water), it seems fitting that the FDTD results should be compared directly with that of Wait/Gibson. This comparison is repeated in Figure 36 for convenience.

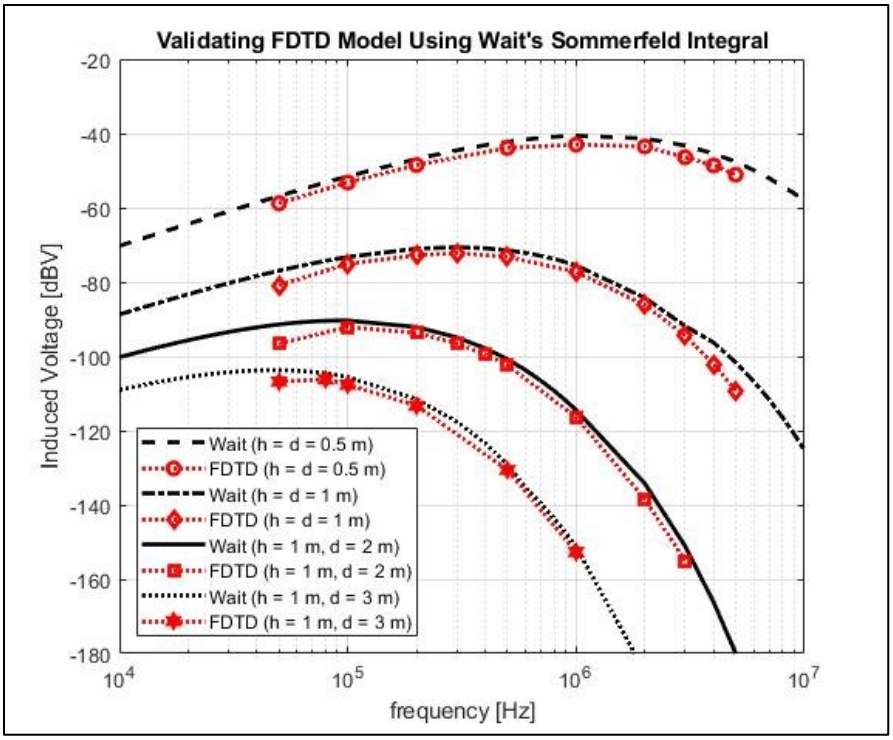

Figure 36: Results using FDFD and Wait's Sommerfeld integral

The first impression one gets by comparing the FDTD results with that of Wait/Gibson in Figure 36 is how closely the red curves match the location and shape of the black curves. One of the main goals of this project was to determine the optimum center frequency at varying transmitter depths. The results show the local maxima for each pair of curves (corresponding to each height/depth configuration) matches well. This iss perceived as a very good indication that the FDTD simulator does a good job at accurately representing the physics of the problem.

Table 3: Comparing key results of FDTD with Wait/Gibson

	Maximum Induced Voltage / Optimal Center Frequency	
Rx Height / Tx Depth	**Wait/Gibson**	**FDTD**
0.5 m / 0.5 m	-40.6 dBV / 1 MHz	-43.0 dBV / 1 MHz
1 m / 1 m	-70.6 dBV / 300 kHz	-72.2 dBV / 300 kHz
1 m / 2 m	-90.4 dBV / 100 kHz	-92.1 dBV / 100 kHz
1 m / 3 m	-103.7 dBV / 50 kHz	-106.2 dBV / 80 kHz

5.1.3 Communication System Evaluation

The results of the FDTD simulations were used to predict the Signal-to-Noise Ratios (SNR) and theoretical channel capacities for three specific coil orientations. The SNR and capacities included here were calculated using the methods described in the section on the communication system evaluation in Chapter 2. The results are shown in Table 4. Note: the final row in Table 4 includes the results of Wait/Gibson because the validity of the datapoint obtained using the FDTD model at 50 kHz is questionable. This is an effect seen at very low frequencies and will be explained in the next section. Unfortunately, simulations involving transmitter depths more than a few meters deep require very low frequencies, so this FDTD tool in its current form is not able to simulate these scenarios.

Table 4: Predictions of SNR and capacity

Rx Height [m]	**Tx Depth [m]**	**Optimal Center Frequency [kHz]**	**Induced Voltage [dBV]**	**SNR [dB]**	**Capacity [kbps]**
0.5	0.5	1000	-43.0	85.6	1421.8
1	1	300	-72.2	61.6	307.1
1	2	100	-92.1	46.5	77.3
1	3	80	-106.2	33.4	44.6
1	3	50 [1]	-103.7	37.9	31.6

Note [1]: This datapoint is from the results of Wait/Gibson

The MI link has been shown to have the potential to have a relatively high throughput when compared to traditional underwater acoustic communication systems which obviously do not have the ability to cross the air-water interface. Even with the transmitter located at a depth of 3 m, with the receiver at a height of 1 m, operating at an optimal center frequency of 80 kHz, a SNR near 33 dB may be possible resulting in a channel capacity near 44 kbps. The TARF system described by researchers at MIT could only support data-rates from 100 to 400 bps with average SNR values from about 10 to 25 dB while transmitting at 75 W at 150 Hz from a depth of 0.9 to 3.6 m using various forms of modulation including BPSK, QPSK, and 16-QAM. Further, the TARF system shows a decrease in SNR with depth from 25 dB at 0.9 m to 14 dB at 3.6 m. The performance of TARF is comparable to traditional underwater acoustic systems (Tonolini and Adib, 2018). The simulation results show MI has great potential as a means for crossing the air-water interface while maintaining relatively high throughput.

5.1.4 Peculiarities of the FDTD Simulator

There are several important phenomena which have the potential to dramatically affect the FDTD simulation results, and these should be noted. First, the test signal must be allowed sufficient time to reach a steady state before the simulation can be determined to be finished and valid. For example, a higher frequency such as 2 MHz may need six periods of oscillation to achieve a steady state whereas a lower frequency of say 200 kHz may only need three. In practice, some of the FDTD simulations used to obtain a single data point had to be run more than once with increasing run-times after the user post-processed the results and made the determination that a steady state was not achieved.

Next, the FDTD results are sensitive to the proximity of the absorbing boundary conditions and this phenomenon was also described by Abrahamsson, in which he states that if air is included in the computational domain, considering the relatively long wavelengths, the air layer must be sufficiently large (Abrahamsson, 2011). The result will show a value for the induced voltage that can be several dBs too high if the domain is too small. Simulation ran at lower frequencies require larger computational domains due to the increased wavelengths.

The FDTD runtime increases as the frequency decreases because the timestep is based on the Courant stability criterion thus is fixed at a very small value on the order of 70 ps. Since the FDTD simulator should be run for two to six periods of oscillation, this results in a very high number of time steps. For the case where the frequency is set to 50 kHz and the number of periods of oscillation are set to 1.5, the number of timesteps is 423,971. Using a computer with an adequately air-cooled AMD Ryzen 7 - 2700X CPU with 8 cores and 16 threads, 32 GB of RAM, a NVIDIA GeForce RTX 2060 graphics card, and a 500 Watt power supply, this simulation takes around four hours.

Probably the most significant bug discovered during the testing of the FDTD simulator, is the behaviour when the number of time steps is very large (over ~425,000). There seems to be an accumulation of energy in the PML which after a sufficient number of iterations begins to seep into the computational domain effecting the simulation results. The fields in the region of interest begin to increase and do not resemble a sinusoidal form. This is why the FDTD simulator was not run at frequencies below 50 kHz. This appears to be the lower limit of usability of the simulator at this time (V10.0.1). It is not obvious if this result is due to fields accumulating in the PML or a numerical artifact of the FDTD scheme used to model damped waves as discussed next. It is thought that this result does not accurately represent the physics of the problem as low frequency signals have been shown to be effective forms of MI communication across the air-water interface (for example, in 2018, Chai et al demonstrated error-free communication over 35 m in the frequency range of tens of Hz).

Possibly related to the previous point, this thesis would not be complete without at least mentioning the concept of *diffusion* when discussing low-frequency electromagnetic fields in conductive media. The simulations indicate that this phenomenon does occur. This topic is interesting and deserves discussion. As discussed in the separate works of Moore and Blair (1961), Tyler et al (1998), Gibson (2003), and Loseth et al (2006) the equations describing electromagnetic waves in conductive media appear non-wavelike

and exhibit a diffusive behaviour. Mathematically, this can be seen by considering the damped wave equation:

$$\nabla^2\vec{\psi} = \mu\sigma\frac{\partial\vec{\psi}}{\partial t} + \mu\varepsilon\frac{\partial^2\vec{\psi}}{\partial t^2} \quad 5.1$$

When the medium has no conductivity then $\sigma = 0$ S/m and the damped wave equation becomes the familiar undamped wave equation $\nabla^2\vec{\psi} = \mu\varepsilon\frac{\partial^2\vec{\psi}}{\partial t^2}$. However, if the conditions are such that the first term on the right-hand side dominates the second, we have the well known homogeneous diffusion equation $\nabla^2\vec{\psi} = \mu\sigma\frac{\partial\vec{\psi}}{\partial t}$. This becomes apparent for low-frequency signals in conductive materials (Loseth et al, 2006). The stability of the FDTD algorithm, which depends on the choice of the timestep Δt and is related to the grid discretization, is known for EM fields which obey Maxwell's equations, but perhaps this stability criteria differs when the governing equations become more diffusion-like. Walter A. Strauss discusses numerical evaluation of the diffusion equation (Strauss, 2008). Strauss speaks on the accumulation of error due to the incorrect mesh resolution in time and space; although, the stability criterion he presents appears to be satisfied using Courant. This effect of the FDTD results at low frequencies needs to be addressed before the FDTD simulator can be used reliably to study the MI-link at greater depths which require lower and lower frequencies.

5.2 Closing Remarks

In this work, the accuracy of a custom FDTD simulator was demonstrated, and the feasibility of using MI to cross the air-water boundary was confirmed. The FDTD simulations presented here indicate magnetic induction has great potential in applications involving the transmission of data across an air-water interface. The simulations indicate a MI-based communication system has the potential to provide a relatively high data-rate for near-surface communication across the air-water interface: over 30 kbps for a MI transmitter located up to 3 meters deep, and for the case where the transmitter and receiver are close to the air-water boundary, a throughput over 1 Mbps may be possible.

With a driving current of only 1 A, radiuses of just 10 cm, and only 5 turns, both the transmitting and receiving coils are low power and compact, especially compared with traditional RF-based systems which are known to require high power and large antenna geometries. The transmission range may be extended by use of larger coil geometries, higher power, or with an underwater MI waveguide consisting of a series of relay coils (Akyildiz, et al, 2015). This is an active area of research by our research team at UW-Stream Lab.

Bibliography

Abrahamsson, L. *Modelling of Air-seawater Interaction in Marine Electromagnetics*. Swedish Research Agency: Division of Defence and Security, Systems, and Technology. Stockholm. (2011).

Akyildiz, I. Wang, P. Sun, Z. *Realizing Underwater Communication through Magnetic Induction*. Underwater Wireless Communications and Networks: Theory and Application. IEEE Communications Magazine. (November 2015).

Balanis, C. A. *Antenna Theory: Analysis and Design*. (2016). Fourth Edition. Wiley. Hoboken, New Jersey.

Blake, R. *Electronic Communication Systems*. (2002). Second Edition. Delmar Cengage Learning. Clifton Park, New York.

Butler, L. *Underwater Radio Communication*. Amateur Radio. (April 1987).

Chai, B. Wang, J. Zhang, X. *A Test of Magnetic Induction from Air to Sea*. 2018 OCEANS - MTS/IEEE Kobe Techno-Oceans. (May 2018).

Chew, W. C. *Waves and Fields in Inhomogeneous Media*. (1995). IEEE Press. New York, New York.

Domingo, M. C. *Magnetic Induction for Underwater Wireless Communication Networks*. IEEE Transactions on Antennas and Propagation. Vol 60. No 6. (June 2012).

Gibson, D. *Channel Characterization and System Design for Sub-Surface Communication*. (2003). Published by David Gibson in Lulu Enterprises Inc.. Leeds, Great Britain.

Grainger, J. J. Stevenson Jr, W. D. *Power System Analysis*. (1998). McGraw-Hill Electrical and Computer Engineering Series. McGraw-Hill Inc.. USA.

Gulbahar, B. Akan, O. *A Communication Theoretical Modeling and Analysis of Underwater Magneto-Inductive Wireless Channels*. IEEE Transactions on Wireless Communications. Vol 11. No 9. (September 2012).

Guo, H. Sun, Z. *Channel Modeling of MI Underwater Communication using Tri-directional Coil Antenna*. 2015 IEEE Global Communications Conference. (December 1015).

Inan, U. S. Inan, A. S. *Electromagnetic Waves*. (2000). Prentice Hall. Upper Saddle River, New Jersey.

Loseth, L. Pedersen, H. Ursin, B. Amundsen, L. Ellingsrud, S. *Low-frequency Electromagnetic Fields in Applied Geophysics: Waves or Diffusion?* Society of Exploration Geophysicists. Geophysics. Vol 71. No 4. Pages W29 – W40. (July 2006).

Maxwell, J. C. *A Treatise on Electricity and Magnetism*. (1954 reprint from original from 1873). Dover Publications INC. New York, New York.

Rumpf, R. C. Online course called *EE5303 – Electromagnetic Analysis Using Finite-Difference Time-Domain*. University of Texas El Paso. Retrieved in Fall 2019. https://empossible.net/academics/emp5304/.

Sacks, Z. S. Kingsland, D. M. Lee, R. Lee, J. *A Perfectly Matched Anisotropic Absorber for Use as an Absorbing Boundary Condition.* IEEE Transactions on Antennas and Propagation. Vol 43. No 12. (December 1995).

Sadiku, M. N. O. *Elements of Electromagnetics*. (2010). Fifth Edition. Oxford University Press. New York, New York.

Sadiku, M. N. O. *Numerical Techniques in Electromagnetics with MATLAB*. (2015). Third Edition. CRC Press. Boca Raton, Florida.

Strauss, W. *Partial Differential Equations*. (2008). Second Edition. John Wiley & Sons Inc.. Hoboken, New Jersey.

Taflove, A. Hagness, S. *Computational Electrodynamics: The Finite-Difference Time-Domain Method.* (2005). Third Edition. Artech House. Boston, Massachusetts.

Tyler, R. H. Boyer, T. P. Minami, T. Zweng, M. M. Reagan, J. R. *Electrical Conductivity of the Global Ocean*. Earth, Planets, and Space. Springer Open. (2017).

Uribe, C. Grote, W. *Radio Communication Model for Underwater WSN*. 2009 3rd International Conference on New Technologies, Mobility and Security. (December 2009).

Wang, Y. Dobbin, A. Bousquet, J.F. *A Compact Low-power Underwater Magneto-inductive Modem*. WUWNET. (October 2016).

Wang, H. Zheng, K. Yang, K. Ma, Y. *Electromagnetic Field in Air Produced by a Horizontal Magnetic Dipole Immersed in Sea: Theoretical Analysis and Experimental Results.* IEEE Transactions on Antennas and Propagation. Vol 62. No 9. (September 2014).

Yee, K. S. *Numerical Solution of Initial Boundary Value Problems Involving Maxwell's Equations in Isotropic Media*. IEEE Transactions on Antennas and Propagation. Vol 14. Pages 302 to 307. (1966).

Zhang, S. Tu, X. Zheng, K. Yang, M. *Radiation Fields Across Sea-air Interface from Underwater Magnetic Dipole Source*. Electronic Information and Communication Technology 2019 IEEE 2nd International Conference. pages 728-731. (2019).